University of Sfax
Faculty of Sciences of Sfax

University of Sfax
Università degli Studi di Messina

In order to obtain the
Doctorate degree of Research in Physics of Materials & Nanostructures

Presented by

*Khouloud ABID*

Laboratory of Dielectric and Photonic Materials

LabSensor

# Development of Two-dimensional (2D) Sensing Materials

Defended on 19/12/2022 in front of the Jury composed of

| | | |
|---|---|---|
| Prof. Mourad Arous | Professor at FSS | President |
| Prof. Ramzi Maâlej | Professor at FSS | Supervisor |
| Prof. Giovanni Neri | Professor at UNIME | Supervisor |
| Prof. Pietro Gucciardi | Professor at CNR | Co-Supervisor |
| Prof. Mohamed Ellouze | Professor at FSS | Reviewer |
| Prof. Andrea Donato | Professor at UNIRC | Reviewer |
| Prof. G.Guido Condorelli | Professor at UniCt | Examinator |

"A person who never made a mistake never tried anything new " — *Albert Einstein*

---

"Una persona che non ha mai sbagliato non ha mai provato nulla di nuovo " — *Albert Einstein*

# Acknowledgment

*I am taking this opportunity to express my gratitude to everyone who supported me throughout the course of this thesis. In the beginning, I am grateful to God for the good health and well-being that were necessary to complete this thesis.*

*I dedicate the success of these three years to my mother Naima, my father Ahmed, and my lovely sister Cyrine, who have provided me with moral and emotional support.*

*I would like to express my sincere thanks to my supervisor* ***Prof.Ramzi Maâlej****, who allowed me to access his laboratory and to be part of his wonderful team. I am grateful for his aspiring guidance, friendly advice, and in believing in me as well as my skills during this period of work.*

*My sincere appreciation goes to my supervisor* ***Prof.Giovanni Neri*** *in Messina-Italy who gave me the opportunity to be a part of his amazing group. Moreover, I express my warm thanks for believing in me and my skills, for his friendly advice during this period of work, and for giving me the chance to work in such an interesting and new field. My deep thanks to Kaveh for his support, time to teach me, and warm greetings to all group for being such amazing friends and second family; Angelo, Vivi, Simona…*

*I wish to extend my special thanks to* ***Prof. Pietro Gucciardi*** *and* ***Dr.Antonino Fotti*** *for their time, and knowledge, and to all the members of the CNR center for the amazing moments spent with them during this period; Onofrio, Antonella, Maria Grazie, Alessandro, David, Martin, and Silvi.*

*I express my warm thanks to my committee members from Sicilia, Italy:* ***Prof.Andrea Donato*** *and Ms.* ***Prof. Guglielmo Guido Condorelli,*** *and from Sfax-Tunisia;* ***Prof.Mourad Arous and Prof.Mohamed Ellouze*** *for their acceptance to attend my thesis defense.*

*I gratefully recognize the help of* ***Prof.Nour Hamza*** *for her time, knowledge, and support during my master's and thesis work.*

*I am also thankful to my friends (Kawther, Amina, and Rahma) who have supported me along the way.*

*I take this opportunity to express gratitude to all other people. I also place on record, my sense of gratitude to one and all, who directly or indirectly, have lent their hand in this venture.*

---

*Khouloud ABID♥*

# *Abstract*

**I**n recent years, two-dimensional (2D) materials have gained crucial interest in several fields. This interest is noted after the discovery of graphene in 2004 using the scotch tape exfoliation method. Among the synthesized 2D materials, we are interested in transition metal dichalcogenides (TMDCs) thanks to their fascinating features citing the indirect-to-direct bandgap crossover, large surface-to-volume area, high carrier mobility...

**T**he most studied TMDCs material is molybdenum disulphide ($MoS_2$). Actually, researchers are also paying attention to tungsten disulfide ($WS_2$) and molybdenum selenide ($MoSe_2$) illustrating a wide potential of applications, especially as chemical sensors. Indeed, the sensing field become more significant due to its use in daily and practical life.

**I**n this thesis, we are interested in the development of two different types of sensors; electrochemical and plasmonic-based on the 2D-TMDCs nanosheets (NS). Herein, we have exfoliated $MoS_2$, $WS_2$, and $MoSe_2$ NS using the liquid phase exfoliation (LPE) technique. By using these nanosheets, we have created different nanocomposites which were used later as sensing layers for different analytes.

**F**or electrochemical sensors, we have chosen a low-cost, simple-to-use device known as a screen-printed carbon electrode (SPCE) where the working electrode is modified with several modifiers. Two different fields of application were our focus: medicine and agriculture user cases. For the first one, we chose folic acid (FA) and dopamine (DA) as analytes. Regarding FA known also as vitamin B9, its determination was on the AuNPs-$MoS_2$ system showing a new sensing mechanism. Indeed, the FA molecules are strongly adsorbed on the surface leading to the decrease of the anodic current peak instead of its increase when adding FA concentration. This fact was referred to as the reduction of gold nanoparticles (AuNPs) active sites number. Moreover, the determination of DA has occurred by using SPCE modified with nanocomposite based on $MoSe_2$ and green synthesized AuNPs (AuNPs-$MoSe_2$). An outstanding improvement in the DA Faradic current was noted and inferred to the band between DA and AuNPs surface. For the agricultural field user case, we used the modified SPCE with graphene oxide-tungsten disulphide (GO-$WS_2$) for the determination of a fungicide known as Thiram. Herein, we observed a good performance toward this analyte at low concentrations. Thus, we studied the effect of the variation of the GO to $WS_2$ ratio on the electroanalytical behaviour.

**F**or the plasmonic sensors, we have used the exfoliated nanosheets coated with noble metal for the detection of different analytes using enhanced Raman spectroscopies (ERS): surface-enhanced Raman spectroscopy (SERS), and photo-induced enhanced Raman spectroscopy (PIERS). Indeed, the Au-$MoS_2$ sensing layer was used to determine 4-mercaptobenzoic acid (MBA) and FA where we noticed a good performance. Moreover, the MBA molecules were used also to check the efficiency of the Au-$WS_2$ substrate where the PIERS performance of this prior was found to be better than that of SERS. This fact is owing to the charge transfer from $WS_2$ nanosheets and AuNPs owing to the UV-C pre-irradiation step in PIERS. The last substrate used as a plasmonic sensor is made of $MoSe_2$ and gold nanorods (AuNRs) that were used to detect methylene blue (MB) pigment. From this test, the SERS performance was improved and we noted a strong enhancement in the Raman signals while with the PIERS we observed better behaviour with significant improvement.

**A**ll of these investigations are either published or submitted in journals with high impact factors. This work is only the initiative of a deeper work that will be accomplished after the thesis.

# *Sommario*

**N**egli ultimi anni, i materiali bidimensionali (2D) hanno acquisito un interesse cruciale in diversi campi. Questo interesse è stato notato dopo la scoperta del grafene nel 2004 utilizzando il metodo di esfoliazione dello scotch. Tra i materiali 2D sintetizzati, siamo interessati ai dicalcogenuri dei metalli di transizione (TMDC) per le loro affascinanti caratteristiche quali il crossover indiretto-diretto del band-gap, l'ampia area superficiale, l'elevata mobilità dei portatori di carica elettrica ....

**A** materiale dei TMDC più studiato è il disolfuro di molibdeno ($MoS_2$). Recentemente, i ricercatori stanno prestando attenzione anche al disolfuro di tungsteno ($WS_2$) e al seleniuro di molibdeno ($MoSe_2$) presentano un ampio potenziale di applicazioni soprattutto come sensori. In effetti, tali dispositivi risultano estremamente importanti a causa del suo utilizzo nella vita quotidiana e pratica.

**I**n questa tesi ci siamo interessati allo sviluppo di due diverse tipologie di sensori; elettrochimico e plasmonico basati sui nanosheets (NS) 2D-TMDCs ($MoS_2$, $WS_2$ e $MoSe_2$ NS) usando la tecnica di esfoliazione in fase liquida (LPE). Usando questi nanosheet, abbiamo sintetizzato diversi nanocompositi che sono stati usati in seguito come layer sensibili verso diversi analiti in diversi settori applicativi.

**P**er i sensori elettrochimici, abbiamo scelto un dispositivo a basso costo e semplice da usare noto come elettrodo di carbonio serigrafato (SPCE) in cui l'elettrodo di lavoro viene modificato con diversi modificatori. Due campi diversi sono il nostro obiettivo; medicina e agricoltura. Per il primo abbiamo scelto l'acido folico (FA) e la dopamina (DA). Per quanto riguarda l'AF noto anche come vitamina B9, la sua determinazione è stata su AuNPs-MoS2 che mostra un nuovo meccanismo di rilevamento. Infatti, le molecole di FA sono fortemente adsorbite sulla superficie portando alla diminuzione del picco di corrente anodica invece del suo aumento quando si aumenta la concentrazione di FA. Questo fatto è dovuto alla riduzione del numero di siti attivi di nanoparticelle d'oro (AuNPs). Inoltre, la determinazione del DA è stata fatta su SPCE modificato con nanocomposito a base di MoSe2 e AuNP (AuNPs-MoSe2) notando un notevole miglioramento della corrente Faradica della DA . Per il settore agricolo, abbiamo utilizzato l'SPCE modificato con ossido di grafene-disolfuro di tungsteno (GO-WS2) per la determinazione di un fungicida noto come Thiram. Qui, abbiamo osservato una buona prestazione verso questo analita a bassa

concentrazione. Pertanto, abbiamo studiato l'effetto della variazione del rapporto GO:WS2 sul comportamento elettroanalitico.

**P**er i sensori plasmonici, abbiamo utilizzato i nanosheet esfoliati rivestiti con metallo nobile per il rilevamento di diversi analiti utilizzando enhanced Raman spectroscopies (ERS): la surface-enhanced Raman spectrosocopy (SERS) e la photo-induced enhanced Raman spectroscopy (PIERS). In effetti, lo strato di rilevamento Au-MoS2 viene utilizzato per determinare 4-mercaptobenzoic acid (MBA) e FA dove abbiamo notato una buona prestazione. Inoltre, le molecole MBA sono state utilizzate anche per verificare l'efficienza del substrato Au-WS2 dove le prestazioni PIERS sono migliori di quelle di SERS. Questo fatto è dovuto al trasferimento di carica da nanosheet WS2 e AuNP a causa della fase di pre-irradiazione UV-C in PIERS. L'ultimo substrato utilizzato come sensore plasmonico è costituito da MoSe2 e nanoroads d'oro (AuNRs) che viene utilizzato per rilevare il blu di metilene (MB). Da questo test, le prestazioni del SERS sono state buone e abbiamo notato un forte miglioramento sui segnali Raman mentre con i PIERS abbiamo osservato con un miglioramento ancor più significativo.

**T**utte queste indagini sono pubblicate o presentate in riviste con un fattore di impatto elevato. Questo lavoro è solo l'inizio di un lavoro più approfondito che sarà compiuto dopo la tesi.

# Table of Content

# List of Figures

# List of Tables

# List of Scheme

# General Introduction

The research has been oriented toward a new path in recent decades. Indeed, scientists have been interested in nanotechnology and nanomaterials thanks to their pros in human life. This technology is one of the fastest and most exciting moving areas of research today. Nanostructure materials are now used to facilitate so many daily tasks citing sensing, food quality control, solar cells, and electronics... Indeed, nanomaterials can be added to the usual ones to enhance their properties. Indeed, nanosilver, which has an antibacterial property that can be used in food contact material (cutting boards), creates small particles at the nanoscale to deliver cancer drugs or even turn polluted water into drinkable… Among these nanomaterials, two-dimensional (2D) materials have gained an important interest worldwide. It was in 2004 when Geim and Novoslov successfully exfoliated nanosheets from graphite, called graphene. Since that, numerous studies have attempted to understand and explore the specific properties of this material citing the optical transparency, mechanical resistance, and high electronic and thermal conductivity caused by the perfect electronic and vibrational confinement. Despite these outstanding features, graphene has a major drawback in that it is gapless and consequently its applications are limited. Hence, the researcher's curiosity is oriented to innovate new nanomaterials that satisfy the scientist's desire. As a result, the transition metal dichalcogenides (TMDCs) have been seen the sight in the research field like molybdenum disulphide ($MoS_2$), tungsten disulphide ($WS_2$), molybdenum selenide ($MoSe_2$)…

The main reason that makes this family the research's center of interest is their ability to transit from indirect to direct bandgap, from bulk to monolayer form, compared with graphene. Moreover, they possess a high volume-to-surface ratio, important Young's modulus, and high carrier mobility. These crucial features bring to this family a wide potential of applications citing the optoelectronic, electronic, and energy storage fields, especially in the sensing application.

Sensors have gained a crucial interest recently due to their use in daily life and to bypass significant issues. Therefore, it is important to develop a low-cost, sensitive, and selectivity sensor for the determination of probe molecules at low concentrations.

Consequently, the hybrid gold nanoparticles (AuNPs) with $MX_2$, which exalts several properties illustrate promising findings. Therefore, it is used in the sensing field with the help of developed techniques to enhance the probe molecule's fingerprint vibrational

modes. Thanks to the improved features of the hybrid AuNPs@$MX_2$, the sensor could be chemical, biological, or plasmonic.

This manuscript is divided into three major chapters. In the first one, we will present the history of two-dimensional (2D) materials, especially graphene and transition metal dichalcogenides (TMDCs). For the prior materials, we will indicate their properties and applications. Then, we will enumerate the different growth techniques of TMDCs materials mentioned in the bibliography. Furthermore, we will display several modifiers used in this investigation. Finally, we identify the sensor features and later we outline the two types in our focus.

In the second chapter, we will detail the experimental procedure used to synthesize the $MX_2$ nanosheets using the liquid phase exfoliation technique. Moreover, we will denote the elaboration methods used to grow gold nanoparticles (AuNPs). Later, we will illustrate the nanocomposite based on the exfoliated nanosheets and we will denote the various techniques of characterization performed to study the different features of our samples. Finally, we will specify the various analytes involved to check the sensing behaviour of our sensing layers.

The third chapter is depicted for the discussion of the obtained findings during this work. Since our goal is the development of two diverse types of sensors, this chapter is divided into two sub-chapters named electrochemical sensors and plasmonic sensors, respectively. Indeed, in the first sub-chapter, we will present the electrochemical and electroanalytical tests achieved with different $MX_2$ nanosheets either pure or as nanocomposites showing their sensing mechanism. In the second sub-chapter, we will illustrate the enhanced Raman spectroscopy (ERS) behaviour of each of $MoS_2$, $WS_2$ coated with gold nanoparticles toward the determination of 4-mercaptobenzoic acid (MBA) presenting in the second place the proposed ERS mechanisms. Furthermore, we used a new 2D-TMDCs material, known as molybdenum selenide ($MoSe_2$), coated with gold nanorods for the determination of dye molecule which is methylene blue (MB) ($10^{-4}$M) to check its efficiency in ERS field.

# Introduction

# Chapter I

## Introduction

### Table of Contents

# Chapter I

## Introduction

### Table of Figures

# Chapter I

# Introduction

## Acronyms and Abbreviations

All the abbreviation used in this chapter are listed below:

- 2D: Two-dimensional
- TMDCs: Transition metal dichalcogenides
- 3D: Three-dimensional
- 0D: Zero-dimensional
- 1D: One-dimensional
- $E_i$: Energy of ionization
- VdW: Van der Waals
- BG: Band gap
- MoS2: Molybdenum disulphide
- MoSe2: Molybdenum diselenide
- WS2: Tungsten disulphide
- CB: Conduction band
- VB: Valence band
- LPE: Liquid-phase exfoliation
- ME: Mechanical exfoliation
- SC: Sodium cholate
- NMP: 1-methyl-2-pyrrolidnone
- PLD: Pulsed laser deposition
- CVD: Chemical vapour deposition
- AuNPs: Gold nanoparticles
- ERS: Enhanced Raman spectroscopy
- SERS: Surface-enhanced Raman spectroscopy
- PIERS: Photo-induced enhanced Raman spectroscopy
- NS: Nanosheets

## Overview

In this section, we will dive into the history of two-dimensional (2D) materials and their vital role in current life. Moreover, we will enumerate the several techniques used in the 2D transition metal dichalcogenides (TMDCs) materials elaboration. Then, we will discuss the different criteria to classify sensors. Finally, we will depict the main sensor types used in these investigations.

## I. History

Materials at the nanoscale size possess outstanding and sometimes new features compared with their counterparts at the macroscale size. Indeed, the well-known definition of nanomaterials is those with sizes up to 100nm where the nanoparticles are nanoscaled in three dimensions (3D). Nanofilms and nanolayers are nanoscaled in two dimensions (2D). To have one-dimensional materials, only one dimension should be outside the nanoscale citing nanorods, nanotubes [1]… Finally, nanoparticles are the most known zero-dimension (0D) materials (with dimension < 100nm). Shrinking the size from one dimension to another results in electron confinement [2]. In this work, we have been interested in 2D materials for several reasons that are described in the next section.

### I.1. Why two-dimensional (2D) materials

In this section, we will attempt to motivate our choice of the 2D materials used in this thesis work. To begin, new and significant features come into view when shrinking the size of the bulk material. For instance, graphene, the familiar 2D material, shows better young's modulus, resistivity, and thermal conductivity compared with graphite [3]. Beyond graphene and its derivatives, 2D-transition metal dichalcogenide (2D-TMDCs) shows better and new features compared to their bulk counterparts like the indirect-to-direct bandgap crossover when decreasing the number of layers. In addition to these promising 2D materials, gold is known as the most precious material in the world that is yellow and shiny. However, this noble metal becomes red or purple when it is in the nanoscale (Figure I.1) due to the confinement of electrons [4], [5].

The diversity of the synthesis techniques is a promising parameter for their attractiveness that are not only low-cost but also simple and easy to use. Owing to the significant features of the 2D materials, they have become used in several fields such as energy storage, sensing, medicine…

***Figure.I. 1.****Gold change of colour at the nanoscale*

## I.2. History look through

The first exfoliation of graphene single-layer trial was made by Bordie in 1859 which end up with a failed attempt. Thus, R.E. Peierls, and L.D. Landau strictly suggested that 2D material could not exist in 1937. After 25 years, the graphene term is introduced by Hahns-Peter Bohm and for the first time, this material was exfoliated and characterized by two scientists Geim and Novoslov in 2004[2]. This prominent investigation was published in October 2004; "**Electric Field Effect in Atomically Thin Carbon Films**" in Science journal[3]. In 2010, they were awarded the Noble Prize in physics thanks to this accomplishment. Since that, various 2D materials have been exfoliated and used either in the development of several devices or to solve issues in current life.

## I.3. State of art

Graphene is an assembly of carbon atoms with a honeycomb structure (Figure I.2). Graphene is called later a 'miracle material', which possesses numerous properties. It is stronger (one hundred times) than steel (130GPa), as flexible as rubber, and more electrical than cobalt [8,9]. In 2014/2015, graphene was used in battery electrodes to boost performance. Despite its positive impacts, graphene has a major drawback, which is gapless. Consequently, its applications were limited and hence the discovery of the transition metal dichalcogenides (TMDCs) family at the beginning of 2011. Owing to the outstanding features of this family, it has gained crucial attention worldwide, which will be discussed in detail in the next section.

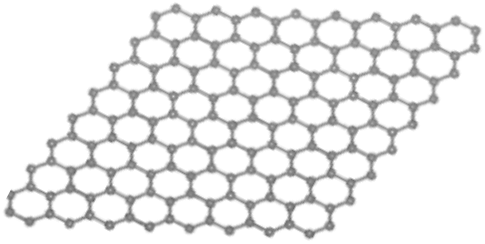

***Figure.I. 2.*** *Honey comb structure of Graphene*

## I.4. Morphologies of nano-materials

Nano-materials can be synthesized in different shapes and morphologies such as nanoparticles, nanowires, nanotubes, nanorods, and nanoribbons as shown in the following Figure I.3 [10].

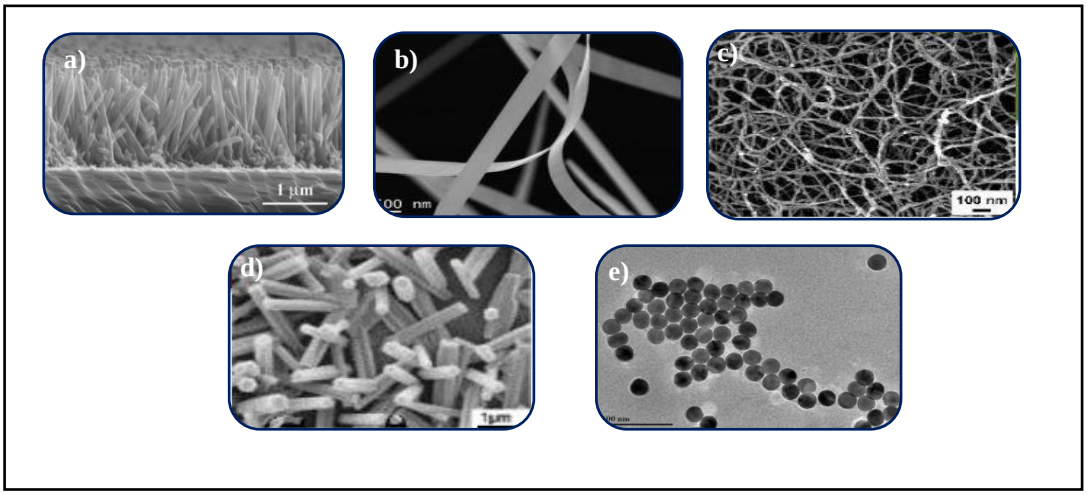


***Figure.I. 3.****TEM images of nano-materials (a) nanowires, (b) nanoribons, (c) nanotubes, (d)nanorods, and (e)nanoparticles*

# II. Transition metal dichalcogenides (TMDCs)

In this section, we will point out the importance of the transition metal dichalcogenide (TMDCs) family in various applications due to their outstanding properties. Before that, we will figure out these elements separately.

## II.1. Transition metal (M) and chalcogen (X) elements

Our center of interest in this thesis is the transition metal dichalcogenides family (TMDCs) with $MX_2$ as the chemical formula where M is the transition metal belonging to the d block ( V column) (M= Mo, W, Nb, Hf..) and X is the chalcogen (X= S, Se, Te.) belonging to p block (XIII column), see Figure I.4.

The transition metals (M) belong to d black and have (n-1)d subshell. Two different classification types are noted. The first one is according to the physical and chemical features of each element resulting in metal and non-metal elements. The second class is based on the d subshell and four transition series are distinguished in this family; 3d ($4^{th}$ period), 4d ($5^{th}$ period), 5d ($6^{th}$ period), and 6d ($7^{th}$ period).

These compounds are coloured and characterized by crucial features citing the high melting point, good conductivity, and low energy of ionization ($E_i$)…

The chalcogen (X) or oxygen family consists of the elements belonging to the 16 period of the periodic table including the non-metal elements (O, S, Se), and semi-metals (Te, Po). The electronic configuration of this family is $ns^2np^4$

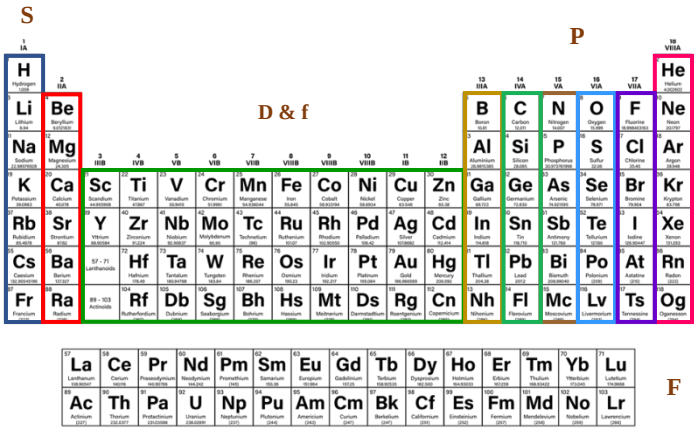


***Figure.I. 4.****The periodic table*

## II.2. Transition metal dichalcogenides family (TMDCs)

The 2D -TMDCs materials have a chemical formula $MX_2$ with M as the transition metal (Mo, W, Ti.) and X as the chalcogen (S, Te, Se…) see Figure I.5.a. In this family, the M atom plan is sandwiched between two X plans where the in-plane molecules are bonded with covalent bonds and the in-plane bonds are Van der Waals (VdW) bonds, see Figure I.5.b.

More than 40 TMDCs materials are depending on the combination of X and M, which can be metallic or semiconductor[11]. Indeed, the layers stack of $MX_2$ gives rise to three possible polytopes: 1T, 2H, and 3R (Figure I.6). Indeed, the digitals indicate the number of layers in the crystallographic unit cell while the alphabet letter displays tetragonal, hexagonal, and rhombohedral structures respectively. The first type has a $D_{3d}$ point group and octahedral coordination. The second is $D_{3h}$ and the third one is $C_{3v}$ with trigonal prismatic coordination.

The electronic behaviour and the thermodynamics of this family are sensitive to the polytype nature and number of layers. Indeed, 1T-TMDCs show a metallic behaviour while 2H and 3R-TMDCs polytypes display semiconducting behaviour. From the stability point of view, the 2H-phase that exists naturally is more thermodynamically stable than 1T and

3R (metastable) which are often found synthetic. The 3R phases can change to the 2H structure through heating, while the 1T phase can be transformed into a 2H phase via interlayer atomic gliding under specific conditions (2D layered transition).

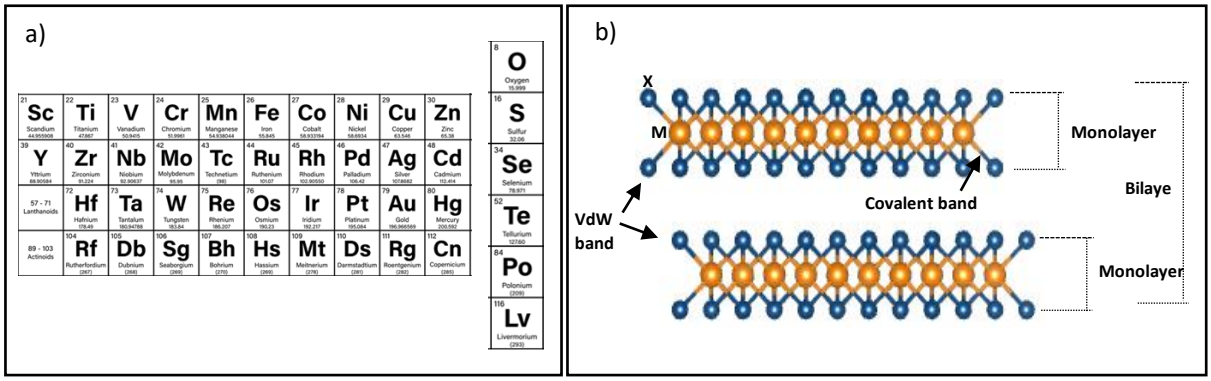


***Figure.I. 5.****(a) Transition metal and chalcogen families and (b) Structrue and bond types of MX2*

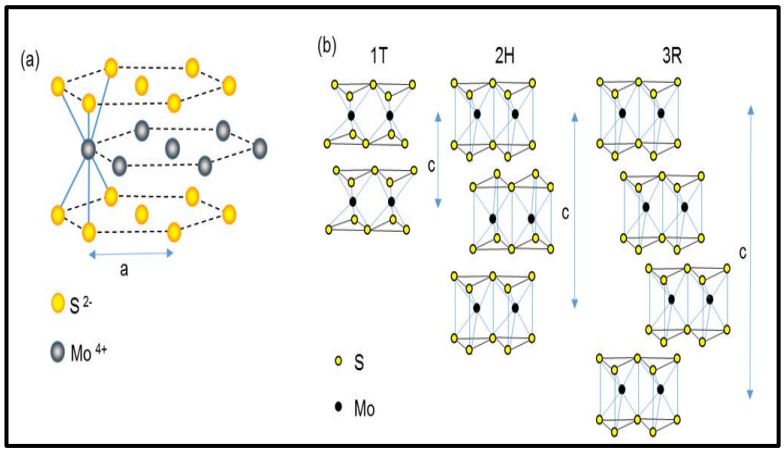


***Figure.I. 6.****TMDCs polytopes, for instance molybdenum disulphide (MoS2)*

The used metals disulphide ($MS_2$) in this work are molybdenum disulphide ($MoS_2$), tungsten disulphide ($WS_2$), and molybdenum diselenide ($MoSe_2$) which are black silvery gray, and brown powder in the bulk form (Figure.I.7). These 2D-$MS_2$ materials are inorganic compounds belonging to the TMDCs family where Mo (W) is the chemical symbol of molybdenum with the atomic number Z=42 (Z=16). The electronic configuration of Mo, W, and S are [Kr] $4d^5\ 5s^1$, [Xe] $6s^2\ 4f^{14}\ 5d^4$, and [Ne] $3s^2\ 3p^4$, respectively.

$MoS_2$ ($WS_2$) has an indirect bandgap equal to 1.23eV (1eV) that becomes a direct bandgap equal to 1.8eV (2eV) when it is a monolayer.

During recent decades, $MoS_2$ and $WS_2$ have been extensively studied for different application purposes. Unlike these nanomaterials, recently, molybdenum selenide ($MoSe_2$) gained interest worldwide due to its similar structure to $MoS_2$ and $WS_2$ and important features citing conductivity, high surface-to-volume ratio, high Young's modulus, and high carrier mobility (Figure.I.8) [13,12]… Thanks to these outstanding features, they have become the scientist's center of interest worldwide. $MS_2$ layered material features and applications will be described in the next sections.


***Figure.I. 7.****Bulk (a) molybdenum disulphide and (b) tungsten disulphide*

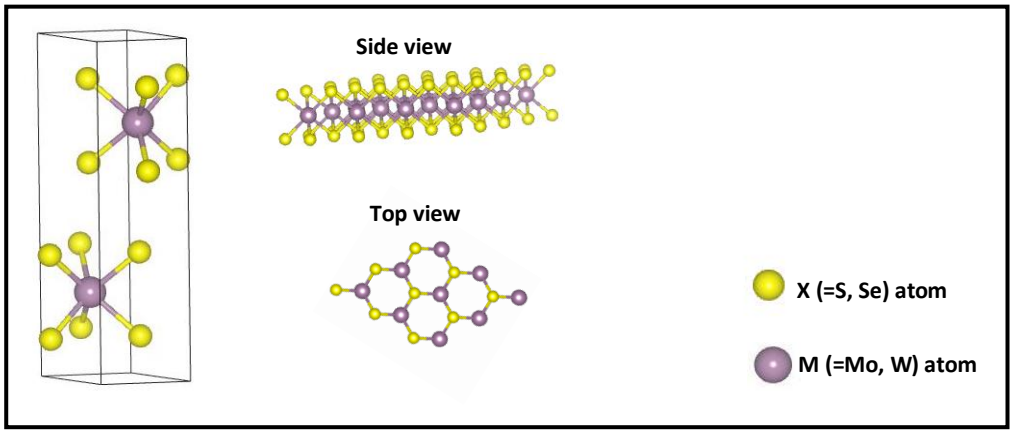


***Figure.I. 8.****MX2 sturcture*

## II.3. Features of transition metal dichalcogenides(TMDCs) materials

### II.3.a. Electronic Features

Two-dimensional materials cover the usual classes of electronic materials possessing excellent conductors (graphene), semiconductors ($MoS_2$, $MoSe_2$…), and insulators (h-BN). We can differentiate between them either with the band theory or with a physical parameter.

According to band theory, an insulator is a material that has a large bandgap where its energy is higher than 4eV while the semiconductor value is between 0 and 4eV ($0eV < E_{BG}$

⩽ 4eV). When we have an overlapping between the valence and conductor bandgap, we have a conductor (see Figure I.9).

Indeed, the bandgap is the energy range between the conduction band (CB) and the valence band (VB) that can be divided into two categories for the 2D semiconductors: direct and indirect bandgaps due to the k-vector (crystal momentum vector) between the minimal energy of CB and the maximum energy of VB (Figure I.10). Indeed, we have an indirect bandgap when the k-vector is different and in the case the similarity of this vector we have a direct bandgap.

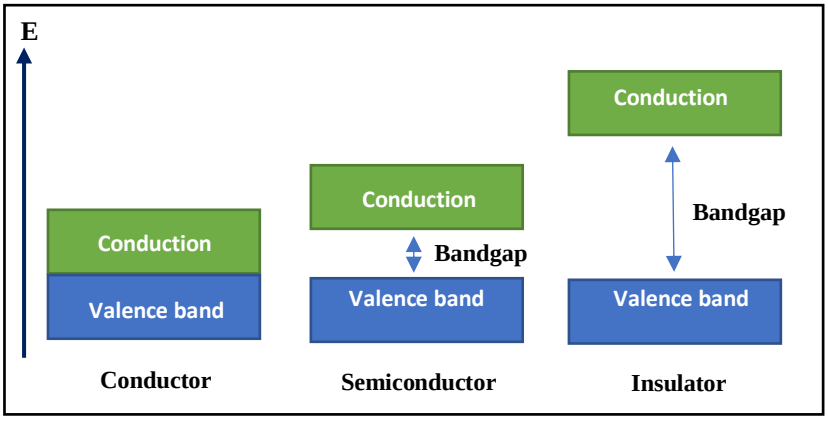


***Figure.I. 9.****Electronic state of TMDCs*

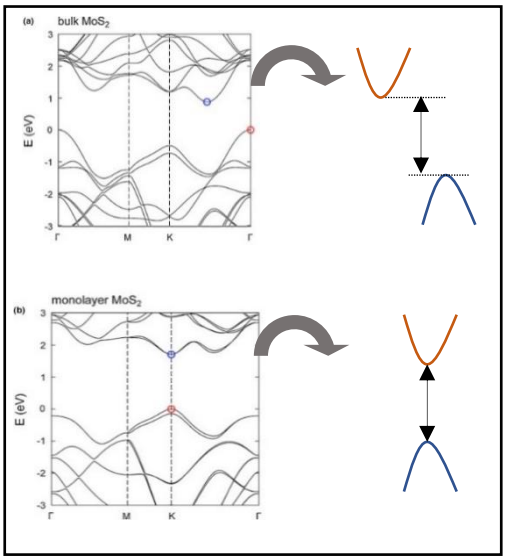


***Figure.I. 10.****(a) indirect and (b) indirect band gap of MoS2*

### II.3.b. Optical features

These TMDCs materials emit a fluorescence signal that is represented as bands in the photoluminescence spectrum. According to previous investigations, the fluorescence

signal of $MX_2$ materials is sensitive to their thickness[14, 15]. Moreover, the absorption spectrum of these materials is sensitive to the number of layers and from these data several, information can be extracted citing bandgap energy value, concentration, length, and the number of layers [16]… Despite the importance of these features, they were studied experimentally and no simulation is carried out [17].

### II.3.c. Mechanical properties

Young's modulus is named after the 19th-century British scientist Thomas Young. When the strain is applied in uniaxial, a relationship between strain (ε) and stress (σ) is defined as follows:

$$\mathbf{E}=\frac{\boldsymbol{\sigma}}{\boldsymbol{\varepsilon}}$$

This elastic modulus is expressed in Pascal (Pa) or $N/m_2$.

According to Zhang, R. & Cheung, R, an increase in the number of layers (thickness) possesses a decrease in Young's modulus of some 2D-materials, for instance, $MoS_2$, hexagonal boron nitride (h-BN), and black phosphorus (BP) [18]. In the work of Zhang, R. et al., they used the mechanical exfoliation technique to obtain $MoS_2$ nanosheets[18]. For one layer of $MoS_2$, Young's modulus is equal to 270±100 GPa, and for two layers of $MoS_2$ is equal to 200±60 GPa.

Thanks to the previously counted properties, two-dimensional inorganic materials display impressive promise in many applications, which will be cited in the next section.

## II.4. Applications of transition metal dichalcogenides family

Thanks to the fascinating features of the TMDCs materials described previously, they have been used in large and various fields denoting the energy storage field as solar cells, sensing field as chemical or biological sensors, or even in forensics and security (Figure I.11)[19], [20,21,22].

In industry, $MX_2$ materials can be used as a catalyst or lubricants due to their layered structure. The direct bandgap, as well as the high absorption coefficient of these two-dimensional layered materials, allows them to absorb a large part of the solar spectrum. As a result, they become the best candidates for the active element of a solar cell [23].

In electronics, the possibility of inserting chemical species between the sheets gives it a potential for application in the field of batteries[23] ( Li-ion batteries).

To sum up, 2D materials have become a promising candidates for several applications, especially in the sensing field. Thus, the 2D TMDCs family will be employed in this thesis work for two types of sensors that will be described later in this chapter.

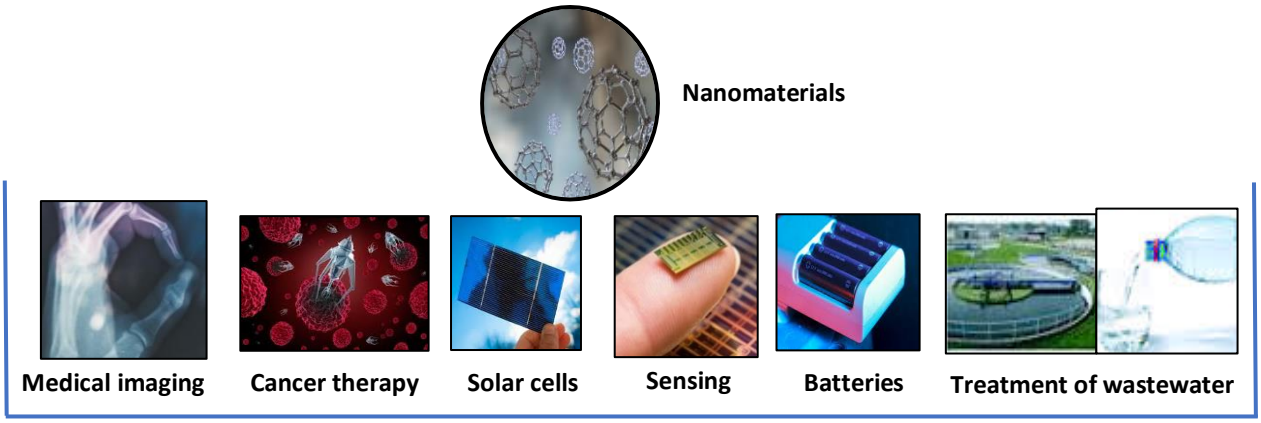


***Figure.I. 11.****Two-dimensional materials applications*

## III. Synthesis method

Since the exfoliation of graphene, several techniques have been used to produce 2D materials that are classified into two main sub-classes (Figure I.12). The first one is the top-down approach where we produce nanomaterials from their mother bulk while the second is the bottom-up approach where we start with principal components to obtain nanomaterials.

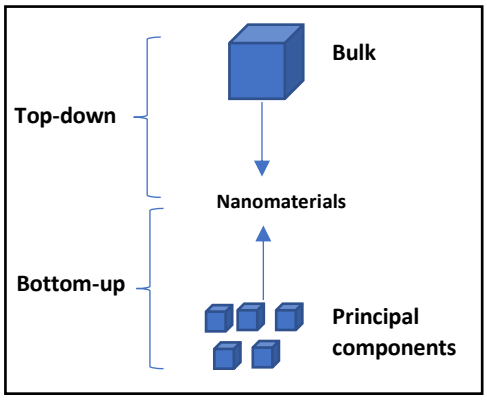


***Figure.I. 12.*** *A descriptive scheme of two approaches used for the synthesis of 2D materials*

### III.1. Top-down approach

The process of this approach is the production of nanomaterials from their bulk form by weakening the VdW bonds between the stacked layers of the bulk. The main advantage of this approach is low-cost, hence, this technique is preferred in numerous applications in many research areas. Nevertheless, problems such as defects in the structure of the surface can be encountered [24]. In the following, we denote several techniques that belong to the top-down approach.

### III.1.a.Mechanical exfoliation

Mechanical Exfoliation (ME) known also as a scotch tape technique, is a simple and cheap tool that has been used for the exfoliation of graphene from its bulk counterpart in 2004 by two scientists from Manchester University (United Kingdom) Geim and Novoslov. Since that, several 2D materials have been synthesized using this method. In fact, the ME technique is peeling or cleaving nanosheets using scotch tape from the bulk as illustrated in Figure I.13.


***Figure.I. 13.****Mechanical exfoliation steps; (a) scotch tape on graphite and (b) exfoliated graphene nanosheets*

The as-prepared samples are not uniform since their size and thickness are not controlled. Indeed, the provided thickness is around 4-10nm corresponding to 6-8 layers[2]. Nonetheless, the products obtained have high quality, purity, and clean single-layered flakes [25].

### III.1.b. Chemical exfoliation

In this technique, the $MX_2$ flakes are produced by putting the bulk material into some solvents to disperse denoting N-methyl-2-pyrrolidone (NMP), sodium cholate (SC), water…) [26,27]. Herein, the chemical exfoliation can be pure chemical or electrochemical peeling.

Chemical exfoliation or known also as liquid-phase exfoliation (LPE) is a low-cost technique that produces few or single layers from the bulk form by breaking the weak forces between sheets, see Figure I.14.a.

Electrochemical exfoliation, also called lithiation or lithium intercalation (Figure I.14.b), is a fascinating technique used to obtain large-scale monolayers. The ion-intercalated compounds are formed with the help of a cation with a small radius ($K^+$, $Li^+$, $Na^+$, $Cu^{2+}$…) that is intercalated into the spacing between bulk crystals [28,24]. Indeed, the layered bulk material is located at the cathode while Li foil is an anode in an electrochemical cell, which leads the obtaining a very high yield of TMDCs (e.g., $MoS_2$), however, this method requires a long time (days).

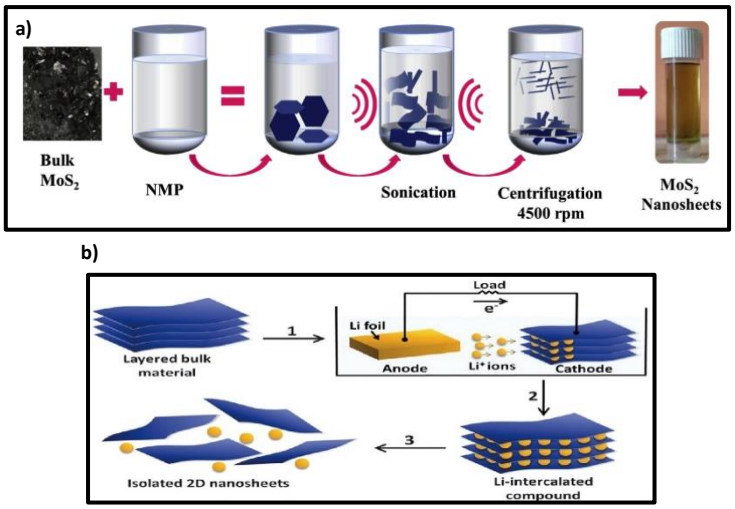


***Figure.I. 14.****(a) chemical and (b) electrochemical exfoliation steps methods*

### III.1.c. Pulsed laser deposition (PLD)

Pulsed laser deposition (PLD) or pulsed laser ablation (PLA) produces flakes or nanoparticles starting from the bulk material thanks to applied energy that came from laser irradiation breaking the interbond of bulk molecules to have the aimed nanoparticles [29].

## III.2. Bottom-up approach

In this approach, we start with atom-sized items and place them one by one to create the final product. This approach has many positive impacts, such as the well-defined morphology and shapes and the produced 2D material can be used in critical fields like electronic applications [30]. It introduces fewer defects as compared to the top-down approach, providing materials with more homogenous chemical compositions.

### III.2.a. Chemical vapour deposition (CVD)

Chemical vapour deposition (CVD), is a very popular and fast-developing technique for the bottom-up approach see Figure I.15. It is used to produce solid materials on a heated substrate with high-performance properties as well as high purity [31].

In this method, a reaction has occurred between two molecular precursors in a vaporized state at high temperatures (typically 700–900°C). For instance, the preparation of $MoS_2$ by this method is done by vaporizing $MoO_3$ and S precursors under Ar, or $N_2$ gas flow (transporter gas), preferably in a two-zone furnace for separate temperature control of both precursors and the as-prepared nanosheets (NS) are utilized for large-scale applications [32].

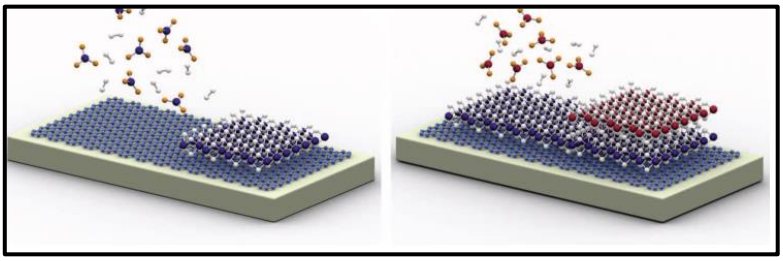

***Figure.I. 15.****CVD technique*

### III.2.b.Hydrothermal / Solvothermal technique

Hydrothermal /solvothermal is classified as a bottom-up technique, which is the most efficient, universal, and economical tool for the synthesis of 2D-$MX_2$ nanomaterials in solvent within which we can increase both pressure and temperature [33]. Based on the literature, we distinguished two different names for this technique depending solvent's nature; if it is water, so-called hydrothermal otherwise it is solvothermal (such as N, N-dimethylformamide (DMF), or NMP) [34,35]. In this technique, we begin by mixing the different solutions with powders. Then, this mixture is poured into the autoclave, which is chemically inert. Later, we close the autoclave and put it in the furnace where we can elevate both temperature and pressure, see Figure I.16 and Figure I.17.

***Figure.I. 16.****Hydrothermal autoclave reactor into furnace*

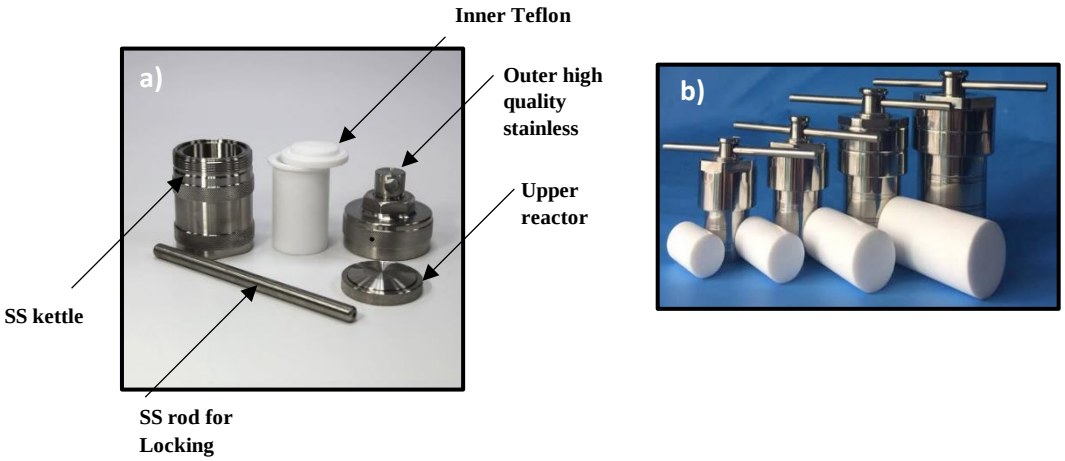


***Figure.I. 17.****Hydrothermal autoclave reactor (a) components and (b) sizes (50mL,100mL, 150mL, and 200ml)*

## IV. Modification of two-dimensional nanomaterials

Despite the fascinating features offered by 2D nanomaterials, we can improve these features and bring new ones for different applications by the modification of these nanomaterials with other elements or noble metals (gold (Au), silver (Ag)). In this investigation, we boost the properties of the 2D-TMDCs material by their modifications with graphene analogs (e.g. graphene oxide (GO)) and gold nanomaterials with different shapes (nanoparticles (NPs) and nanorods (NRs)).

### IV.1. Gold nanomaterials

In its natural state, gold is solid, yellow, and shiny with conventional use in jewelry. This matter belongs to the transition metals bloc in the periodic table symbolled with ‘Au’ with an atomic number (Z) equal to 79. Gold is inert i.e., extremely resistant to chemical action and it has more free electrons compared with d bloc’s elements leading to its good conductivity. These electrons are located on the surface of the noble metal, hence, the

interaction between light and Au causes large oscillations in the surface electromagnetic field [36]. This noble metal was also used in the coloring of glasses (400A.D) and stained glass, and the best-known example is the cup of Lycurgus (Figure I.18) dating from the IVe century AD. It was in 1857 that Michael Faraday synthesized pure gold particles in a solution for the first time.

***Figure.I. 18.****Cup of Lycurgus; in the right is enlightened by transmission and in the left by reflection*

Depending on the fabrication method, numerous morphologies (size and shapes) can be assumed from nanospheres up to nano-stars the AuNPs can be synthesized in different morphologies (nano-stars, nanowires, nano-triangles, nanorods)[37]. Figure I.19 illustrates the most prominent nanostructures[38].

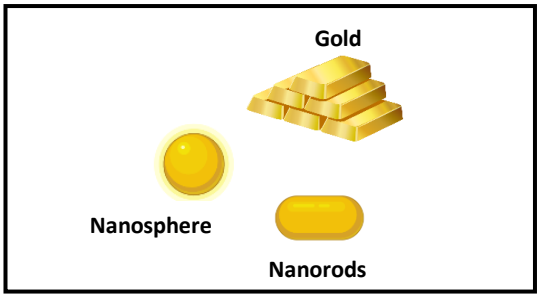


***Figure.I. 19.****Gold nanoparticles shape*

## IV.2. Graphene oxide (GO)

Graphene oxide (GO) is a derivative of graphene with a similar structure (honeycomb structure). This graphene analog is a non-stoichiometric compound with various potions of carbon, hydrogen, and oxygen where carbon is covalently functionalized with oxygen closing groups citing oxygen epoxides, and carbonyl groups (C=O), hydroxyl (-OH) … It has gained crucial potential in wide applications citing, energy storage, supercapacitors, electrochemical [31,32,33]... The significant attention toward GO is due to its important features denoting the large surface area (890 $m^2g^{-1}$) [34]. Moreover, GO is mechanically strong due to the high Young's modulus (207.6 ±23.4 GPa) [34].

The modification of the 2D nanomaterials with nanoscaled gold will improve the sensitivity of the obtained nanocomposite for several analytes and will improve its efficiency as an enhanced Raman scattering (ERS) substrate[35,36,37]. Moreover, the obtained nanocomposite based on GO will improve the sensitivity of 2D-TMDCs in electrochemical sensing [33, 38].

# V. Sensors before and after nanotechnology

## V.1. Definition

A sensor is a device able to detect a physical quantity (input) and converts it into a signal (output) which can be read by an observer or by an instrument. The input maybe light, heat, temperature, or molecule trace.

Up to now, sensors have different sizes from macro to nano (10nm-100nm). A nanosensor is a physical, biological, or chemical sensor that is built on the atomic scale (Figure I.20) [47]. These nanosensors are used in several applications such as medicine, drug discovery, food analysis quality and safety, and environment monitoring [48, 49, 50]… Nanosensors have numerous performance parameters that have been classified according to either the nature of the input quantity or the working principle of the sensor. We will describe the prior type of classification in the next sections.

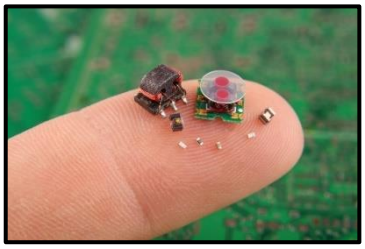

***Figure.I. 20.****Nanosensor size*

### V.1.a. Sensor before the nanotechnology revolution

Before time, professionals are making measurements after bringing the sample to the laboratory for detection using classical tools denoting nuclear magnetic resonance (NMR), chromatography, and electroanalytical methods such as voltammetry and potentiometry [40]... In this condition, we obtain selective analysis with a detection time goes to several hours. Owing to the advancement of science and technology, selective, sensitive, and real-time sensors have been launched in a smaller size.

### V.1.b. Sensor after the nanotechnology revolution

Nowadays, sensors have become smaller due to the need of human beings. We can create nanosensors to solve the current issues where various types of sensors can be found in our offices, cars, homes… Scientists are working daily since ever to make life easier like turning lights with simple crackling fingers, and detecting fire as well as hazardous gases… These and other automatic functions are possible thanks to sensors. However, to achieve these purposes, an efficient sensor must possess significant features that will be detailed in the following section.

## V.2. Characteristic features

Nanosensors have a great potential for application in wide fields such as medicine, national security, aerospace, biology as well as home safety, and many more. Thus, to have a useful and efficient sensor, it should be :

- **Selectivity:** is one of the fundamental parameters for a chemical sensor. It determines whether a sensor can respond selectively to an analyte or group of analytes.
- **Sensitivity:** described by the ratio of conductance change before and after the gas adsorption to its conductance in the absence of target gases [52].
- **Response time**: is the time taken by the sensor to respond to a concentration change step [53].
- **Recovery time:** The recovery time is the time appropriated by a gas sensor to return to its initial configuration once the environmental event ceases[31].
- **Reproducibility**: is the sensor's capacity to reproduce the same results in the same conditions and regardless of the number of times.
- **Linearity:** linear output signal to the amount of stimulus.
- **Accuracy:** is defined as how close the sensor is to the expected value. If for a given input, the output is expected to be a certain value accuracy is related to how close the sensor's output is to this value.

## V.3. Sensor types

According to the literature, various classifications are found to identify the sensor's type.

- **Depending on the nature of the analyte:** we have magnetic sensor, electrometer sensor, chemical, biological sensor…
- **According to the detection means:** they can be radioactive, electrochemical, plasmonic, biological…

To produce an output, a sensor can be active, which means an external power or excitation is needed. In the inverse case, we will have a passive sensor.

Depending on the output signals, we recognize two sub-classes; analog and digital. In the first type, the output is analogous to the measured input. Usually, the continuous output is voltage, e.g. temperature sensors. Regarding the digital sensor type, we will obtain digital data that can be read.

Among the various types of sensors, we are interested in plasmonic and electrochemical sensors where we chose to use the TMDCs materials and noble metals to develop these kinds of sensors due to their key role in our daily life.

### V.3.a. Electrochemical sensor

Based on the literature, several techniques have been used for the quantification citing spectrophotometry, high-performance liquid chromatography (HPLC), and spectrofluorimetric… Despite the selectivity and sensitivity of these techniques, they have multiple drawbacks such as high cost, time-consumer, and operation protocol difficulties that consist of the presence of a specialist.

To overcome these problems, electrochemical platforms, such as screen-printed electrodes (SPE), are used owing to their low cost, high sensitivity, and good analytical efficiency, see Figure I.21. Thus, they are extensively used in recent decades, especially for various fields citing biology, medicine, and food control due to their low cost, ease of use, as well as sensitivity [54, 55]. The SPE devices are plastic/ceramic cards that contain three types of electrodes called electrochemical cells. These electrodes are auxiliary, reference, and working electrodes that can be carbon, gold, or platinum.

These devices have been used in the bare form or modified by some materials to further develop their sensitivity and selectivity. Among these materials, we denote metal oxides (ZnO, CuO…), TMDCs, as well as graphene, and its analogs [56, 57]… The development of the working electrode (WE) of SPE's electrodes by the cited materials has opened a new path in analytical detection.

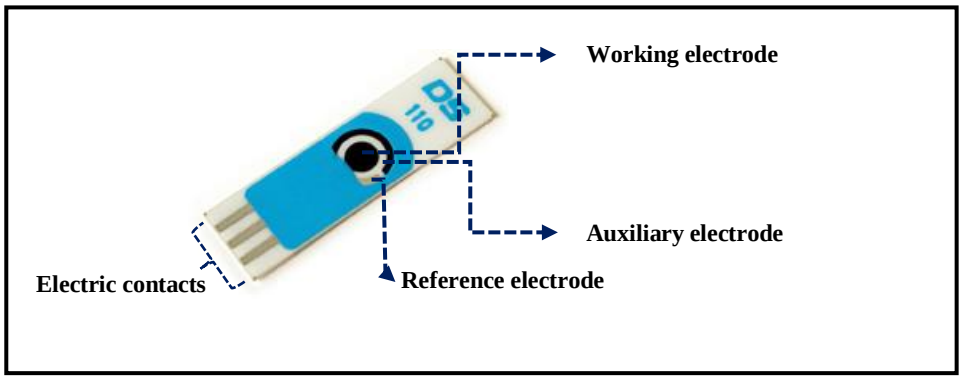


***Figure.I. 21.****Screen Printed Electrode (SPCE) components*

### V.3.b. Plasmonic sensor

Plasmonic sensors are those used based on the plasmonic noble metals either pure or in composite form. Over recent years, the use of this noble metal has undergone a crucial change owing to the free electrons in Au nanoparticles (NPs) interacting strongly with light under a specific light wavelength, which undergoes a collective oscillation [58].

This oscillation is known as a surface plasmon resonance (SPR). Besides these outstanding features, the stainless and inertness of Au NPs make them the best candidate for Raman enhancement techniques and electrochemical applications compared with other nanometals. Indeed, copper (Cu), silver (Ag), and platinum (Pt) have also been used to enhance Raman signals of the analyte.

These precious metals are used, therefore, as enhanced Raman scattering (ERS) substrates, which will be discussed later. Indeed, upon the interaction of the analyte on the plasmonic surface of the sensor, the signals will be enhanced due to the analyte-surface binding. This enhancement is due to the electromagnetic (EM) enhancement created by the interaction of the light bombarded on the plasmonic surfaces resulting in the surface plasmon. This fact is seen with surface-enhanced Raman spectroscopy (SERS). However, with photo-induced enhanced Raman spectroscopy (PIERS), the enhancement is further increased upon the UV-irradiation of the substrate that enhances the charge transfer (CT) between the substrate materials and the surface and the analyte, see Figure. I.22. Therefore, the enhancement of Raman signals will be enhanced more owing to CT enhancement and the further enhancement of EM leading to the boost of the global enhancement factor.

In this thesis investigation, we have coated the as-prepared $MX_2$ NS with gold nanorods (AuNRs) and gold nanoparticles (AuNPs) to create a developed plasmonic sensor.

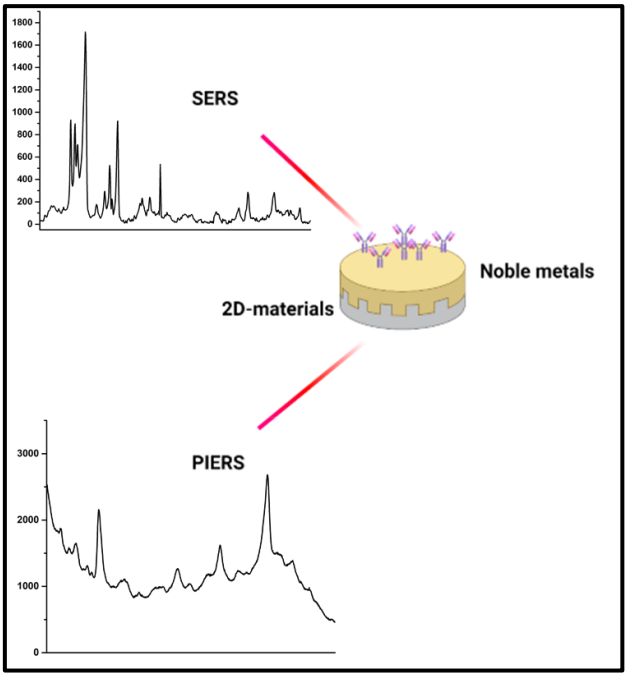


***Figure.I. 22.****ERS substrate enhancement*

# References


1. Shanmugam, V. *et al.* A Review of the Synthesis, Properties, and Applications of 2D Materials. *Particle & Particle Systems Characterization* **39**, 2200031 (2022).
2. Scher, J. A., Elward, J. M. & Chakraborty, A. Shape Matters: Effect of 1D, 2D, and 3D Isovolumetric Quantum Confinement in Semiconductor Nanoparticles. *J. Phys. Chem. C* **120**, 24999–25009 (2016).
3. Bharech, S. & Kumar, R. A Review on the Properties and Applications of Graphene. *Journal of Material Science and Mechanical Engineering (JMSME)* **2**, 70–73 (2015).
4. Pong, B.-K. *et al.* New Insights on the Nanoparticle Growth Mechanism in the Citrate Reduction of Gold(III) Salt: Formation of the Au Nanowire Intermediate and Its Nonlinear Optical Properties. *J. Phys. Chem. C* **111**, 6281–6287 (2007).
5. Why do gold nanoparticles show different colors? – nbccomedyplayground. https://www.nbccomedyplayground.com/why-do-gold-nanoparticles-show-different-colors/.
6. Geim, A. K. & Novoselov, K. S. THE RISE OF GRAPHENE. 14.
7. Novoselov, K. S. Electric Field Effect in Atomically Thin Carbon Films. *Science* **306**, 666–669 (2004).
8. Lee, C., Wei, X., Kysar, J. W. & Hone, J. Measurement of the Elastic Properties and Intrinsic Strength of Monolayer Graphene. *Science* **321**, 385–388 (2008).
9. Cao, K. *et al.* Elastic straining of free-standing monolayer graphene. *Nat Commun* **11**, 284 (2020).
10. Neri, G. First Fifty Years of Chemoresistive Gas Sensors. *Chemosensors* **3**, 1–20 (2015).
11. Nicolosi, V., Chhowalla, M., Kanatzidis, M. G., Strano, M. S. & Coleman, J. N. Liquid Exfoliation of Layered Materials. *Science* **340**, 1226419–1226419 (2013).
12. Jiang, F., Zhao, W.-S. & Zhang, J. Mini-review: Recent progress in the development of MoSe2 based chemical sensors and biosensors. *Microelectronic Engineering* **225**, 111279 (2020).
13. Li, T. *et al.* Two-Dimensional Material-Based Electrochemical Sensors/Biosensors for Food Safety and Biomolecular Detection. *Biosensors* **12**, 314 (2022).
14. Zhang, X. Characterization of Layer Number of Two-Dimensional Transition Metal Diselenide Semiconducting Devices Using Si-Peak Analysis. *Advances in Materials Science and Engineering* **2019**, 1–7 (2019).
15. McCreary, K. M., Hanbicki, A. T., Sivaram, S. V. & Jonker, B. T. A- and B-exciton photoluminescence intensity ratio as a measure of sample quality for transition metal dichalcogenide monolayers. *APL Materials* **6**, 111106 (2018).
16. Abid, K. *et al.* Photoinduced Enhanced Raman Spectroscopy with Hybrid Au@WS2 Nanosheets. *J. Phys. Chem. C* **124**, 20350–20358 (2020).
17. W, T. & Nm, R. S. and R. Electronic & Optical properties of transition-metal dichalcogenides. *MJNN* **2**, 60–66 (2017).
18. Zhang, R. & Cheung, R. Mechanical Properties and Applications of Two-Dimensional Materials. in *Two-dimensional Materials - Synthesis, Characterization and Potential Applications* (ed. Nayak, P. K.) (InTech, 2016). doi:10.5772/64017.
19. Santos, B. G. *et al.* Electrochemical sensor for isoniazid detection by using a WS2/CNTs nanocomposite. *Sensors and Actuators Reports* **4**, 100073 (2022).
20. Guang, Q., Huang, B. & Li, X. Au-Decorated WS2 Microflakes Based Sensors for Selective Ammonia Detection at Room Temperature. *Chemosensors* **10**, 9 (2022).

21. Abid, I. *et al.* Plasmon damping and charge transfer pathways in Au@MoSe2 nanostructures. *Materials Today Nano* **15**, 100131 (2021).
22. Mulpur, P., Yadavilli, S., Rao, A. M., Kamisetti, V. & Podila, R. MoS2/WS2/BN-Silver Thin-Film Hybrid Architectures Displaying Enhanced Fluorescence via Surface Plasmon Coupled Emission for Sensing Applications. *ACS Sens.* **1**, 826–833 (2016).
23. Soltane, M. A. Etude des propriétés électroniques et structurales du semiconducteur lamellaire MoS2 pour une application photovoltaïque. 84.
24. Murugan, C., Sharma, V., Murugan, R. K., Malaimegu, G. & Sundaramurthy, A. Two-dimensional cancer theranostic nanomaterials: Synthesis, surface functionalization and applications in photothermal therapy. *Journal of Controlled Release* **299**, 1–20 (2019).
25. Omkaram, I., Hong, Y. K. & Kim, S. Transition Metal Dichalcogenide Photodetectors. *Two-dimensional Materials for Photodetector* (2017) doi:10.5772/intechopen.72295.
26. Photoinduced Enhanced Raman Spectroscopy with Hybrid Au@WS2 Nanosheets | The Journal of Physical Chemistry C. https://pubs.acs.org/doi/10.1021/acs.jpcc.0c04664.
27. Tyurnina, A. V. *et al.* Ultrasonic exfoliation of graphene in water: A key parameter study. *Carbon* **168**, 737–747 (2020).
28. Hu, R., Huang, Z., Wang, B., Qiao, H. & Qi, X. Electrochemical exfoliation of molybdenum disulfide nanosheets for high-performance supercapacitors. *J Mater Sci: Mater Electron* **32**, 7237–7248 (2021).
29. Habiba, K., Makarov, V., Weiner, B. & Morell, G. Fabrication of Nanomaterials by Pulsed Laser Synthesis. in 263–291 (2014). doi:10.13140/RG.2.2.16446.28483.
30. Turki, R. *et al.* Luminescent Sm-doped aluminosilicate glass as a substrate for enhanced photoresponsivity of MoS2 based photodetector. *Applied Surface Science* **565**, 150342 (2021).
31. Habba, Y. G. Étude des nanostructures de ZnO pour leur application dans l'environnement: détection de gaz et dépollution de l'eau. 167.
32. Velický, M. & Toth, P. S. From two-dimensional materials to their heterostructures: An electrochemist's perspective. *Applied Materials Today* **8**, 68–103 (2017).
33. Wu, M. *et al.* Molybdenum disulfide (MoS2) as a co-catalyst for photocatalytic degradation of organic contaminants: A review. *Process Safety and Environmental Protection* **118**, 40–58 (2018).
34. Wang, S. *et al.* Hydrothermal Synthesis of Molybdenum Disulfide for Lithium Ion Battery Applications. *Chinese Journal of Chemical Engineering* **18**, 910–913 (2010).
35. Akram, H. *et al.* Solvothermal Synthesis and Characteriszation of Hollow nanospheres Molybdenum Sulfide. *Journal of Nanoscience and Nanotechnology* (2012).
36. Peveler, W. J., Jaber, S. B. & Parkin, I. P. Nanoparticles in explosives detection – the state-of-the-art and future directions. *Forensic Sci Med Pathol* **13**, 490–494 (2017).
37. Khoa, N. T., Kim, S. W., Yoo, D.-H., Kim, E. J. & Hahn, S. H. Size-dependent work function and catalytic performance of gold nanoparticles decorated graphene oxide sheets. *Applied Catalysis A: General* **469**, 159–164 (2014).
38. Dobrowolska, P. *et al.* Application of Turkevich Method for Gold Nanoparticles Synthesis to Fabrication of SiO2@Au and TiO2@Au Core-Shell Nanostructures. *Materials* **8**, 2849–2862 (2015).
39. Fabrication of Graphene Oxide Supercapacitor Devices | ACS Applied Energy Materials. https://pubs.acs.org/doi/10.1021/acsaem.7b00164.
40. Park, M.-A. *et al.* Bifunctional Graphene Oxide Hole-Transporting and Barrier Layers for Transparent Bifacial Flexible Perovskite Solar Cells. *ACS Appl. Energy Mater.* **4**, 8824–8831 (2021).

41. Chen, D., Feng, H. & Li, J. Graphene Oxide: Preparation, Functionalization, and Electrochemical Applications. *Chem. Rev.* **112**, 6027–6053 (2012).
42. What is the Difference Between Graphene Oxide and Reduced Graphene Oxide. *Nanografi Nano Technology* https://nanografi.com/blog/what-is-the-difference-between-graphene-oxide-and-reduced-graphene-oxide/.
43. Abid, K. *et al.* Photoinduced Enhanced Raman Spectroscopy with Hybrid Au@WS2 Nanosheets. *J. Phys. Chem. C* **124**, 20350–20358 (2020).
44. Brognara, A. *et al.* New Mechanism for Long Photo-Induced Enhanced Raman Spectroscopy in Au Nanoparticles Embedded in TiO2. *Small* **18**, 2201088 (2022).
45. Zhao, J. *et al.* Recent advances and perspectives in photo-induced enhanced Raman spectroscopy. *Nanoscale* **13**, (2021).
46. Krishnamoorthy, D. & Prakasam, A. Graphene Hybridized with Tungsten disulfide (WS2) Based Heterojunctions Photoanode Materials for High Performance Dye Sensitized Solar Cell Device (DSSCs) Applications. *J Clust Sci* **32**, 621–630 (2021).
47. Dahman, Y. Nanosensors**By Yaser Dahman, Amira Radwan, Boris Nesic, and Jason Isbister. in *Nanotechnology and Functional Materials for Engineers* 67–91 (Elsevier, 2017). doi:10.1016/B978-0-323-51256-5.00004-6.
48. Ibáñez, D., Izquierdo-Bote, D., González-García, M. B., Hernández-Santos, D. & Fanjul-Bolado, P. Development of a New Screen-Printed Transducer for the Electrochemical Detection of Thiram. *Chemosensors* **9**, 303 (2021).
49. Curulli, A. Electrochemical Biosensors in Food Safety: Challenges and Perspectives. *Molecules* **26**, 2940 (2021).
50. Pérez-Fernández, B., Costa-García, A. & Muñiz, A. de la E.-. Electrochemical (Bio)Sensors for Pesticides Detection Using Screen-Printed Electrodes. *Biosensors* **10**, 32 (2020).
51. Qriouet, Z. *et al.* Analytical Methods Used for the Detection and Quantification of Benzodiazepines. *Journal of Analytical Methods in Chemistry* **2019**, 1–11 (2019).
52. Pu, H. Novel Two-dimensional Nanomaterials and Their Gas Sensing Properties. 238.
53. (PDF) Gas Sensors: A Review. https://www.researchgate.net/publication/285988329_Gas_Sensors_A_Review.
54. Lu, H., He, B. & Gao, B. Emerging electrochemical sensors for life healthcare. *Engineered Regeneration* **2**, 175–181 (2021).
55. Zeng, L., Peng, L., Wu, D. & Yang, B. *Electrochemical Sensors for Food Safety*. *Nutrition in Health and Disease - Our Challenges Now and Forthcoming Time* (IntechOpen, 2018). doi:10.5772/intechopen.82501.
56. Melinte, G. *et al.* Selective Detection of Folic Acid Using 3D Polymeric Structures of 3-Carboxylic Polypyrrole. *Sensors* **20**, 2315 (2020).
57. Bressi, V., Ferlazzo, A., Iannazzo, D. & Espro, C. Graphene Quantum Dots by Eco-Friendly Green Synthesis for Electrochemical Sensing: Recent Advances and Future Perspectives. *Nanomaterials* **11**, 1120 (2021).
58. Jaber, S. B. & Parkin, I. Evaluation of Gold and Silver Nano Spherical Efficiency for Enhancing Raman Scattering of Explosives. *undefined* (2018).

# Methods and Materials

# Chapter II

## Methods & Materials

### Table of Contents

# Chapter II

## Methods & Materials

### Table of Figures

# Chapter II

## Methods & Materials

### Table of Scheme

# Chapter II

# Methods and Materials

## Acronyms and Abbreviations

All the abbreviation used in this chapter are listed below:

- 2D: Two-dimensional
- TMDCs: Transition metal dichalcogenides
- VdW: Van der Waals
- $MoS_2$: Molybdenum disulphide
- $WS_2$: Tungsten disulphide
- $MoSe_2$: Molybdenum diselenide
- VdW: Van der Waals
- H-BN: Hexagonal boron nitride
- BP: Black phosphorus
- ERS: Enhanced Raman spectroscopy
- SERS: Surface-enhanced Raman spectroscopy
- TERS: Tip-enhanced Raman spectroscopy
- PIERS: Photo-induced enhanced Raman spectroscopy
- SERRS: Surface-enhanced resonance Raman spectroscopy
- HPLC: High-performance liquid chromatography
- SPCE: Screen-printed carbon electrode
- WE: Working electrode
- LPE: Liquid phase-exfoliation
- DI: Deionized water
- SEM-EDX: Scanning electron microscopy- energy dispersive X-ray spectroscopy
- UV-Vis : Ultra-violet visible
- DLS: Dynamic light scattering
- CV : Cyclic voltametric
- DPV: Differential pulse voltammetry
- LSV: Linear sweep voltammetry
- SWV: Square wave voltammetry

- MBA: 4-mercaptobenzoic acid
- FA: Folic acid
- DA: Dopamine

### Overview

In this chapter, we will deep into the chosen method to synthesize two-dimensional (2D) layered transition metal dichalcogenides (TMDCs) and 2D-gold with different shapes. Besides, we will present the diverse characterization techniques used in this work to understand the optical and electronic properties of our samples. In the second section of this chapter, we will illustrate the preparation of sensing layers for electrochemical and plasmonic sensors. Finally, we will depict the different probe molecules used for the sensing process.

# I. Sample synthesis

## I.1. Synthesis method: liquid phase exfoliation (LPE)

As mentioned in the previous chapter, two main categories are distinguished. The first mechanical exfoliation or the scotch tape technique is used by two scientists from Manchester University in 2004 to peel off graphene sheets from the graphite (bulk form) [1]. Since that, this technique has been used to exfoliate various TMDCs 2D materials. Indeed, it consists of the break of the VdW band between TMDCs planes using scotch tape (Figure II.1).

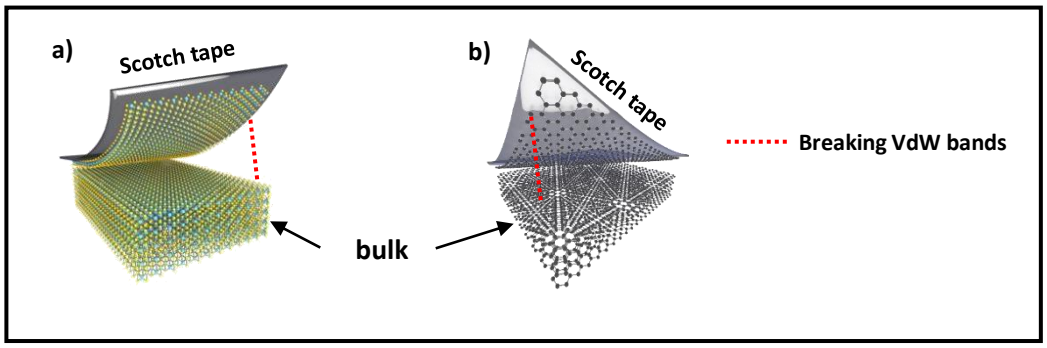


***Figure.II. 1.*** *Mechanical exfoliation of (a)TMDCs and (b) graphene*

In this investigation, we have chosen a top-down technique known as liquid-phase exfoliation (LPE) for the production of $MX_2$ nanosheets (NS). Herein, we will argue our choice. Indeed, the top-down approach is the production TMDCs nanomaterials from the bulk form based on the exfoliation technique, either mechanical or chemical where chemical exfoliation produces nanosheets with high quality than mechanical. This technique can produce up to 10 layers with lengths in the range of 350nm [2, 3, 4, 5]. Compared with this approach, bottom-up methods produce uniform and high-quality TMDC layers. However, this requires high-cost precursors. As our goal is to create a low-cost developed

electrochemical/plasmonic sensor with high-quality TMDCs layers, we have chosen the LPE technique to exfoliate $MX_2$ NS in five simple steps as follows (e.g. $MoSe_2$):

We mix 150mg of $MoSe_2$ commercial powder with 45mg of sodium cholate (SC) in 30mL of deionized water (DW), Figure 8.a-b. Later, this solution is horn sonicated in an ice bath for 45mn (Figure II.2.c). After a night, we obtained dispersions in a flask that were centrifugated at two different power (1.5Krpm and 5Krpm) (Figure II.2.d). The obtained dispersions are stable for months (Figure II.2.e-f). . The same procedure is done to obtain $MoS_2$ and $WS_2$ sheets.

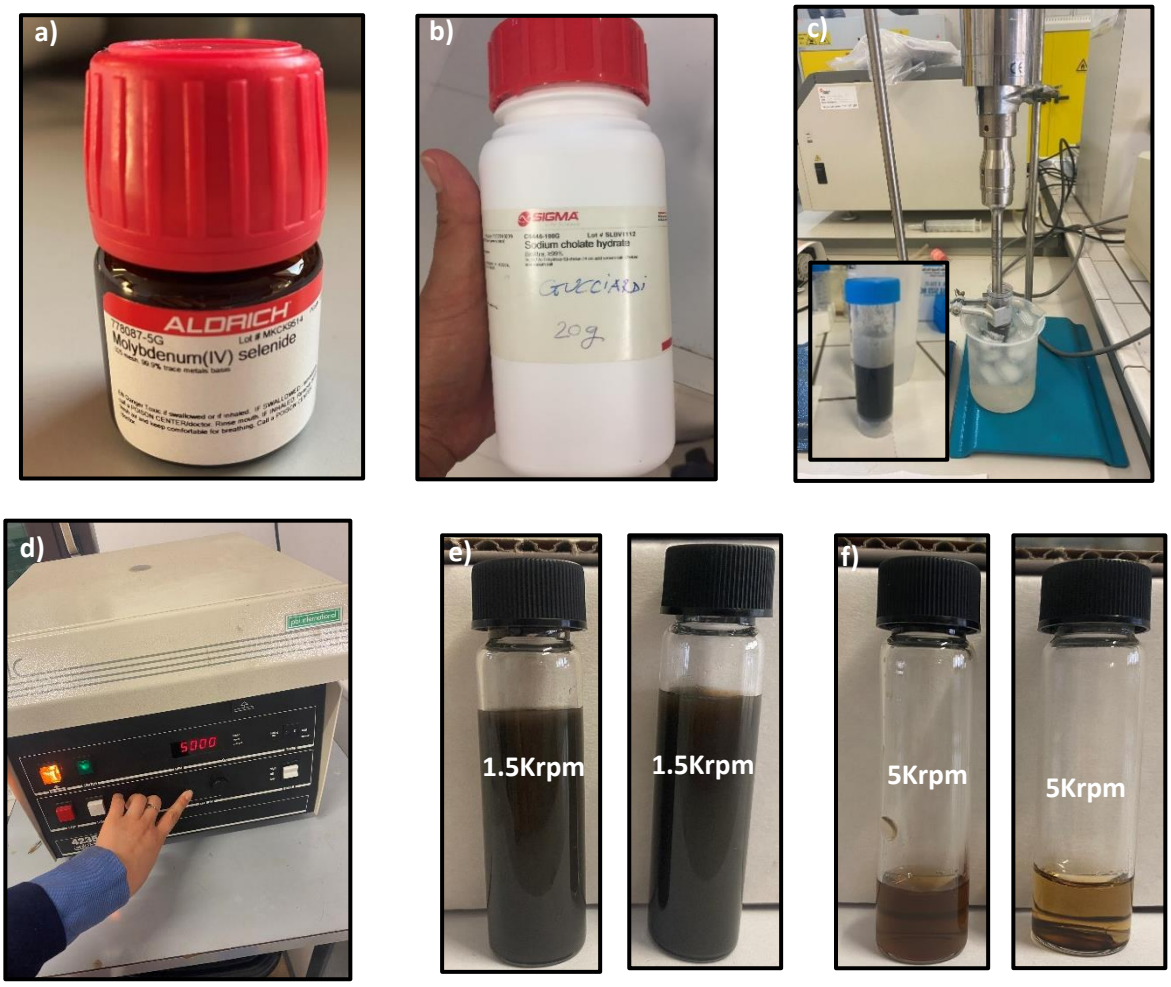


***Figure.II. 2.*** *LPE technique steps: (a) MoSe2 commercial powder, (b) sodium cholate powder, (c) sonication of MoSe2 in SC watery solution. Inset the solution after sonication, (d) centrifugation of the supernatant, (e) before and after MoSe2 centrifugation at 1.5Krpm, (f) at 5Krpm*

## I.2. Synthesis of gold nanoparticles (AuNPs)

Owing to the importance of Au nanoparticles (AuNPs) in the sensing field as pure or nanohybrid form, various techniques were used to achieve its synthesis citing the

electrochemical, thermal, and chemical approaches [6]. In the following, we will describe the used pathways to elaborate gold nanomaterials for this investigation.

### I.2.a. Turkevich-Frens method

In 1951, Turkevich set up a simple protocol for the synthesis of AuNPs that was controlled by Frens later (in 1973)[6,7,8]. In this method, we dissolve 120mg of chloroauric acid ($HAuCl_4$) in boiling water (250mL), then, we add 25mL sodium citrate solution (1% w/w). After 1h of boiling, we precipitated the AuNPs using ultra-centrifugation and re-suspended them in methanol, see scheme II.1.

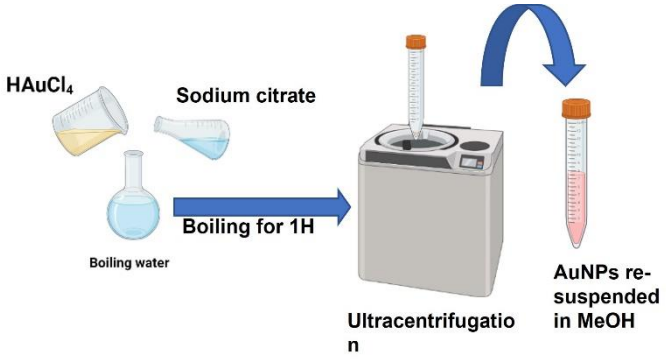


***Scheme.II. 1.*** *Scheme presenting the synthesis of AuNPs using Turkevich-Frens method*

### I.2.b. Green-synthesis approach

As described previously, gold nanoparticles (AuNPs) are crucial for sensors and several techniques are used to elaborate them citing Turkish-Frens, green synthesis [11, 12, 13]… In this investigation, we chose a green synthesis pathway to obtain AuNPs based on three components; natural honey, DW, and gold chloride ($HAuCl_4$), (Figure.II.3. a-b). Herein, two solutions were prepared. In the first one, we mix 25mg of $HAuCl_4$ with 60mL of DI. In the second, in 25mL of DW, we dissolve 10g of honey, Figure.9.c. Later, we mix 12.5mL of the aqueous honey solution with 15mL $HAuCl_4$ solution and stirred strongly for 3h to obtain a violet solution, Figure II.3.d-e. To remove any honey residues and to get only the AuNPs, we centrifuge the obtained violet solution at 13.5Krpm, see Figure II.3. f-g.

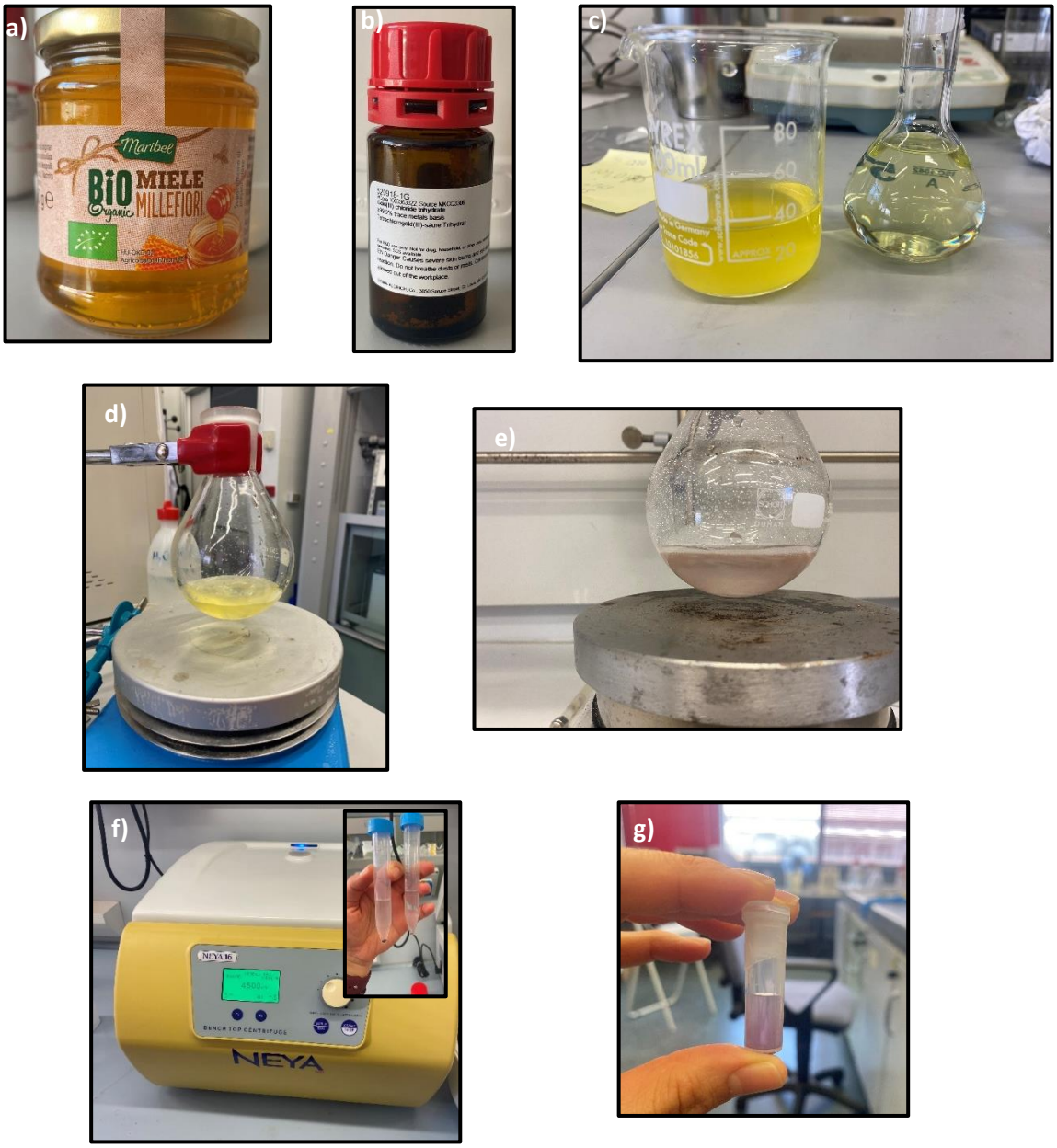


***Figure.II. 3.*** *AuNPs green synthesis; (a) honey , (b) gold chloride, (c) honey and HAuCl4 solutions, (d) before (e) after the stirring solution (violet solution), (f) centrifugation. Inset the obtained AuNPs solution after centrifugation, and (g) the obtained AuNPs with green synthesis*

## I.3. Graphene oxide:Tungsten disulphide ($GO@WS_2$) nanocomposite

To study the effect of TMDCs on the sensing behaviour of graphene oxide (GO), we have prepared $GO@WS_2$ nanocomposite. First, we dispersed 10 mg of GO in 2 mL of denoised water, Figure.II.4. By mixing GO with $WS_2$, we prepare different nanocomposites at different ratios of GO: $WS_2$ (i.e 1:1, 2:1, and 1:2), to develop three nanocomposite samples. These nanohybrids were mixed by simple stirring for 2h at room temperature.

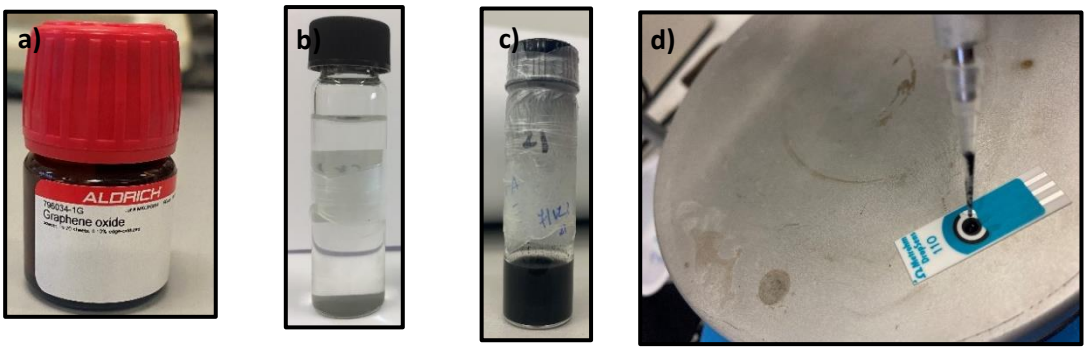


***Figure.II. 5.*** *Preparation of GO@WS2 nanocomposite; (a) graphene oxide commercial powder, (b) WS2 dispersions, (c) GO@WS2 nanocomposite, (d) modifying the WE with GO@WS2 through drop casting*

## I.4. Electrode modification

The working electrode (WE) of the SPCE device is modified to further improve its sensitivity. The modifier in this work will be 2D-TMDCs nanosheets ($MoS_2$, $WS_2$, $MoSe_2$) and nanohybrids (Au@$MoS_2$, GO@$WS_2$, Au@$MoSe_2$). Indeed, the modification is achieved by drop-casting into WE. Scheme.II.2 presents a scheme for the synthesis process of the nanosheets, AuNPs, and the modification of SPCE with Au@$MoSe_2$ nanohybrid.

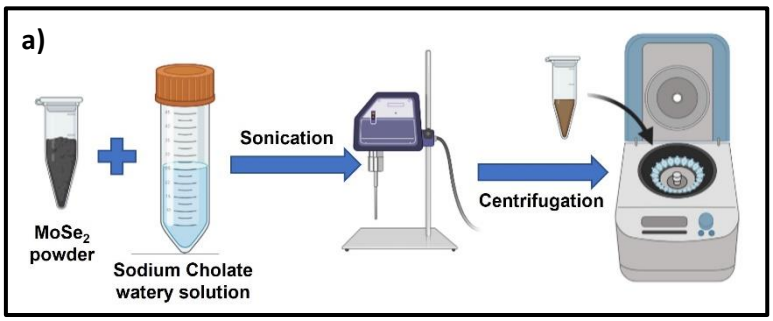


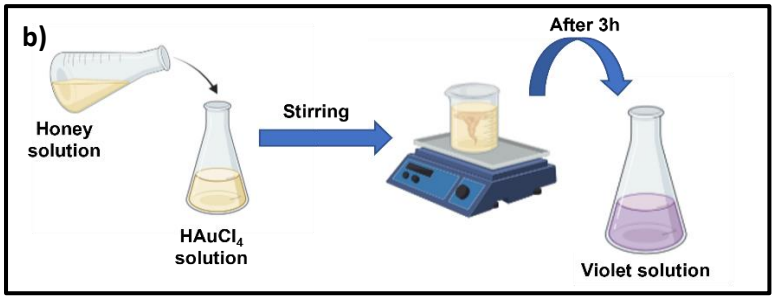

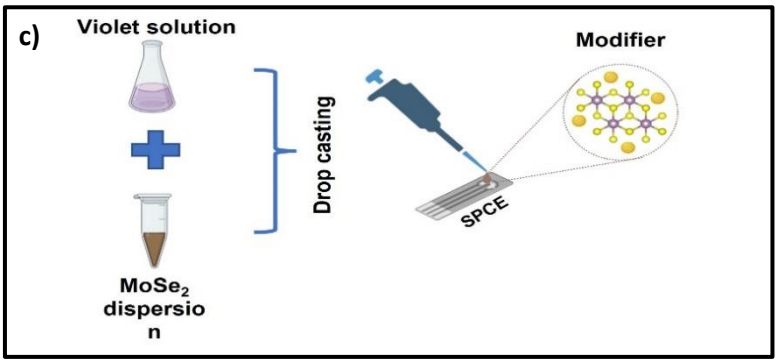


***Scheme.II. 2.****Schematic experimental diagram of (a) Liquid phase exfoliation (LPE) of MoSe2, (b) green synthesis of gold nanoparticles (AuNPs), and (c) modification of screen printed carbon electrodes (SPCE)*

## I.5. Enhanced Raman spectroscopy (ERS) substrate preparation

For the enhanced Raman spectroscopy (ERS) substrates, we prepared AuNPs@$WS_2$ and AuNRs@$MoSe_2$(5Krpm) by drop-casting the solution onto a glass slide and leave to dry at room temperature.

For the SERS measure of AuNRs@$MoSe_2$(5Krpm) substrate, we mixed in the first place $MoSe_2$ (5Krpm) dispersion with gold nanorod (AuNRds) and drop cast onto a glass slide 50µL and put it dry at room temperature. Once the substrate is dried, we immersed it in the analyte solution for 2 hours (Figure.II.5.a-b). For the PIERS measure, we put the substrate at a 1cm distance for 2 hours, see Figure.II.5.c.

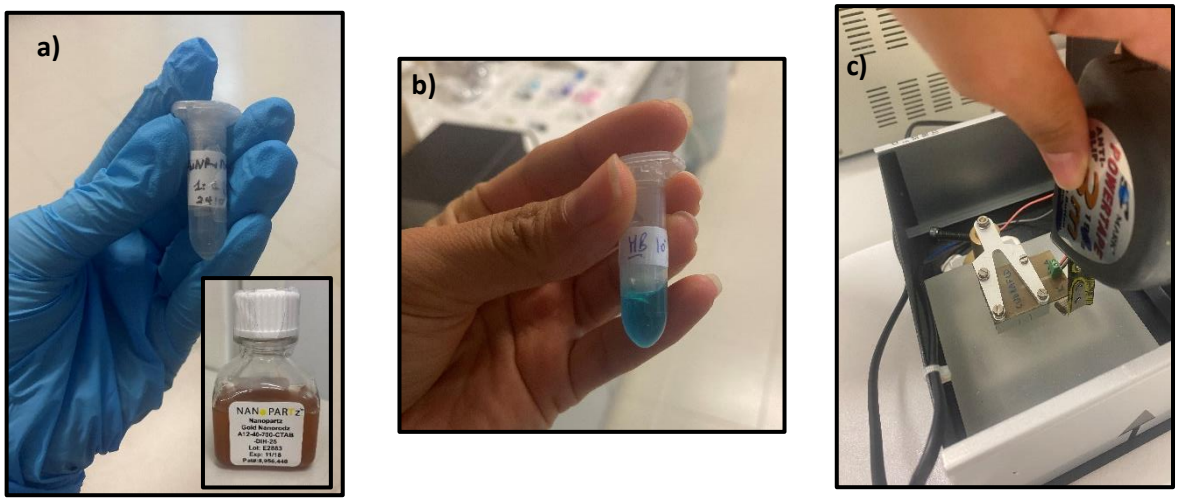


***Figure.II. 6.****AuNRs-MoSe2(5Krpm) ERS susbtrate preparation; (a) AuNRs@MoSe2 solution. inset commercial AuNRs, (b) immersion of the susbtrate in MB (10-4M), (c) 1cm distance between substrate and the irradiation source in PIERS setup*

# II. Characterization techniques

Spectroscopy is the study of matter and electromagnetic radiation where we distinguished various categories according to the nature of the energy-material interaction including absorption, emission spectroscopies, and inelastic scattering…

In order to study the optical and vibrational features of our $MX_2$ nanosheets and our sensors, we have used different techniques; vibrational technique (Raman, FT-IR), optical tools (photoluminescence (PL), Ultra-violet (UV)), morphological techniques (SEM-EDX, DLS), and enhanced Raman enhancement spectroscopies (ERS). In the following, we present the basics and principles of these techniques.

## II.1. Vibrational techniques

### II.1.a. FTIR technique: introduction and principe

❖ **Introduction:** Fourier transform infrared (FT-IR) spectroscopy is a non-destructive analysis technique giving an infrared spectrum of the specimen (gas, solid, liquid) based on Fourier transform, which is a mathematical process (Figure II.6.). Both the appearance of the FTIR tool and the developed algorithm by Cooley-Turkey were timelined between 1960-1966.

❖ **Principe:** An infrared light interacted with the molecules of the sample. This interrogation results in the observation of vibrational bonds at specific frequencies. All the bonds form the characteristic fingerprint spectrum of each molecule

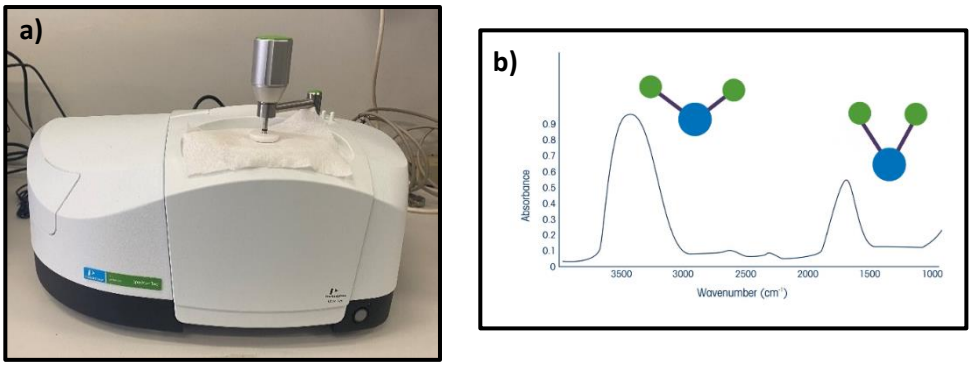


***Figure.II. 7.(a)*** *The used FT-IR spectroscopy at LabSensor, (b) fingerprint spectrum of organic/inorganic compound*

### II.1.b. Raman spectroscopy

❖ **Introduction:** Raman spectroscopy is a non-destructive and highly versatile vibrational spectroscopy discovered by the Indian Chandrashekhara Venkata Raman (C.V.Raman) in 1928 (Figure II.7). This spectroscopy is a tool for analyzing the scattered light to determine the molecular/crystal structure of probe molecules. Each molecule has a specific Raman band position and intensity that are actual molecular fingerprints. Most organic and inorganic matter, solids, gases, and liquids are allowed to be characterized by Raman spectroscopy.

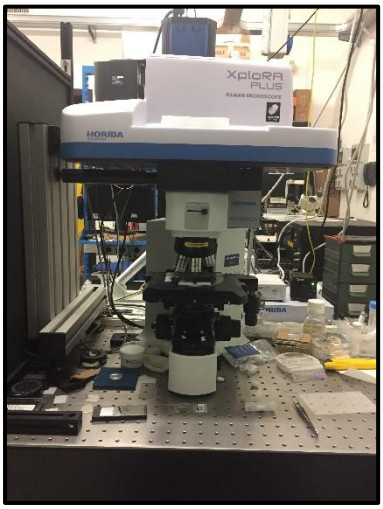


***Figure.II. 8.****The used Raman spectroscopy at CNR*

❖ **Principe:** An electromagnetic wave is sent on the sample that interacts with the molecules. As a result, the centers of gravity of the negative and positive charges do not coalesce anymore. Hence, a dipole moment appeared, which is proportional to the polarizability of the molecule, $\alpha$, and the amplitude of the induced electric field E with the following relation:

$$\boldsymbol{P=\alpha E}$$

Where polarizability is the ability of the electron cloud to deform under the action of an exterior field. In other words, an incident photon from a laser can absorb or emit a phonon of the crystal and then scatter into the surroundings in all directions. Thus, the photon gains (anti-stocks shift) or loss (stokes shift) energy, see Figure. II.8.

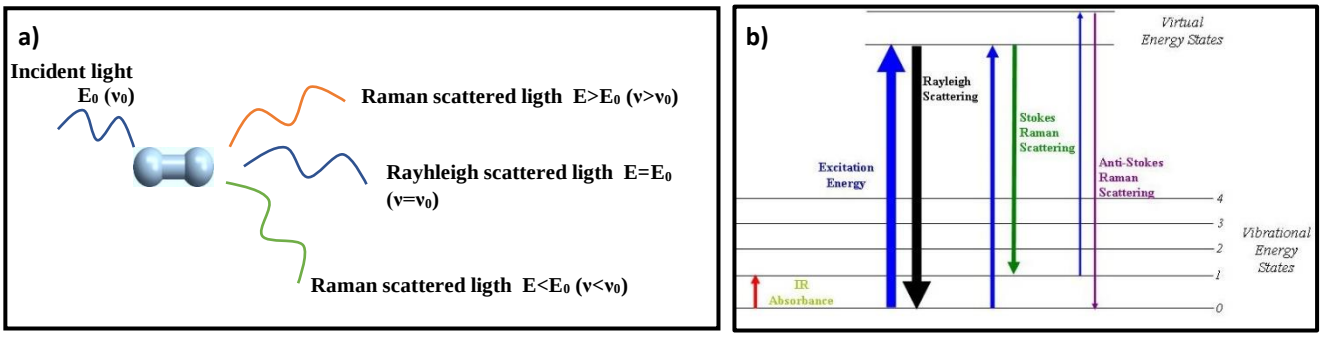


***Figure.II. 9.****(a) Raman scattering Principe, (b) scattering types*

## II.2. Optical spectroscopies

### II.2.a. Ultra-violet visible (UV-Vis) spectroscopy

❖ **Introduction:** Ultraviolet-visible (UV-Vis) spectroscopy is a quantitative and non-destructive technique see Figure II.9. The absorption spectrum is resulted from the interaction between ultra-violet (UV) or visible light [200nm; 900nm] with the matter. This tool characterizes the optical and electronic properties of various materials such as liquid, powder, and solids.

***Figure.II. 10.****The used UV-Vis spectroscopy at LabSensor*

❖ **Principe:** A light source (e.g. laser) interacts with the samples where its range is from 200nm to 900nm. Hence, a transition from a ground state to an excited state is occurring according to the wavelength and the nature of the specimen. This transition is resulted due to the energy absorption from the valence electron of the pattern.

### II.2.b. Photoluminescence (PL) technique

Photoluminescence (PL) spectroscopy is a nondestructive and contactless technique, see Figure.II.10. Vincenzo Cascariolo discovered photoluminescence in 1603 thanks to a bright stone [18].

When a monochromatic laser line interacts with the specimen's molecules, electrons are excited to higher energy level. Upon the excitation, the electrons return to the equilibrium level emitting photons (See Figure. II.11).

***Figure.II. 11.****The used PL spectroscopy at LabSensor*

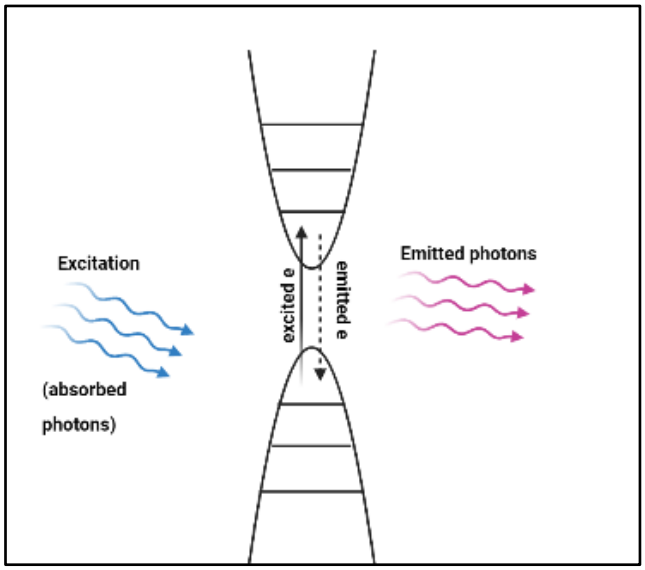


***Figure.II. 12.****Principe of photoluminescence*

## II.3. Morphological techniques

### II.3.a. Dynamic light scattering (DLS)

This tool is a powerful technique used to determine the size distribution and the size of particles in suspension or solution through the interaction of a laser with particles. The first three companies that have been launched the first DLS instrument in the market are Malven established in the United Kingdom (UK), ALV in Langen-Germany, and Brookhaven in Long Island-United state America (USA). The interaction of a monochromatic laser line

and the molecules of the solution sample results in the scattering of light randomly in all directions.

The used DLS setup in this investigation is presented in the following Figure.

***Figure.II. 13.****The used DLS spectroscopy at LabSensor*

### II.3.b. Scanning electrin microscopy(SEM)-enery dispersive X-ray (EDX) tool

As the name indicates, SEM-EDX is the scanning electron microscopy technique coupled with the energy-dispersive X-ray spectroscopy (EDX/EDS) tool. Using the SEM, we will obtain morphological information using an electron beam rather than a light beam, which is targeted to the specimen being examined to generate images. This later is combined with the elemental composition spectrum.

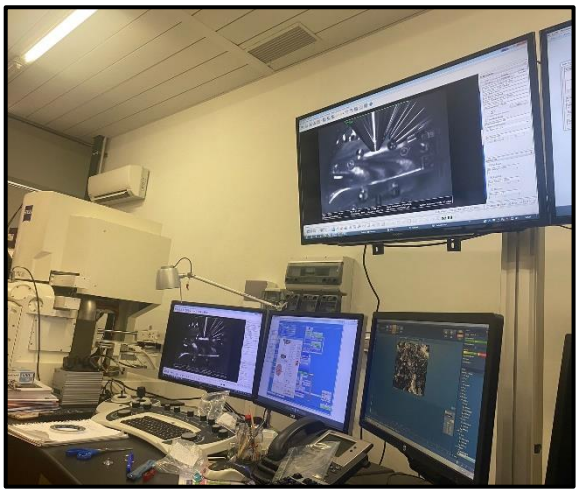

***Figure.II. 14.****The used SEM-EDX spectroscopy at LabSensor*

## II.4. Enhanced Raman spectroscopies (ERS)

Raman spectroscopy is a powerful technique for the detection of molecules and it has been used until now in various fields. Despite that, it has a major drawback, especially for the sensing attention, that the cross-section leads to difficulty in the detection of molecules in

low concentrations. Enhanced Raman scattering (ERS) has been shown up to overcome this limitation. Among them, we distinguished tip-enhanced Raman scattering (TERS), surface-enhanced Raman spectroscopy (SERS), surface-enhanced resonance Raman spectroscopy (SERRS), and lately photo-induced enhanced Raman spectroscopy (PIERS). The most known ERS tools are SERS and TERS.

### II.4.a. Surface-enhanced Raman spectroscopy (SERS)

❖ **Introduction:** As mentioned above, surface-enhanced Raman scattering (SERS) is the most popular and powerful technique for the detection, identification, quantification, and structural studies of small amounts of samples in materials research, surface science, and medical diagnostics…This developed Raman spectroscopy was discovered in the mid-1970s by Albrecht and Creighton and Jeanmaire and Van Duyne [14]. Gold, silver, and copper are the most commonly used as SERS substrates due to their surface plasmons existing in or close to the visible region [15]. The sample must be in a liquid or vapour form and placed in direct contact with the SERS substrate. This approach greatly enhances the Raman signal from sample molecules adsorbed on noble-metal surfaces processing nanoscale roughness.

❖ **Principle:** As Raman spectroscopy depends on the polarizability as well as the electric field, SERS uses interactions with specialized surfaces to enhance Raman signal strength. In other words, it is possible to increase either the $\boldsymbol{\alpha}$ or the **E** amplitude. The laser interacts with the SERS substrate, the excites surface plasmons that resonate with the vibrational transitions in the sample molecule adsorbed to that surface, see Scheme.II.3. In this work, the SERS substrate is composed of the layered TMDCs material, and the noble metal (Au, Ag) dropped on the top of 2D TMDCs. The chosen noble metal is gold because, firstly, of the existence of a plasmonic cloud that generates the Raman signals enhancement. Secondly, its neutrality, makes the SERS substrate the best candidate for the biological or chemical sensor.

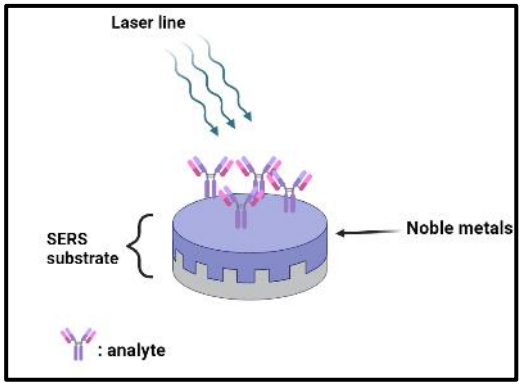


***Scheme.II. 3.****Scheme presenting the SERS mechanism*

### II.4.b. Photo-induced enhanced Raman spectroscopy (PIERS)

❖ **Introduction:** Photo-induced enhanced Raman spectroscopy (PIERS) is based on light-induced charge transfer (CT) between semiconductor and plasmonic metal surface (gold nanomaterials in our case) upon pre-UV irradiation. The out-performance of this technique is significant to that of non-photo spectroscopy.

❖ **Principle:** In the PIERS process, pre-UV irradiation is applied to the substrate (semiconductor-plasmonic metal) for additional chemical enhancement. Followed by laser line excitation on the substrate after dropping the probe molecule, as shown in the following scheme.

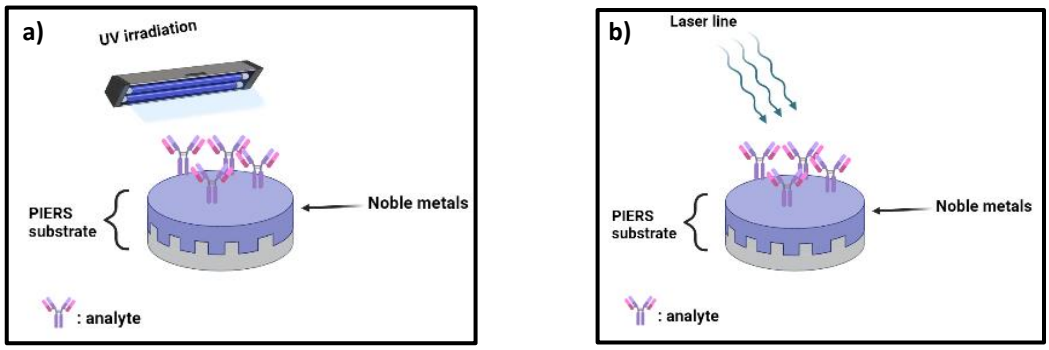


***Scheme.II. 4.****Scheme presenting PIERS mechanism: (a) pre-irradiation step, (b) after the irradiation*

## III. Plasmonic sensor

This type of sensor is used in this investigation for the detection of several analytes based on enhanced Raman spectroscopies (ERS) citing surface-enhanced Raman spectroscopy (SERS) and photo-induced enhanced Raman spectroscopy (PIERS), Figure II.15.For the detection procedure, we will use ERS substrate based on 2D-$MX_2$ nanosheets coated with 2D-Au with different shapes.

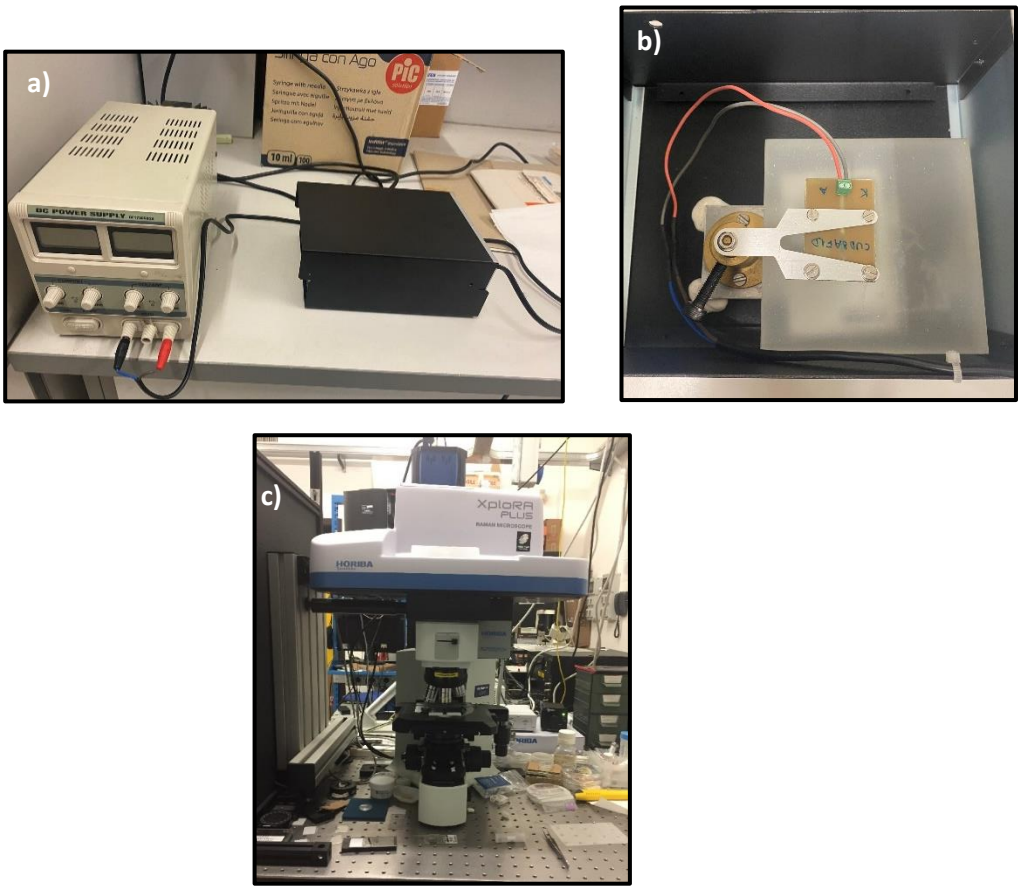


***Figure.II. 15.****The used (a) PIERS setup, (b) irradiation source, and (c) SERS technique at CNR*

## IV. Electrochemical sensor

The device used in this work is the screen-printed carbon electrode (SPCE). Herein, the determination of the probe molecule is achieved through the redox reaction upon the application of appropriate potential with the help of DropSens µStat 400 Potentiostat (Figure.II.16) . From the obtained curves, various information can be calculated citing the sensitivity (S), active surface area (A), the limit of detection (LoD), the limit of quantification (LoQ)…


***Figure.II. 16.****DropSens µStat 400 Potentiostat system at LabSensor for the electrochemical test*

Several analytical techniques are used according to the literature where the most familiar ones are cyclic voltammetric (CV), differential pulse voltammetry (DPV), linear sweep voltammetry (LSV), and square wave voltammetry (SWV) [16], see Figure.II.17.

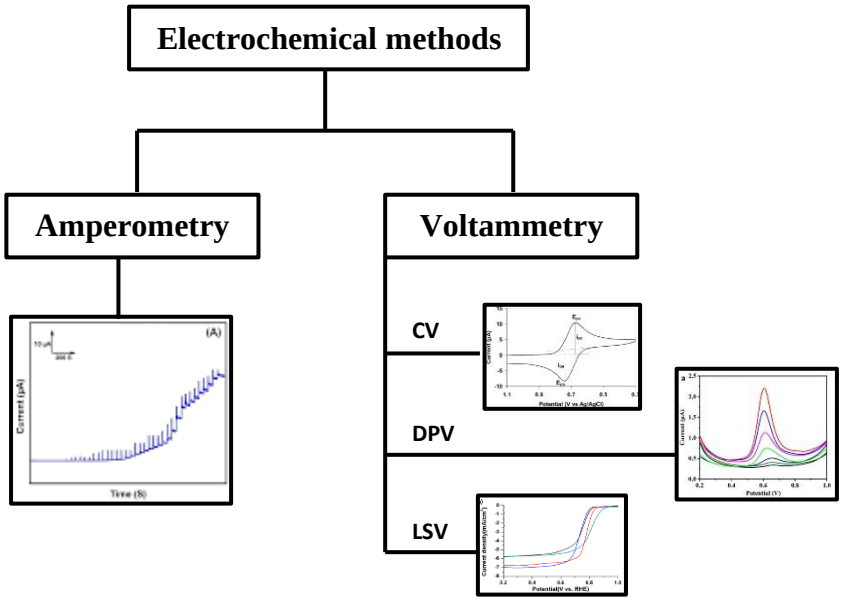


***Figure.II. 17.****Familiar Analytical methods*

Electrochemical impedance spectroscopy (EIS) is acquired to determine the equivalent circuit of the electrode surface from the Nyquist plot, the conductivity and resistivity features of the sensing layer, and to further understand the charge transfer (CT) mechanism occurring between working electrode-electrolyte (WE-electrolyte) or working electrode-analyte (WE-analyte). All these data occurred through the Autolab PGSTAT204 system in the $[FeCN_6]^{3-/4-}$ solution, see Figure.II.18.

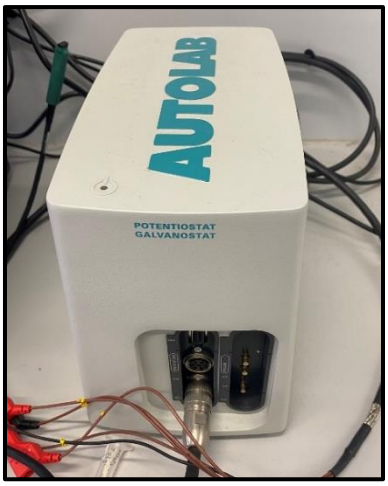


***Figure.II. 18.****Autolab PGSTAT204 system used for EIS study at LabSensor*

## V. Probe molecules: Medical and environmental analytes

In this investigation, we target various fields denoting medicine, environment, and food quality control using plasmonic and electrochemical sensors.

### V.1. 4-mercaptobenzoic acid (MBA): Raman reporter molecule

The 4-mercaptobenzoic acid, abbreviated as MBA, is a chemical substance with $C_7H_6O_2S$ as a chemical formula and its structure is shown in the figure below. This molecule is used as a Raman reporter molecule to check at first place the efficiency of our ERS substrates.

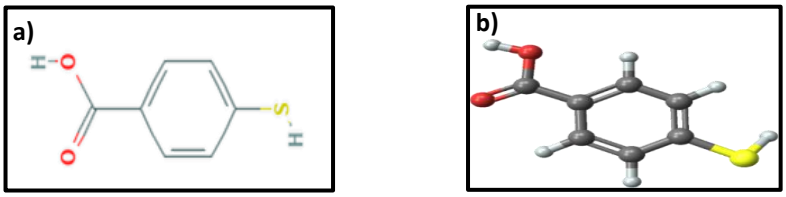


***Figure.II. 19.****(a) MBA chemical structure (b) MBA 3D conformer*

### VI.2.Medical analytes

#### V.2.a. Folic Acid (FA)

Folic acid (FA), known as vitamin $B_9$, belongs to the B vitamins family and it is important for human health, see Figure.II.20. This vitamin is necessary for cell growth such as blood cell production, repair, and synthesis of DNA. However, it is difficult to get it into the human diet. Thus, the deficiency of this vitamin can cause numerous diseases for human beings and pregnant women.

The lack of blood cells leads to a less rate of oxygen in the organs and tissues. Moreover, FA anemia causes megaloblastic which is the change in the red blood cells' shape from round to oval. During pregnancy, the deficit of vitamin $B_9$ results in neural tube irregularities citing spina bifida, anencephaly...

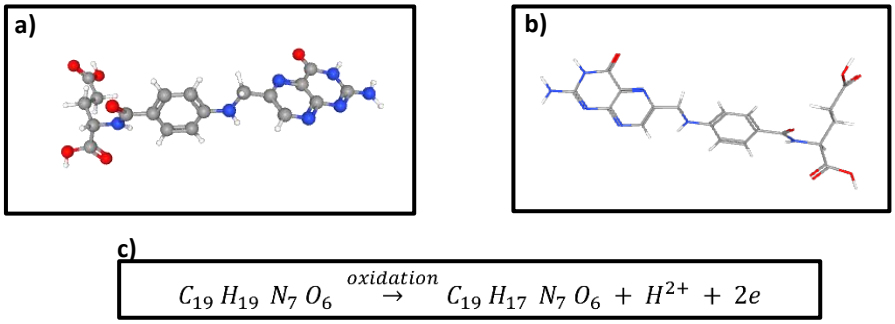


***Figure.II. 20.****a) 3D conformer and b) molecular structure of FA; c) oxidation reaction of FA*

### V.2.b. Dopamine (DA)

Dopamine (DA) is a neurotransmitter in the human body (Figure. II.21) that controls various physiological functions of the central nervous system denoting learning, drug addiction, and movement [17]...

Different diseases can result from a disorder of DA in the human body denoting Parkinson's, schizophrenia, and attention deficit [17]. Moreover, abuse of DA can lead to depression and drug dependence [18]. Thus, a highly selective and efficient biosensor is needed in clinical use since the electrochemical performance of DA is a key role in this kind of diagnosis [17].

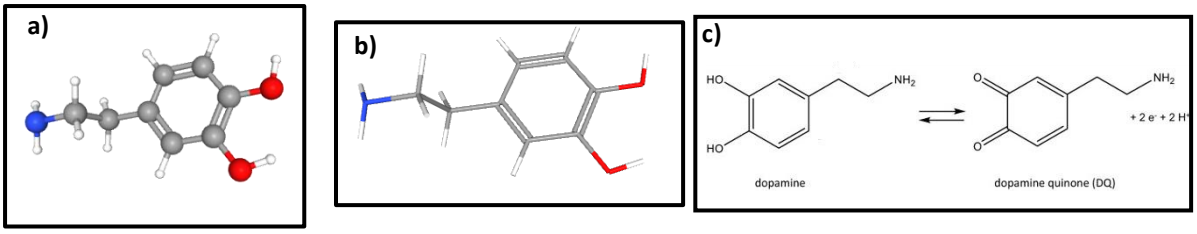


***Figure.II. 21.****a) 3D conformer and b) molecular structure of DA; c) oxidation reaction equation of DA*

## V.3. Environmental analytes

Food and water control become a challenging research area since pollutant determination at the trace level is required. In fact, pesticides are widely used in producing food; they include herbicides, insecticides, and fungicides. Given to the extraordinary rise of industrial growth, the chemical additive products in food are improved. The abusive use of these compounds results in either the destruction or reduction of food [19]. Thus, their detection is

needed, due to their hazard to human and animal health citing infertility, carcinogenicity, respiratory problems, and neurological diseases [19,3]. Therefore, the early detection of these chemicals in food is significant.

### V.3.a.Fungicides: Thiram

Fungicides (Thiram, Maneb, Mancozeb,…) quantification is nowadays strongly needed to monitor different fungal diseases in plants. Further, to avoid toxicity issues in humans associated with the use of fungicides in agriculture, the maximum residual limit in food imposed by the European Union (EU) is settled from 0.41 to 41.6 µM[20].

Among sulfur derivatives, thiram is the second most used fungicide in agriculture [21], see Figure. II.22. It is a toxic high-chemical and biologically active molecule due to its ability to chelate polyvalent cations[21]. Because of its strong affinity with soil particles and low solubility in water, it is challenging to eliminate Thiram from the natural environment.[22]

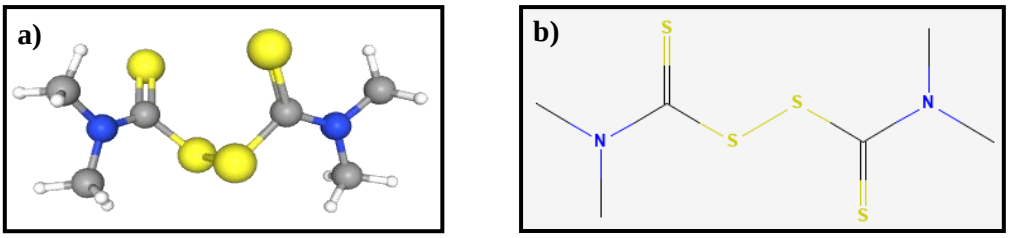


***Figure.II. 22.****Thiram (a) 3D conformer and (b) chemical structure*

# References


1. Geim, A. K. & Novoselov, K. S. THE RISE OF GRAPHENE. 14.

2. Abid, K. *et al.* Photoinduced Enhanced Raman Spectroscopy with Hybrid Au@WS2 Nanosheets. *J. Phys. Chem. C* **124**, 20350–20358 (2020).

3. Electronics and optoelectronics of two-dimensional transition metal dichalcogenides | Nature Nanotechnology. https://www.nature.com/articles/nnano.2012.193.

4. Backes, C. *et al.* Production of Highly Monolayer Enriched Dispersions of Liquid-Exfoliated Nanosheets by Liquid Cascade Centrifugation. *ACS Nano* **10**, 1589–1601 (2016).

5. Bonaccorso, F., Bartolotta, A., Coleman, J. N. & Backes, C. 2D-Crystal-Based Functional Inks. *Advanced Materials* **28**, 6136–6166 (2016).

6. Herizchi, R., Abbasi, E., Milani, M. & Akbarzadeh, A. Current methods for synthesis of gold nanoparticles. *Artificial Cells, Nanomedicine, and Biotechnology* **44**, 596–602 (2016).

7. A study of the nucleation and growth processes in the synthesis of colloidal gold - Discussions of the Faraday Society (RSC Publishing). https://pubs.rsc.org/en/content/articlelanding/1951/df/df9511100055.

8. Controlled Nucleation for the Regulation of the Particle Size in Monodisperse Gold Suspensions | Nature Physical Science. https://www.nature.com/articles/physci241020a0.

9. Kimling, J. *et al.* Turkevich Method for Gold Nanoparticle Synthesis Revisited. *J. Phys. Chem. B* **110**, 15700–15707 (2006).

10. Haiss, W., Thanh, N. T. K., Aveyard, J. & Fernig, D. G. Determination of Size and Concentration of Gold Nanoparticles from UV−Vis Spectra. *Anal. Chem.* **79**, 4215–4221 (2007).

11. Philip, D. Honey mediated green synthesis of gold nanoparticles. *Spectrochimica Acta Part A: Molecular and Biomolecular Spectroscopy* **73**, 650–653 (2009).

12. Najibi, A., Kamran, S., Baezzat, M. R. & Heidari, R. Evaluating graphene oxide and gold nanocomposites (GO@AuNPs) as adsorbents for preconcentration of tetramethyl thiuram disulfide(thiram) from natural waters and as thiram antidotes for in vivo application. *International Journal of Environmental Analytical Chemistry* **101**, 794–809 (2021).

13. Dong, J., Carpinone, P. L., Pyrgiotakis, G., Demokritou, P. & Moudgil, B. M. Synthesis of Precision Gold Nanoparticles Using Turkevich Method. *Kona* **37**, 224–232 (2020).

14. Willets, K. & Mayer, K. Surface-enhanced Raman scattering (SERS) as a characterization method for metal-organic interactions. in *Handbook of Organic Materials for Electronic and Photonic Devices* 529–549 (Elsevier, 2019). doi:10.1016/B978-0-08-102284-9.00016-4.

15. Smith, W. E. & Rodger, C. Surface-Enhanced Raman Scattering (SERS), Applications*. in *Encyclopedia of Spectroscopy and Spectrometry* 2822–2827 (Elsevier, 1999). doi:10.1016/B978-0-12-374413-5.00304-3.

16. Curulli, A. Electrochemical Biosensors in Food Safety: Challenges and Perspectives. *Molecules* **26**, 2940 (2021).

17. Mohammad-Shiri, H., Ghaemi, M., Riahi, S. & Akbari-Sehat, A. Computational and Electrochemical Studies on the Redox Reaction of Dopamine in Aqueous Solution. *International journal of electrochemical science* **6**, 317–336 (2011).

18. Klein, M. O. *et al.* Dopamine: Functions, Signaling, and Association with Neurological Diseases. *Cell Mol Neurobiol* **39**, 31–59 (2019).

19. Electrochemical Sensors for Food Safety | IntechOpen. https://www.intechopen.com/chapters/64766.

20. Ibáñez, D., Izquierdo-Bote, D., González-García, M. B., Hernández-Santos, D. & Fanjul-Bolado, P. Development of a New Screen-Printed Transducer for the Electrochemical Detection of Thiram. *Chemosensors* **9**, 303 (2021).

21. Steter, J. R., Kossuga, M. H. & Motheo, A. J. Mechanistic proposal for the electrochemical and sonoelectrochemical oxidation of thiram on a boron-doped diamond anode. *Ultrasonics Sonochemistry* **28**, 21–30 (2016).

22. Nováková, K., Navrátil, T., Dytrtová, J. J. & Chýlková, J. The use of copper solid amalgam electrodes for determination of the pesticide thiram. *J Solid State Electrochem* **17**, 1517–1528 (2013).

# Results & Discussion

# Results & Discussion

## Electrochemical Sensors

# Chapter III

## Results & Discussion: Electrochemical Sensors

### Table of Contents

# Chapter III

## Results & Discussion: Electrochemical Sensors

### Table of Figures

# Chapter III

## Results & Discussion: Electrochemical Sensors

### Table of Tables

# Chapter III

## Results & Discussion: Electrochemical Sensors

### Acronyms and Abbreviations

All the abbreviations used in this chapter are listed below:

- 2D: Two-dimensional
- $MoS_2$: Molybdenum disulphide
- UV: Ultra-violet
- <N>: average number of layers
- SEM: Scanning electron microscope
- EDX: Energy dispersive spectroscopy
- SPCE: Screen printed carbon electrode
- Au@MoS2: Gold nanoparticle-molybdenum disulphide
- D: Diffusion coefficient
- $I_{pa}$: Anodic peak current
- $R_{CT}$: Charge transfer resistance
- $R_s$: Electrolyte resistance
- $Z_w$: Warburg impedance
- $C_{dl}$: Double layer capacitance
- PBS: Phosphate buffer solution
- CV: Cyclic voltammetry
- WE: Working electrode
- AuNPs: Gold nanoparticle
- LSV: Linear sweep voltammetry
- FT-IR: Fourier transform infrared spectroscopy
- WS2: Tungsten disulphide
- GO: G raphene oxide
- GO-WS2: Graphene oxide- tugsten disulphide
- NS: Nanosheets
- PL: Photoluminescence
- EIS: Electrochemical impedance spectroscopy
- DPV: Differential potential voltammetry

- Ei and Ef: Initial and final energy
- DLS: Dynamic light scattering
- BZ: Brouillon zone
- $MoSe_2$: Molybdenum selenide
- DA: Dopamine

# Overview

In this section, we will start with the findings obtained with the electrochemical sensing layers. First, we will present the basic characterizations that occurred on the samples and the sensing layers. Then, we will present the different electrochemical and electroanalytical tests performed on the different modified SPCE toward various analytes.

## I. Molybdenum disulphide ($MoS_2$)

The obtained nanosheets were characterized by using several techniques and then used for the in situ determination of vitamin B9.

### I.1. UV-Vis spectroscopy

The exfoliated $MoS_2$ nanosheets were characterized with UV-Vis spectroscopy after their dilution at 1:10 (V/V) where the obtained spectrum is presented in Figure.III.1. Four prominent excitonic bands were observed. An excitonic transition with E = 0.19eV results in the appearance of A and B located at ~676nm and ~613nm, respectively [1,2]. Moreover, the C (at 467nm) and D ( at 382nm) excitonic bands were observed that are derived from the direct excitonic transition from VB to CB[3].

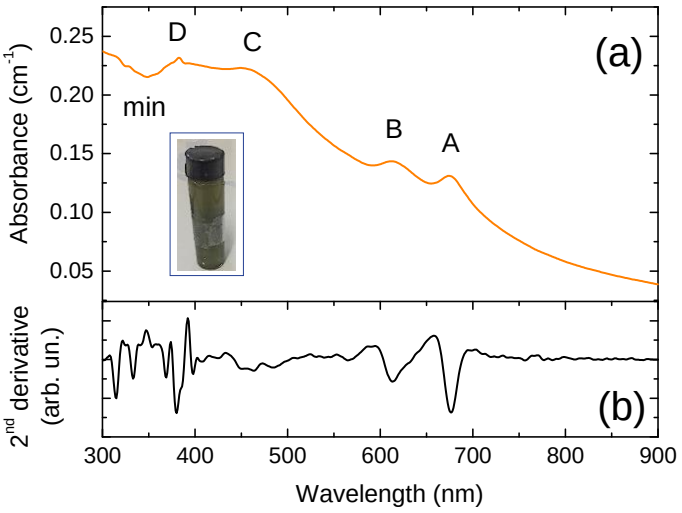


***Figure.III.1.****(a) Extinction spectrum of the 2D-MoS2 dispersion (diluted 1:10 v/v). (b) Second derivative of the extinction signal. Inset: Picture of the MoS2 nanosheets suspension (non-diluted solution).*

From the UV data, we can compute several characteristics parameters for $MoS_2$ nanosheets denoting their concentration, average length, and the number of layers (N). These parameters were determined using the following empirical formulas [4]:

$$\langle L \rangle\ (\mu m) = \frac{3.5 * Ext_B/Ext_{350} - 0.14}{11.5 - Ext_B/Ext_{350}} \qquad eq\ (1)$$

$$C = \frac{1}{l} Ext350/\varepsilon_{350} = -\frac{1}{\varepsilon_{350}\, l}\, Log_{10} T(\lambda = 350\ nm) \qquad eq(2)$$

$$\langle N \rangle = 2.3 * 10^{36}\, e^{-54888/\lambda_A} \qquad eq\ (3)$$

Based on the intensity of the local minimum extinction at 350nm ($Ext_{350}$) and the intensity of B-band ($Ext_B$), in equation (1), we have determined that the average length $\langle L \rangle$ is equal to ~ 200 nm. The concentration of these dispersions is found to be 32 µg/mL calculated with equation (2) with $\varepsilon_{350}$ is the absorption coefficient equal to 69 $Lg^{-1}cm^{-14}$. The cuvette length ($l$) is 1cm and $T_{\lambda 350}$ is the transmittance at the local minimum. The average number of layers $\langle N \rangle$ is found to be ~12 that is calculated from equation (3) based on the wavelength of A-band.

## I.2. Raman discussion

At room temperature and using a 514.5nm laser line, we collected the Raman spectrum of $MoS_2$ nanosheets (Figure.III.2). Two prominent Raman modes are located at 385nm and 410nm identifying the vibration of S-M atom in-plane ($E^1_{2g}$) and the vibration of S atoms out-of-plane ($A_{1g}$) modes[5]. Based on the difference between these two vibrational modes $\Delta\omega(E^1_{2g}\text{-}A_{1g})$, we can determine the number of layers [6]. As cited by Sahoo, D. et al., the $\Delta\omega$ decrease from $26cm^{-1}$ to $17.5cm^{-1}$ when decreasing the number of layers i.e. from bulk to single layer [7]. In our case, the $E^1_{2g}\text{-}A_{1g}$ frequency difference is found to be $25cm^{-1}$ indicating that we have more than 6 layers that are in agreement with the previous investigation [8]. Moreover, this difference and the number of layers N are related by the following mathematical equation :

$$\Delta\omega\ (A_{1g} - E^1_{2g}) = 25.8 - 8.4/N \qquad eq\ (4)$$

Based on the equation above, the N of $MoS_2$ is equal to 10 [9,10].

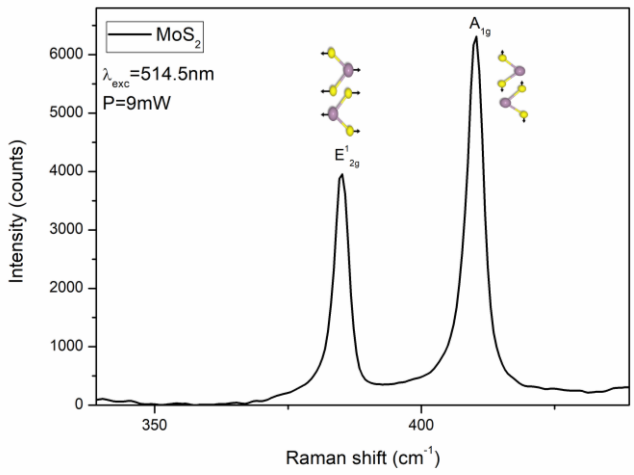


***Figure.III. 2.****Raman spectrum of MoS2 at room temperature under 514.5 nm laser line. Inset: atomic displacement of active (E12g, A1g).*

## I.3.Scanning electron microscopy-energy dispersive X-ray discussion

One of the important characterizations is scanning electron microscopy (SEM) coupled with energy dispersive X-ray (EDX) spectroscopy that is occurred to study the morphology of $MoS_2$ onto the screen-printed carbon electrode (SPCE). The outcomes of this characterization are shown in Figure.III.3. The morphology of unmodified and modified 2D-$MoS_2$ SPCE is presented in Figure III.3.a-b. The modified Au@$MoS_2$ electrode was also characterized. Figure III.3.c shows the morphology of this modified SPCE at low magnification showing that the electrode is covered by the modified $MoS_2$ SPCE and forming aggregates with size ranges from 80nm to 200nm as depicted in Figure. III.3.d (at high magnification). The EDX spectrum proves the presence of the predicted elements as shown in Figure III.3.e where the wt% is 71, 24, 4, and 0.3 for Au, C, Mo, and S elements, respectively. It is shown in this spectrum the presence of Cl element that can be introduced to contamination by $HAuCl_4$ used in the preparation of Au-$MoS_2$.

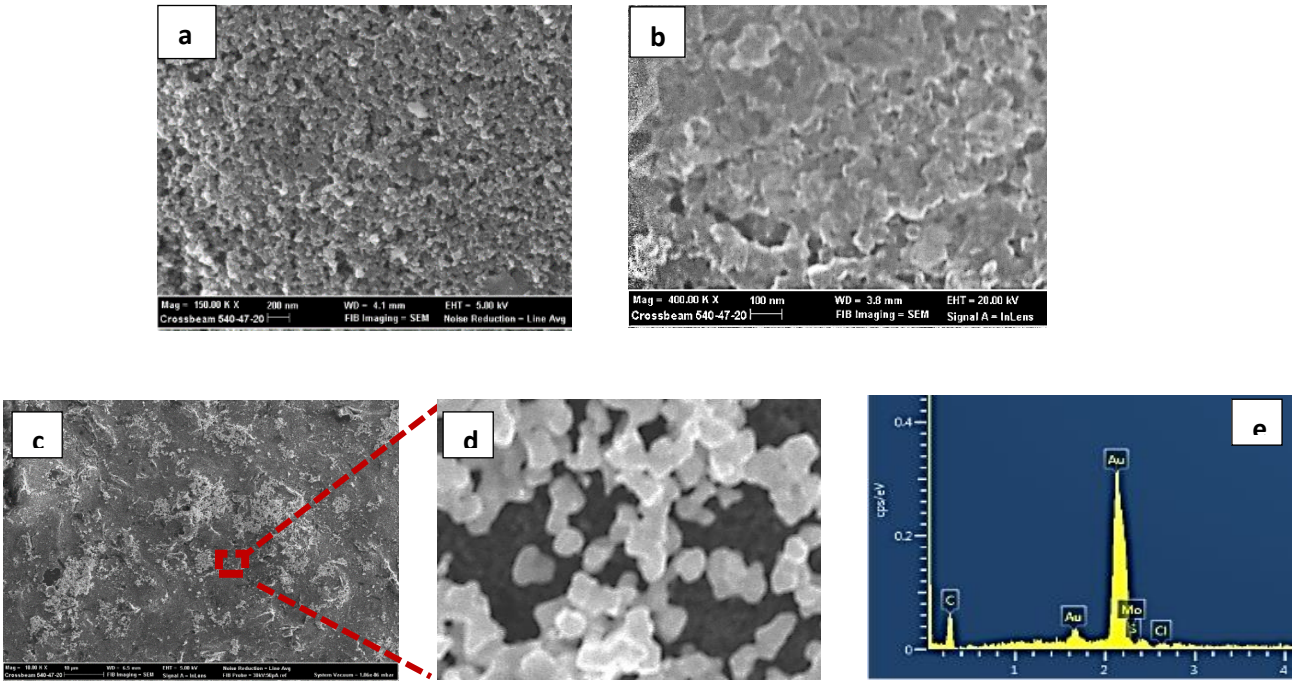


***Figure.III. 3.****SEM images showing the morphology of: a) bare SPCE; b) 2D-MoS2 nanosheets over SPCE surface, c, d) SEM image at different magnification of the AuNPs-MoS2/SPCE surface; e) EDX spectrum.*

## I.4.Electrochemical study of Au-$MoS_2$/SPCE

Before the electroanalytical study of the modified electrodes, we should study their electrochemical behaviour. To achieve that, we performed the CV test in ferrocyanide solution $[Fe(CN)_6]^{3-/4}$ at [-0.2V, -0.6V] potential range and at 0.05V/s scan rate. Compared with the bare SPCE, a slight improvement in the current response, see Figure. III.4.However, Au-$MoS_2$/SPCE illustrates better performance toward the determination of the redox $[Fe(CN)_6]^{3-/4-}$ compared to unmodified and $MoS_2$ SPCE due to the higher surface area.

The active surface area (A) is computed using equation (5) where the anodic peak current is $I_{pa}$ (expressed in µA), the diffusion coefficient 'D' is expressed in $cm^2s^{-1}$, ν is the used scan rate, n is the number of electrons involved in the oxidation reaction, and C is the concentration in mol $cm^{-3}$ [11]. Owing to this equation, we conclude that A of AuNPs-$MoS_2$/SPCE increased by 12% compared to that of the bare.

$$I_{pa} = 2.69 \times 10^5 SAD^{1/2} n^{3/2} \nu^{1/2} C \quad eq\ (5)$$

In the ferrocyanide solution, we performed electrochemical impedance spectroscopy (EIS) test to further study the electrochemical response, and the Nyquist plot of the electrodes is depicted in Figure.III.5 For unmodified electrodes, we obtained semicircle and linear segments in high and low frequencies, respectively. The equivalent circuit is illustrated in Figure.III.5.b with Randles parameters $R_{CT}$, $R_s$, Zw, and Cdl identifying charge transfer (CT) resistance, electrolyte resistance, Warburg impedance, and double-layer capacitance, respectively. A change in $R_{CT}$ may be assigned to a modification of the CT rate across the interface. In this framework, a crucial change in the CT resistance from ~3707Ω to 19.6KΩ and 19.3KΩ for bare, $MoS_2$/SPCE, and Au@$MoS_2$/SPCE, respectively.

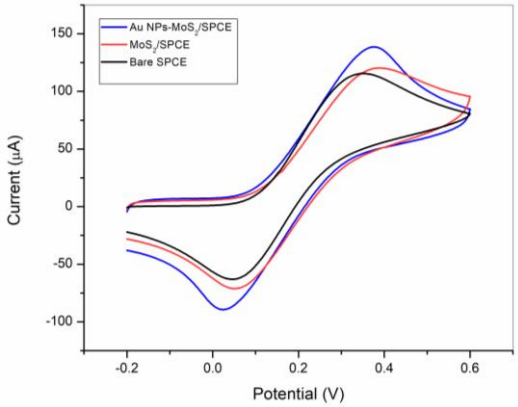


***Figure.III. 4.****CV in [Fe(CN)6]3−/4− solution for the SPCE, MoS2/SPCE and AuNPs MoS2/SPCE.*

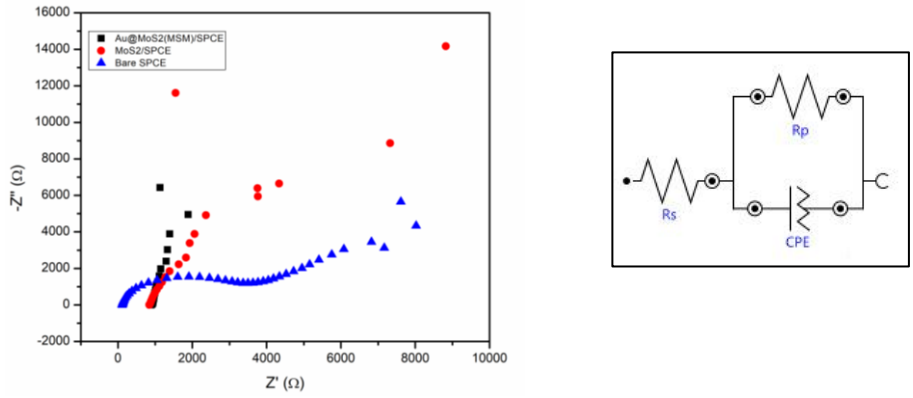


***Figure.III. 5.****(a) Nyquist plot of bare SPCE, MoS2/SPCE and Au NPs-MoS2/SPCE. (b) equivalent circuit*

## I.5.Folic acid (FA) determination using Au-$MoS_2$/SPCE

In 0.01M of phosphate buffer solution (PBS) with pH=7.4, FA determination occurred with unmodified and modified ($MoS_2$, Au-$MoS_2$) SPCE at 50mV/s scan rate and in [0V;1V] potential range as shown in Figure.III.6.a. No faradic peak is observed with unmodified SPCE and $MoS_2$/SPCE where the CV of the prior electrode is larger because of the higher

capacitive effect of the sensing layer. Yet, with Au@$MoS_2$/SPCE, we observed a couple of anodic and cathodic peaks dominate the CV curve located at 0.27V and 0.85V, respectively. These peaks are identified in the redox cycle of Au indicating the formation of AuNPs on the working electrode (WE).

Figure.III.6.b presents the electroanalytical method, Linear Sweep Voltammetry (LSV), chosen for the detection of vitamin B9 in PBS containing different concentration values. At 0.6V, we observed a weak oxidation peak that shifted to lower potential (0.52V) and higher current intensity with $MoS_2$/SPCE (inset Figure.III.6.b) indicating that $MoS_2$ is good electrocatalytic than bare SPCE for the determination of FA.

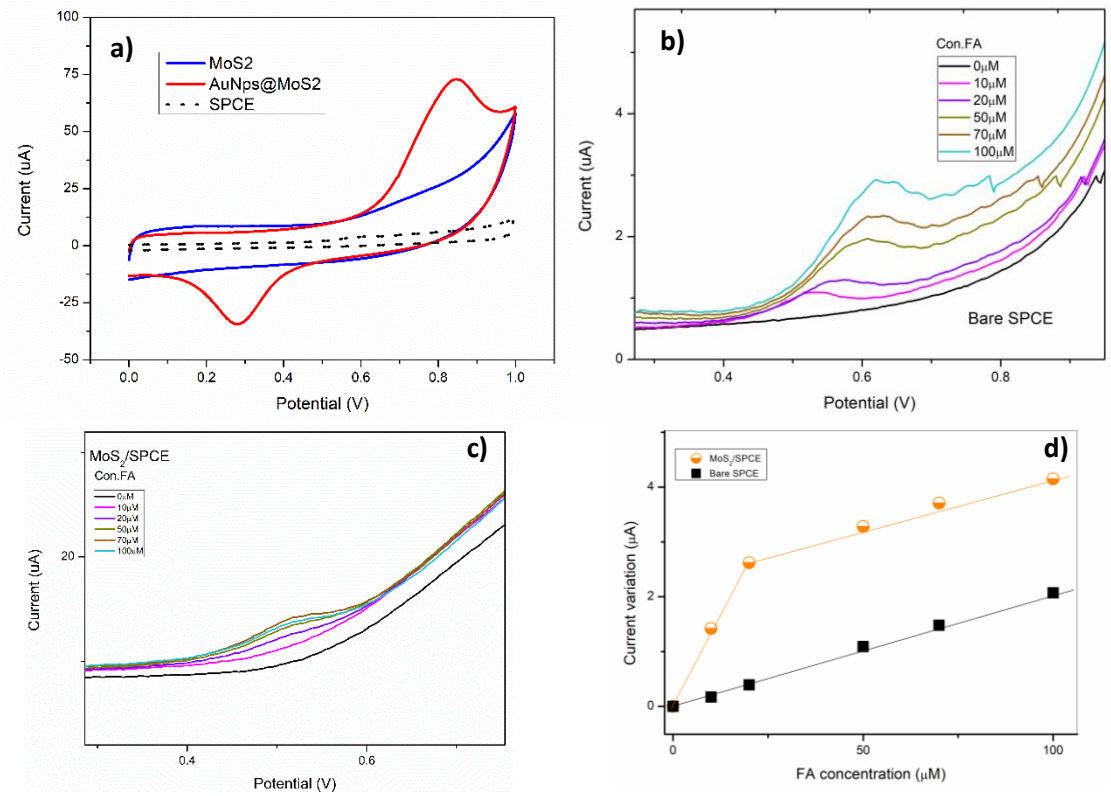


***Figure.III. 6.****(a)CV of bare SPCE, MoS2/SPCE, and Au NPs MoS2/SPCE in PBS solution at 50 mVs-1, b) LSV measurement of bare/SPCE, c) MoS2/SPCE and c) calibration curve of FA on the bare SPCE and MoS2/SPCE*

At a different concentration of FA ranging from 0µM to 100µM, we performed an electroanalytical test on Au@$MoS_2$/SPCE where we observed a significant decrease in the current peak of $Au_{ox}/Au_{red}$ when increasing FA concentration, see Figure III.7.a. This modified electrode illustrates a larger variation in signals compared to the other studied electrodes, see Figure III.7.a. Regarding the sensitivity, it was computed in two linear

regimes. In the first one [0 µM, 20 µM], the sensitivity is equal to ~21 which is ~5 times higher than that in [20 µM, 100 µM], see Figure III.7.b.

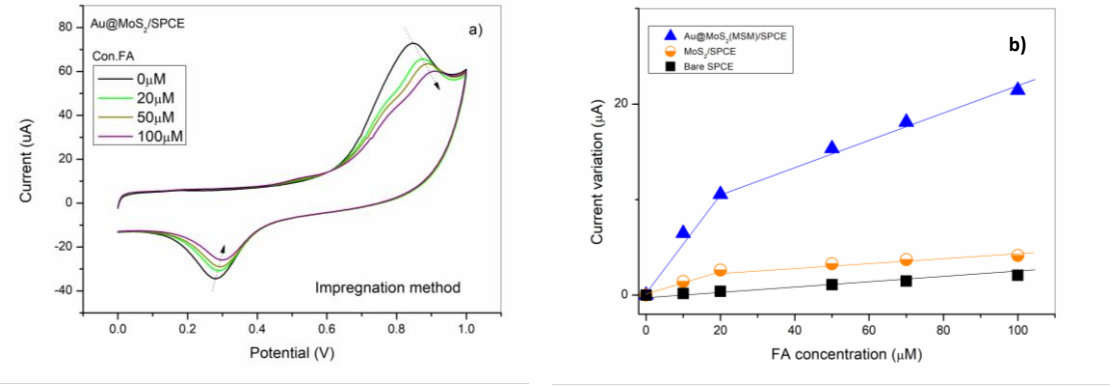


***Figure.III. 7.****(a) CV measurement of FA on AuNPs-MoS2/SPCE; (b) Calibration curve of AuNPs-MoS2/SPCE. Calibration curve of FA on SPCE and MoS2/SPCE are also shown for comparison*

## I.6. Sensing mechanism

The sensing mechanism beyond FA determination on $MoS_2$/SPCE and Au-$MoS_2$/SPCE is different which can be explained by the interaction of this analyte with the sensing layer in the presence and the absence of AuNPs. Indeed, on $MoS_2$/SPCE, the sensing layer behaves as an active surface to electrooxidizes FA as shown in Scheme III.1.a. Nevertheless, the suggested sensing mechanism for $MoS_2$/SPCE does not operate with Au-$MoS_2$/SPCE where the surface is covered by the FA molecules that adsorbed strongly on AuNPs surface as shown in Scheme.III.1.b. The strong adsorption poisons the sensing layers preventing the electrooxidation of vitamin B9. Using SERS, Raman analysis, and DFT calculations, Castillo's group proved that the interaction between gold and FA occurred through nitrogen in the pterin part (circled in red) [12]. In addition to that, these molecules can be adsorbed on the AuNPs surface by the carboxylic group.

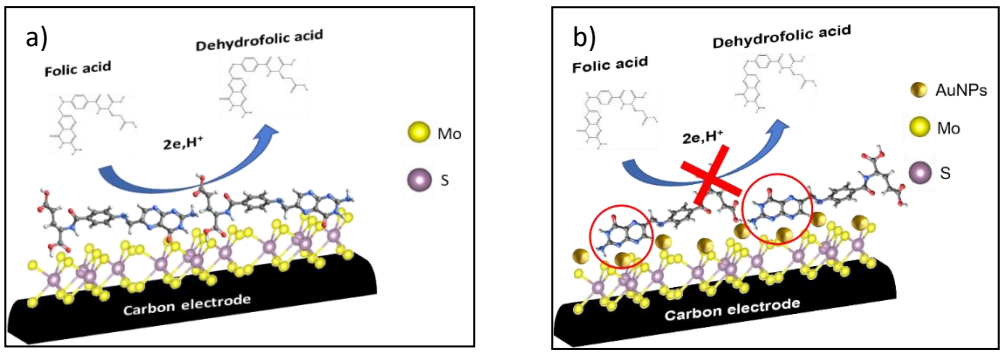


***Scheme.III. 1.****Schematic representation of adsorption/reaction processes which occur in the presence of FA on the surface of: a) MoS2/SPCE and b) Au NPs-MoS2/SPCE.*

In Majidi et al work, they suggested that the interaction between AuNPs surface and vitamin B9 is achievable through the glutamic acid moiety especially its carboxylate group and the amin group of pterin portion [13].

Since the binding affinity between FA and the AuNPs, the active sites' number decreases in the Au surface leading to the current reduction observed with the LSV test. A comparable sensing mechanism is reported on AuNPs-$TiO_2$ nanotubes for the determination of GSH (glutathione) [14].

## I.7. Fourier transform infrared (FTIR) study

Fourier transform infrared (FTIR) test was recorded on AuNPs-$MoS_2$/SPCE to further study the interaction between FA-AuNPs. Figure III.10 illustrates the FTIR spectra of unmodified and modified electrodes in addition to that of the FA powder. This prior presents the prominent absorption peaks at 1694$cm^{-1}$ identified to C=O stretching, 1607$cm^{-1}$, and 1475$cm^{-1}$ corresponding to pterin and phenyl rings. On both the bare electrode and $MoS_2$/SPCE, the vitamin B9 signature is hardly visible, which is not the case with Au-$MoS_2$/SPCE as shown in Figure III.8. This result suggests that B9 molecules interact with AuNPs on the surface of the modified electrode that may be introduced in the spectrum with the absence of the skeletal vibration of pterin ring (at 1508$cm^{-1}$).

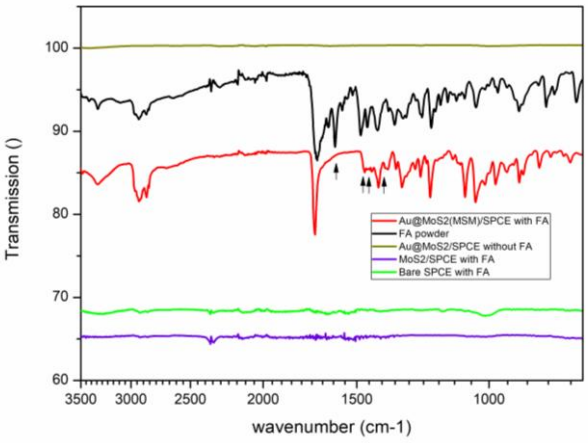


***Figure.III. 8.****FT-IR spectra acquired from FA deposited from a solution 10-4 M on the investigated electrodes*

# II. Graphene-Tungsten disulphide (GO:$WS_2$) nanocomposite

## II.1. Scanning electron microscopy-energy dispersive X-ray study

The morphology of the modified and bare SPCE electrodes is studied with the SEM-EDX technique where their outcomes are depicted in Figure III.9. From these findings, we noted

that the morphology of the working electrode of SPCE is modified compared with GO/SPCE and bare SPCE that is proved also by EDX spectrum where the expected elements are detected.

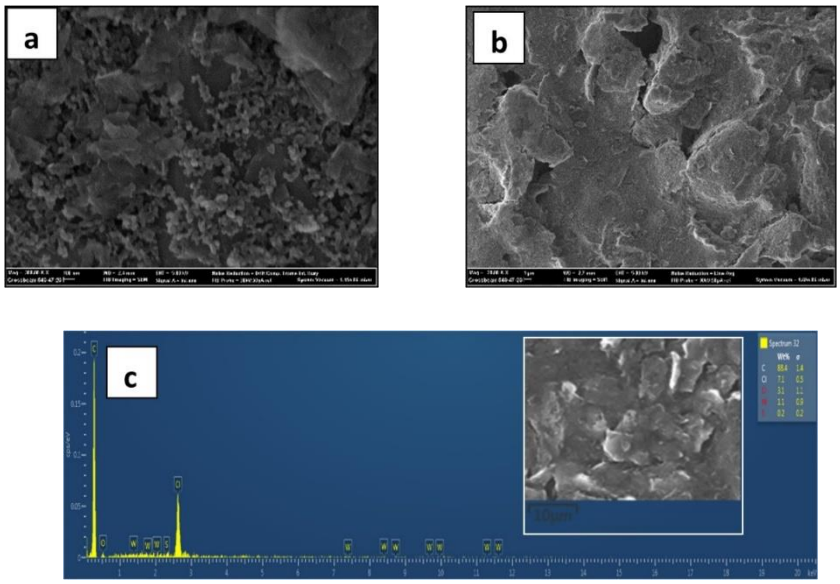


***Figure.III. 9.****SEM images of (a) GO/SPCE, (b) GO@WS2(1:1)/SPCE, and (c) EDX spectrum of GO@WS2(1:1)/SPCE.*

## II.2. Raman discussion

The nanocomposite GO@$WS_2$, $WS_2$ nanosheets, and pure GO powder were characterized with Raman spectroscopy to verify their characteristic vibrational modes, see Figure III.10. All spectra were recorded at room temperature and under a 514.5nm laser line.

Raman spectrum of the exfoliated $WS_2$ nanosheets (NS) dropped in silicon slide is presented in Figure III.10.a. The two significant modes were obtained in the Raman spectrum located at 351$cm^{-1}$ and 416$cm^{-1}$ standing for the W-S in-plan vibration ($E^1_{2g}$) and the S atom out-of-plan vibration ($A_{1g}$), respectively.

Three characteristic peaks of GO were observed; D-band (at 1370$cm^{-1}$) indicating the defect mode, G-band located at 1590$cm^{-1}$ standing for graphite mode, and the secondary D-band, named also G' or 2D band, obtained at 2700$cm^{-1}$ identifying the ordered $sp^2$ hybridized carbon network [15], [16].

Following the literature, the ratio value of D and G bands intensities is used as an indicator of graphene and its analogs' order degree in the crystal structure [17]. Indeed, the higher disorder in these 2D materials is related to the higher broadness and intensity of the D and G bands, respectively. According to Qiao et al. group, the higher graphitization degree is

observed when the intensity ratio of the D and G band ($I_D/I_G$) decreases [18]. In this framework, the $I_D/I_G$ ratio value of pure GO is 0.6 showing the good order in its crystal structure. For the GO@$WS_2$ nanocomposite, this ratio is equal to 0.74, 0.5, and 0.44 for 1:2, 1:1, and 2:1 GO: $WS_2$ ratios, respectively.

At these experiment conditions, we could not observe any characteristic vibration Raman mode of $WS_2$ NS after the deposition onto the working surface of SPCE. This is maybe introduced to the porous surface of the electrode resulting in the suppression of $WS_2$ vibrational modes.

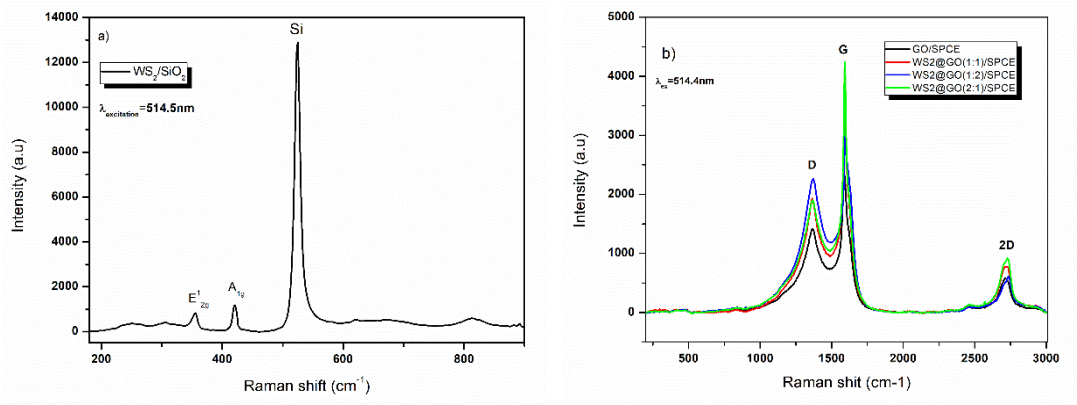


***Figure.III. 10.****(a) Raman spectrum of WS2 dropped on SiO2 substrate (b) Raman spectrum of GO/SPCE(black line), GO@WS2 (1:1)/SPCE (red line) , GO@WS2 (1:2)/SPCE (blue line), and GO@WS2 (2:1)/SPCE (green line).*

## II.3. Photoluminescence (PL) study

At ambient conditions and under 350nm excitation wavelength, the optical features of the nanocomposite GO@$WS_2$ at different ratios and the starting 2D materials were studied using photoluminescence (PL) spectroscopy as shown in Figure III.11.

For the starting 2D materials, an intense emission peak at 525nm as well as shoulder (at 450nm) are observed in the PL spectrum for GO. A large band at 440nm and intense peak at 411nm are obtained in the PL $WS_2$ spectrum [19].

Compared with the starting components, a different PL behaviour is noted for the different GO@$WS_2$ nanocomposites. Due to the strong interaction between $WS_2$ and GO, a quenching effect in the photoluminescence is observed at 525nm in addition to a new strong

emission located at 398nm. This prior finding is noted also by Krishnamoorthy group and it can be introduced as an indication of the formation of GO@$WS_2$ nanocomposite [20].

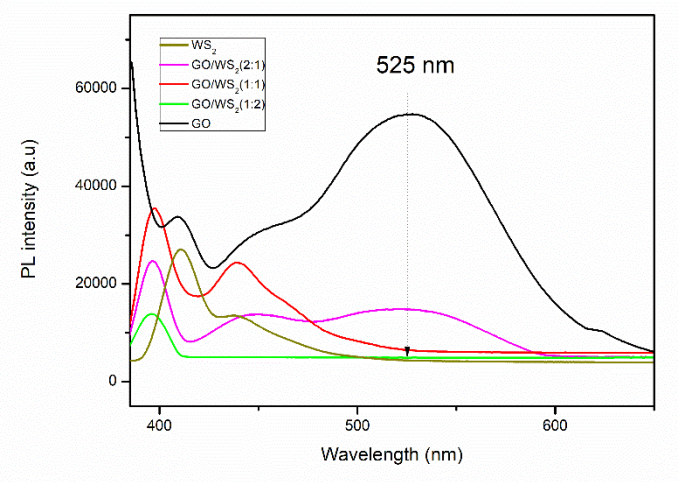


***Figure.III. 11.****Photoluminescence emission spectrum of GO, WS2, and GO:WS2 samples with different ratios.*

## II.4. Electrochemical test

Before the study of the electroanalytical behaviour of the modified electrodes, an electrochemical test is needed. Figure III.12. shows the performed electrochemical impedance spectroscopy (EIS) and cyclic voltammetry (CV) tests, on the bare and the modified SPCE, in ferrocyanide solution ($Fe(CN)_6]^{3-/4-}$) and phosphate buffer solution (PBS), respectively.

Based on the Nyquist plot, we can determine various information. For bare SPCE, we noted a semi-circle and a linear line in high and low frequencies, respectively. The charge transfer resistance is identified by the semi-circle where the linear part identifies the Warburg line [21],[20]. The equivalent circuit revealed from the EIS data is presented in Figure III.12.a. For the modified electrodes, at the interface of the SPCE electrode and the solution, the nanocomposite with a high ratio possesses lower $R_{CT}$ in comparison with GO where the lowest value is noted with GO@$WS_2$(2:1). In agreement with the previous investigation, this finding indicates that the formation of the nanocomposite enhance the electrochemical features of the modified SPCE, see Figure III.12.c [22].

A CV test is recorded for all electrodes in $[Fe(CN)_6]^{4-/3-}$ solution at [-0.2V;0.6V] potential range at 50mV/s scan rate, see Figure III.12. A strong improvement is observed in the $[Fe(CN)_6]^{4-/3-}$ intensity current peak on all modified electrodes compared with the unmodified electrode. The increase in the surface area increases capacitive current which is defined by the enlarging that occurred in the CV cycle. On the modified SPCE, a decrease

in the potential peak difference ΔEp is observed in addition to well-defined and sharp peaks. The cited improvement is due to the increase in the active sites on the $WS_2$@GO surface and to the boost in the process.

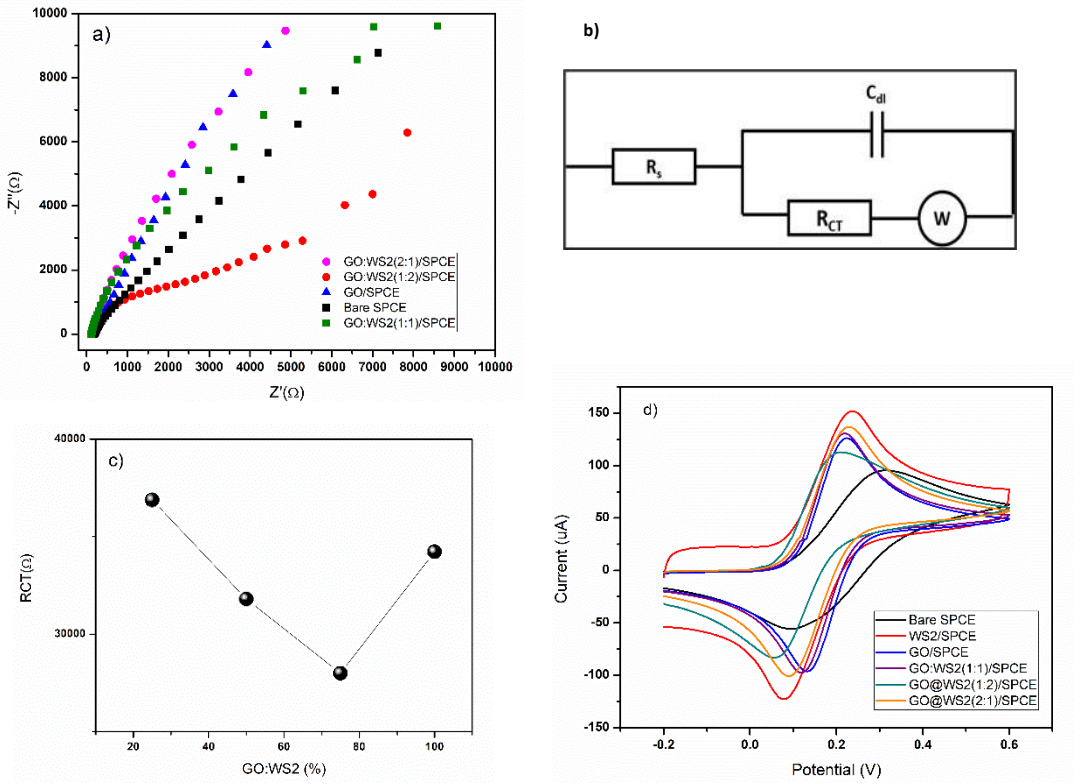


***Figure.III. 12.****a) EIS spectra of bare, GO/SPCE, and GO@WS2/SPCE electrodes; b) equivalent circuit used for fitting EIS data; c) RCT values computed for the electrodes as a function of the GO/WS2 ratio; d) CV test in ferrocyanide solution ([Fe(CN)6]4−/3-)*

## II.5. Electrochemical determination of Thiram

The modified electrodes are used now for the determination of Thiram at low concentrations. All the electroanalytical tests occurred in PBS (pH=7.4, C=0.01M) at a 50mV/s scan rate in the [0V;1.2V] potential range.

The first test was done on the modified electrode and the bare SPCE is CV analysis in PBS containing 0.25µM of thiram as shown in Figure.III.13. From these findings, the modified electrode depicted better performance compared with unmodified SPCE toward the determination of Thiram. Moreover, we noted the oxidation peak of Thiram at 0.6V, and no reduction peak is obtained on both bare and GO@$WS_2$ (1:1) SPCE electrodes. This prior signifies that the process of thiram electrooxidation is irreversible. The variation of Thiram concentration as a function as scan rate (from 0.025V/s to 0.4V/s) will define the sensing

mechanism of the modified electrode, see inset Figure III.13. Indeed, a linear increase in anodic current peak is observed when increasing the scan rate ($i_{pa}$ vs $V^2$), see inset Figure.III.13. This linear relationship indicates that the electrooxidation of Thiram is adsorption-controlled.

Since no cathodic peak current is observed in the preliminary test, the linear sweep voltammetry (LSV) analytical technique is selected for the determination of thiram at different concentrations ranging from 0µM to 0.58µM, see Figure.III.13. A shift to lower potential is observed on GO@$WS_2$/SPCE with an improvement in the anodic current peak of 2 times compared to that of the bare SPCE.

The sensitivity is one of the major features of the sensors that are computed from the calibration curve (Figure.III.14). Based on these data, in a linear range up to 0.35µM, the sensitivity of the modified SPCE is more significant than that of the unmodified SPCE. In agreement with the literature, the obtained enhancement in the sensitivity is due to a couple of facts; the electrocatalytic behavior of $WS_2$ and GO's adsorption capacity for the oxidation of Thiram. These features result in the synergic action that improves the electroanalytical performance of the nanocomposite GO@$WS_2$ [20,23].

In table III.1, we compare the results from this investigation and other findings achieved in the determination of Thiram.

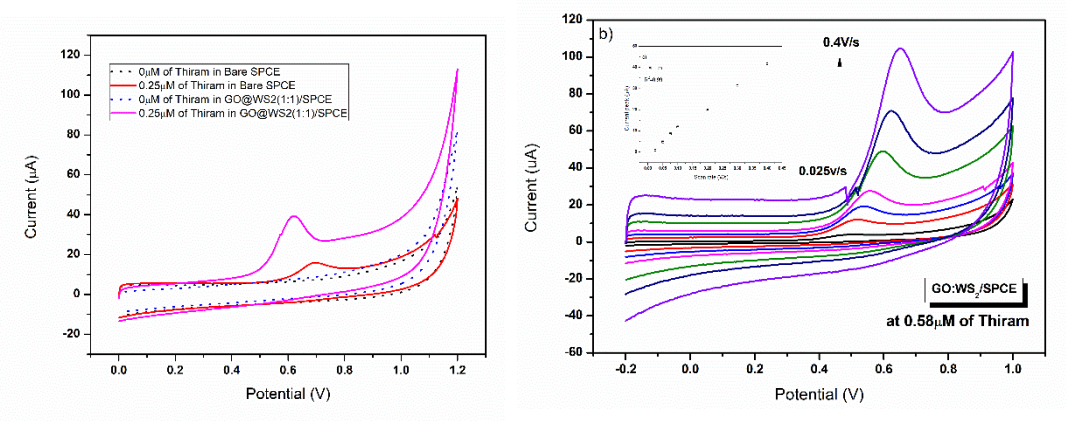


***Figure.III. 13.****CV curves of bare and GO@WS2(1:1)/SPCE sensors in the absence (dots line) and presence of 0.25µM of Thiram (continuous lines). Scan rate variation of (a) GO/SPCE and (b) GO@WS2/SPCE electrodes. Inset the variation of faradic current as function as Thiram concentration*

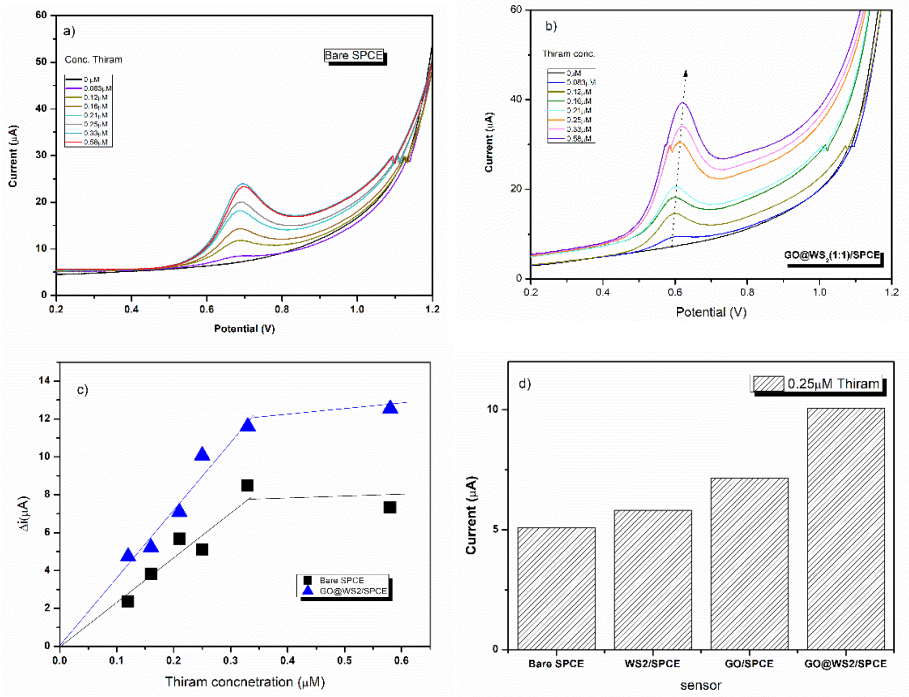


***Figure.III. 14****LSV test of (a) bare SPCE, (b) modified GO@WS2(1:1)/SPCE, (c) calibration curve, (d)* comparison on different sensors of the response to 0.25 µM of Thiram.

***Table.III. 1.****Comparison between the findings obtained with our electrode and other investigations toward Thiram determination*

| Electrode | LOD | Linear range | Electrochemical technique | Ref. |
|---|---|---|---|---|
| GSH-Cu | | 2.5ng mL 1;250ng mL-1 | | 24 |
| NAD+ and K3Fe(CN)6 /SPCE | 0.37 µM | n.r | | 25 |
| Zeolite/CPE | 0.042 µM | 0.014 µM;4.16 µM | DPV | 26 |
| Au/SPCE | 0.092 µM | 0.07- 15 µg mL−1 | Amperometry | 27 |
| GCE dissolved $Cu^2$+ and $Zn^2$+ | n.r | n.r | CV | 28 |
| CPE | 2.07 µM | | DPV | 29 |
| GO/$WS_2$@SPCE | 0.02µM | 0.083 µM;0.33 µM | LSV | This work |

n.r: not regonized

## II.6. Variation of GO@$WS_2$ ratio effect

Since the studied modified electrode in the previous section shows a good performance in the determination of Thiram, we chose to study the effect of the GO@$WS_2$ ratio on the electrooxidation of these organic molecules [30]. Indeed, three modified electrodes were prepared with the following formulation of GO@$WS_2$ (x:y); 1:2, 2:1, and 1:1. For these

electrodes, we apply differential pulse voltammetry (DPV) analytical technique in PBS (pH=7.4, C=0.01M) containing Thiram with concentration varies from 0.083µM to 0.33µM using the following conditions; 0.1V/s as scan rate, pulse width 100ms with initial potential ($E_i$) is 0.2V and final potential ($E_f$) is 1V. All the outcomes are depicted in Figure.III.15. It can be noted as, increasing the amount of GO in the composites, the electrochemical performance of the electrode toward the determination of Thiram is favorite, owing to the combination of the electrical conductivity of GO and the catalytic sites of $WS_2$ nanosheets.

From the calibration curve plotted in Figure.III.14, we noted that the best sensitivity is obtained with the ratio of 2:1. To check the reproducibility of this modified electrode, we performed the same conditions a DPV test after 33 days for the detection of Thiram. From Figure.III.16, we may propose that our modified electrode GO@$WS_2$ (2:1) ratio is reproducible and sensitive to Thiram.

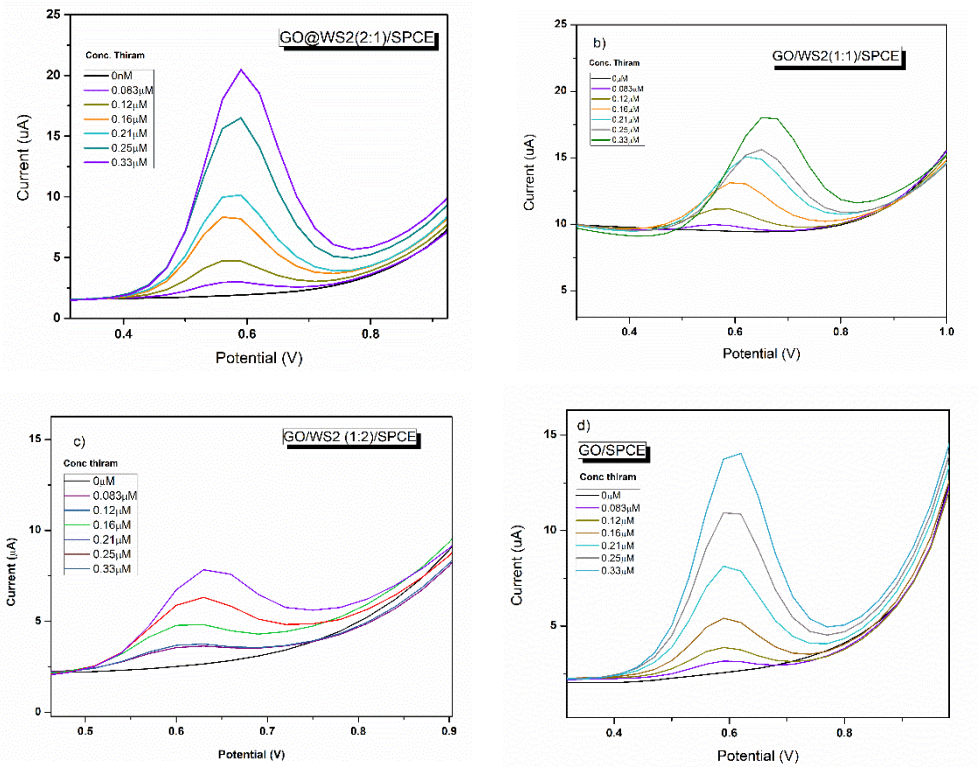

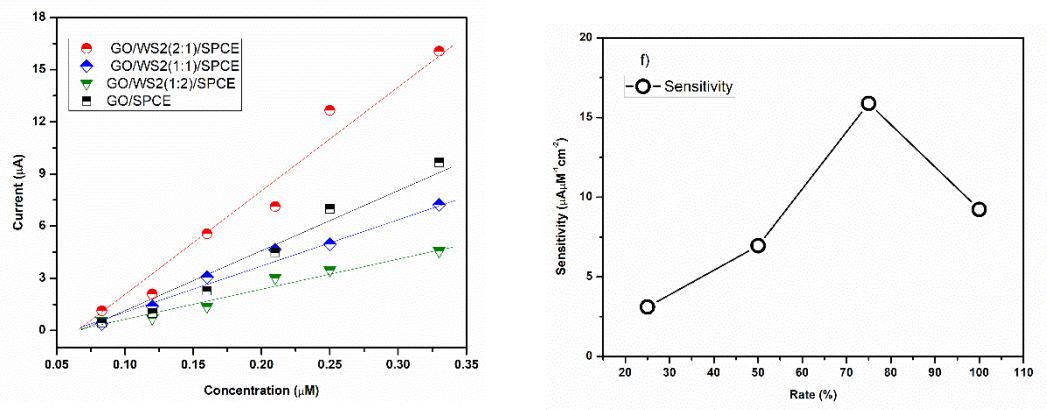


***Figure.III. 15.****DPV analysis of GO@WS2/SPCE (a) 1:2, (b) 1:1%, (c) 2:1,(d) GO/SPCE , (e) calibration curve, and (f) variation of GO:WS2 ratio with respect to GO/WS2 percent in the nanocomposites.*

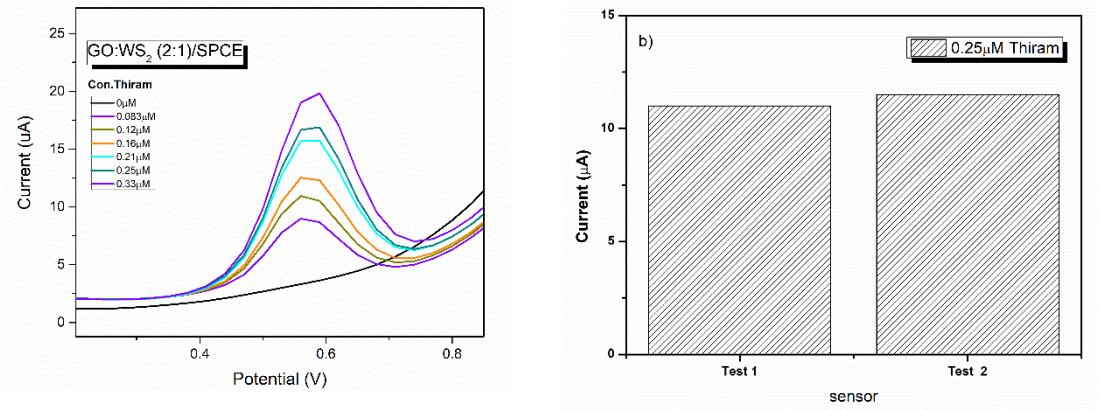


***Figure.III. 16.****Reproducibility of GO@WS2/SPCE sensors. Test 2 performed on GO/WS2(2:!)(@SPCE after 33 days, in the same operative conditions.*

## II.7. Real Sample Thiram determination

Electrochemical detection is an ideal analytical technique for in situ analysis of pesticides, providing high sensitivity, simple sample treatment, and easy operating procedure. Tests above presented have demonstrated that the developed modified SPCE is very sensitive for the determination of Thiram at low traces. Hence, an investigation was also carried out for the determination of Thiram in a real sample. Thiram can be found for example in fruit juice, water river, fruits, food and soil. In this work, we have checked the efficiency of our electrodes in the detection of this dithiocarbamate fungicide in mineral water, spiked with known quantities of Thiram that are below the maximum residue limits (MRLs) for this pesticide, as proposed by EU.

Results using GO/$WS_2$(2:1)@SPCE for determination of Thiram in mineral water, are shown in Fig. III.17.a. Interestingly, the response is the same to that obtained in PBS, indicating that the sensor is not affected by matrix effect. Further, adding to this solution a very high concentration of Mancozeb (M), another well-known fungicide, only a slight increase of the Thiram anodic peak was observed. This finding is promising because allow us to determine the concentration of Thiram also in the presence of this other fungicide. On the other hand, by this electrode is not possible to obtain the simultaneous determination of both fungicides. Further investigations are needed to improve the selectivity of this modified sensing layer.

The results presented in Fig. III.17.b have shown that the sensor reliability is high, i. e. the relative standard deviation is low (the differences between the results obtained in different experiments) showed a coefficient of variation of less than 3%. This was also confirmed also comparing tests carried in PBS and natural water (see Fig. III.17.b)

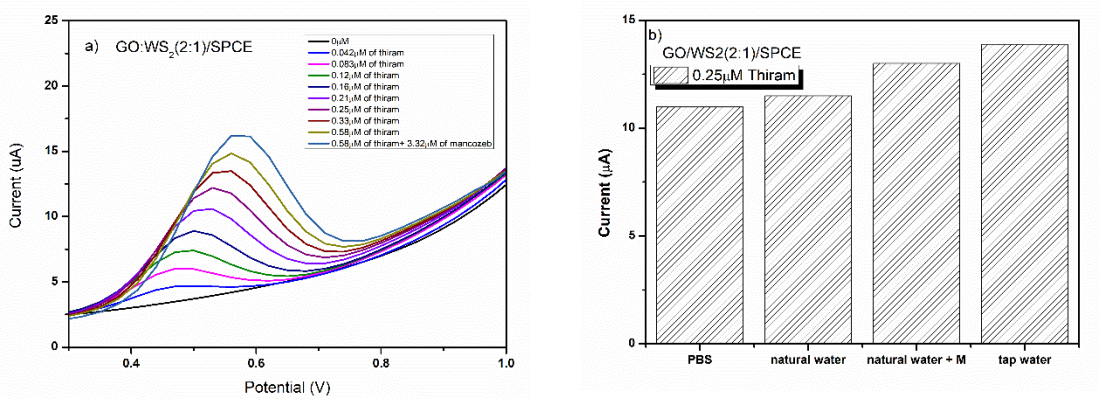


***Figure.III. 17.*** *Reproducibility of GO@WS2/SPCE sensors. Test 2 performed on GO/$WS_2$(75%)(@SPCE after 33 days, in the same operative conditions.*

# III. $MoSe_2$@AuNPs nanocomposite

## III.1. Morphology study of gold nanoparticles (AuNPs)

### III.1.a. Scanning electron microscopy (SEM) discussion

The green-synthesized AuNPs were characterized on SPCE device scanning electron microscopy (SEM). Their outcomes are illustrated in Figure III.18. Indeed, at high magnification, the working surface morphology of SPCE is changed indicating the successful modification of this device with AuNPs while at lower magnification we can note the AuNPs.

Based on these data, we determine that the elaborated AuNPs possess an average spherical shape with an average diameter of 57nm (see Figure III.16.c) [31].

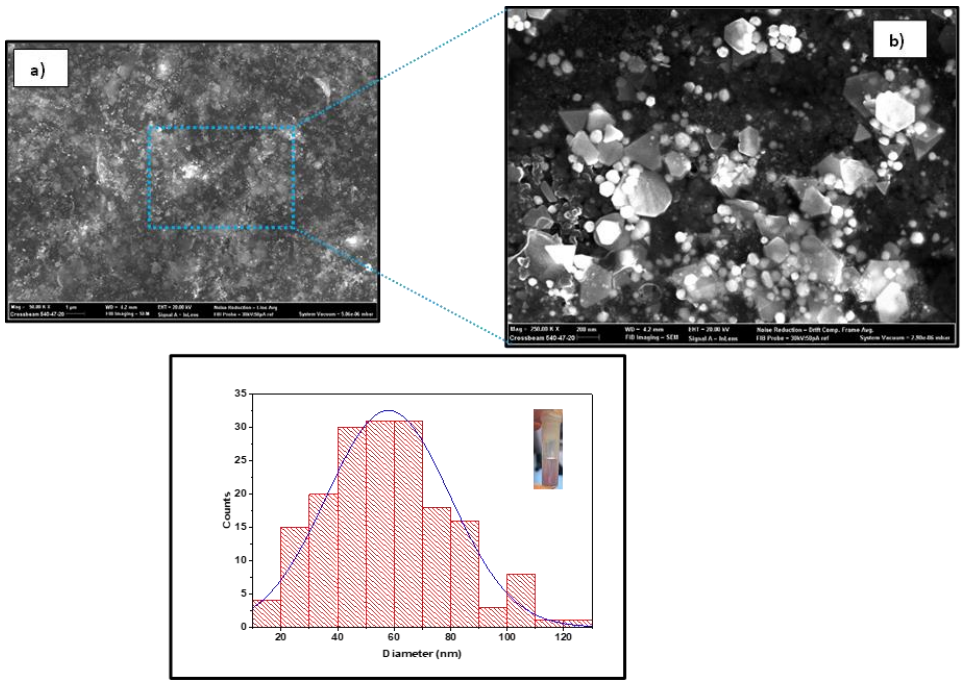


***Figure.III. 18.****SEM images of AuNPs at 1µm (a) and 200nm (b). (c) the histogram distribution*

### III.1.b. Ultra-violet(UV) and dynamics light scattering (DLS) discussion

According to the size and shape of 2D-gold, the localized surface plasmon resonance (LSPR) changes position in the extinction spectrum. In this framework, Figure III.16.a shows the LSPR of the synthesized AuNPs that was observed at 547nm proving that the size of these nanoparticles is 50nm in agreement with Philip, D. work [31]. The obtained findings are in accord with SEM findings and DLS data as presented in Figure III.18.b.

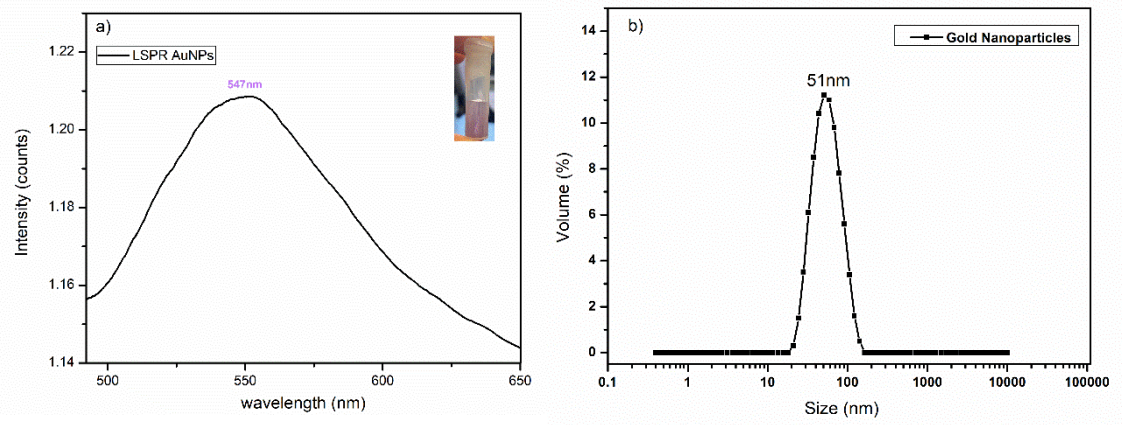


***Figure.III. 19.****(a) LSPR of AuNPs located at 547nm. Inset AuNPs (b) DLS of AuNPs*

## III.2.Ultra-violet (UV) discussion of $MoSe_2$ nanosheets

The exfoliated molybdenum selenide ($MoSe_2$) at different two different centrifugation power (1.5Krpm and 5Krpm) were characterized by a UV tool in the range [500nm;900nm] at room temperature. The outcomes of this characterization are shown in Figure III.19.a-b where we noted two excitonic transitions at the K-point of the brouillon zone (BZ) resulting in two excitonic bands at 1.54eV (A band) and 1.77eV (B band) identifying that we have 2H-$MoSe_2$ polytype [32,33,34,35]. Moreover, two bands are observed at around 295-420nm identified to C and D bands indicating the same origin as in $MoS_2$[36].

From UV findings, we can determine various information citing concentration of the dispersion, length and number of layers, and bandgap value. Indeed, using the Beer-Lambert law at the B band, we can calculate the concentration of the $MoSe_2$ dispersion through equation 1 [34].

$$A_B = \alpha \lambda l \, C \quad (eq\ 1)$$

This equation relates the absorbance 'A', absorption coefficient 'α', the concentration 'C', and optical path 'l' is equal to 10mm. According to Woodward, R. I. et al work, $\alpha_{700}$ is equal to 615 L $g^{-1}m^{-1}$ [34]. Therefore, the concentration of $MoSe_2$ exfoliated at 1.5Krpm and 5Krpm are 0.92$gL^{-1}$ and 0.46$gL^{-1}$, respectively.

Since $MoSe_2$ has been studied recently, there is no wide investigation regarding these nanosheets. However, owing to the similarity of this compound to the other sulphur TMDCs materials, we can use the equation (1) with the local minimum at 380nm to determine the average length <L> that is found equal to 116nm and 196nm for 1.5Krpm and 5Krpm, respectively [37].

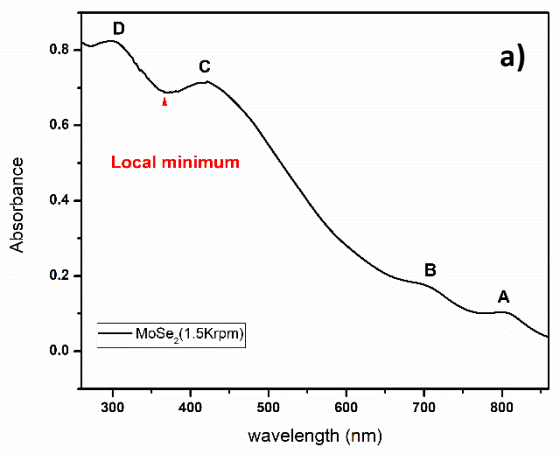

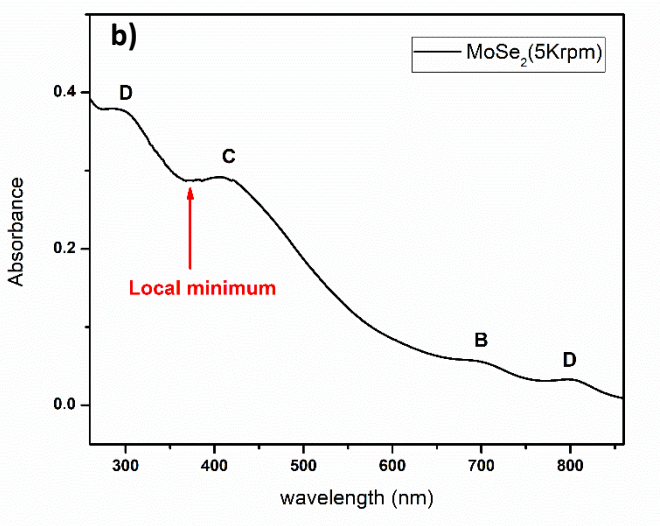


***Figure.III. 20.****Absorption spectra of (a) MoSe2(1.5Krpm) and (b) and MoSe2 (5Krpm)*

## III.3. Raman of $MoSe_2$

Raman spectroscopy is a non-destructive and powerful technique that is used for the vibrational characterization of different samples and within several parameters are determined. Five vibrational modes are identified for a monolayer of $MoSe_2$ with the following irreducible representation according to the group theory [38]:

$$\Gamma = A_{2u}\,(IR) + E_{2g}\,(R) + A_{1g}\,(R) + E_{1g}\,(IR+R)$$

R and IR are defined for active Raman modes and active infra-red modes, respectively.

At room temperature and under a 638nm laser line, $MoSe_2$ (1.5Krpm and 5Krpm) dropped on p-dopped $Si/SiO_2$ slide Raman spectra were collected and presented in Figure III.21.

The spectra are dominated by the prominent characteristic mode at between 239-242$cm^{-1}$ named for out-of-plane mode ($A_{1g}$). Moreover, we observed the in-plane ($E^1_{2g}$) mode located at 284$cm^{-1}$. Both wavelength and intensity of these main vibration Raman modes are sensitive to $MoSe_2$ thickness. In fact, a decrease in $A_{1g}$ position and an increase in $E_{2g}$ position are noted when decreasing the number of the layers.

The success of the few-layered $MoSe_2$ obtention is identified by two facts. The first one is the strong $A_{1g}$ intensity compared with that of $E^1_{2g}$. The second is the red shift in the $A_{1g}$ position due to the increase in the centrifugation power results in the decrease in the number

of layers, see Figure III.20. The observed shift in the $A_{1g}$ position from $MoSe_2$ (1.5Krpm) to $MoSe_2$(5Krpm) resulted from the increased of centrifugation power resulting in the weak inter-binding, then, indicating the successful exfoliation of $MoSe_2$ nanosheets [39,40]. According to Sun, Z. et al. work, a red shift is observed with the different $MoSe_2$ number of layers due to Davydov splitting [41].

In sulphur TMDCs 2D materials, the difference in wavelength of out-of-plane and in-plane modes $\Delta\omega$ ($A_{1g}$-$E^1_{2g}$) is used as an indicator for the number of layers (N). However, non-similar to these materials, the number of layers (N) is determined from Raman spectra based on either the difference of $\Delta\lambda$($A_{1g}$-Si) or the intensity ratio of $A_{1g}$ and Si [42 ,43]. The first indicator remains constant when N is higher than 9 and in our case, the decrease in the ratio value noted for 5Krpm and 1.5Krpm indicates that we have up to 9 layers [43]. Using the $A_{1g}$ and Si intensities ratio ($I_{A1g}/I_{Si}$), we found that this ratio indicates the exfoliation of 5 layers for 1.5Krpm and 3 layers for 5Krpm [43].

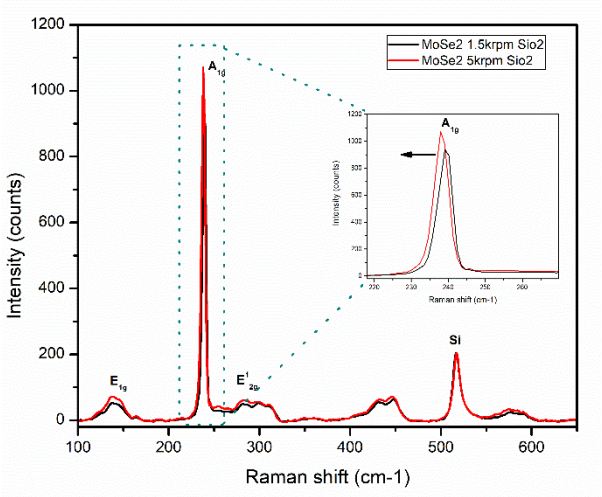


***Figure.III. 21.****Raman spectrum of MoSe2 nanosheets (NS) at 1.5Krpm(black line), and 5Krpm (red line) dropped on p-doped Si/ SiO2*

## III.4.Electrochemical test on $MoSe_2$-based electrodes

The modified electrodes were tested with electrochemical impedance spectroscopy (EIS) and cyclic voltammetry (CV) in ferrocyanide solution $[Fe(CN)6]^{3-/4-}$. Figure III.22.a shows the CV outcomes for the different sensing layers; $WS_2$ (1.5Krpm), $MoS_2$ (1.5Krpm), and $MoSe_2$ (1.5Krpm). An increase in the intensity of $[Fe(CN)6]^{3-}$/$[Fe(CN)6]^{4-}$ with $MoSe_2$/SPCE compared with other modified and unmodified electrodes due to the higher surface area of these sensing layers. This finding is proved also by the EIS spectra shown in Figure III.21.b. Two parts are observed in the Nyquist plot. The first one is the semi-

circle assigned for the limited process of electron transfer. The electron transfer resistance ($R_{CT}$) is identified by the semi-circle radius obtained in Figure.21.b. The second part is the Warburg line identifying the limited diffusion. The obtained shape is illustrated in Figure III.16.b the conductive surfaces of the modified working electrodes [21]. When the non-conductive molecules block the charge transfer, the value of $R_{CT}$ will be higher [21]. This case is observed in our investigation, where the $R_{CT}$ of $WS_2$ is higher, and in agreement with Loo, A. H. investigation, $MoSe_2$ has the best charge transfer kinetics compared with sulphide 2D-materials [44]. The characteristic Randles parameters are presented in Table III.2.

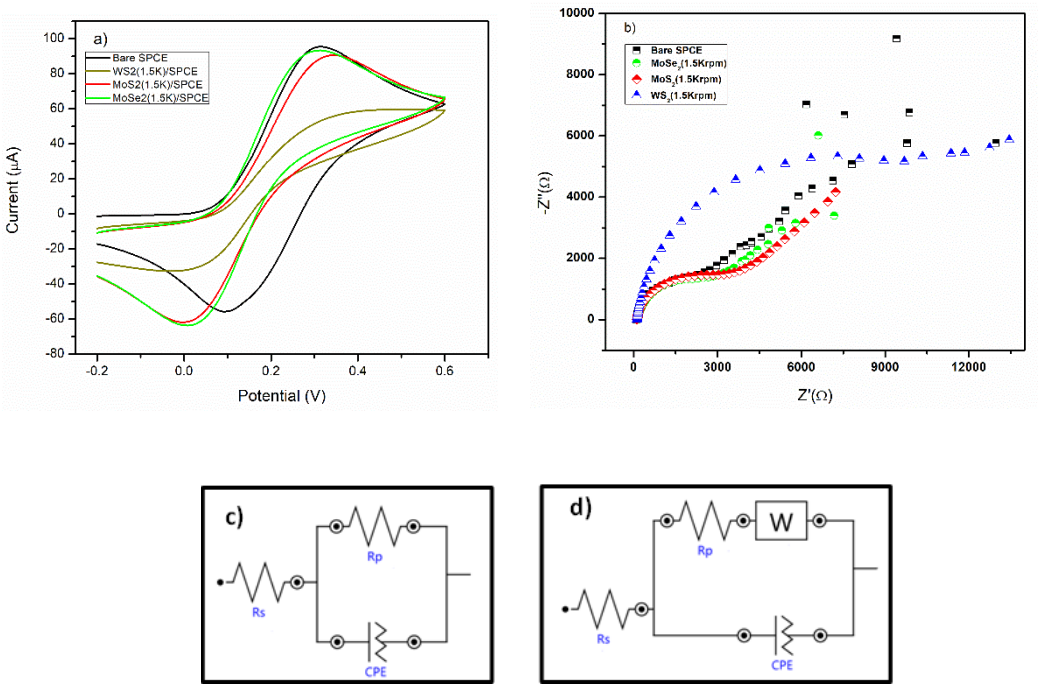


***Figure.III. 22****.(a) EIS spectra of unmodified and modified electrodes, (b) the obtained and (c) simulated equivalent circuit*

***Table.III. 2.****Randles circuit equivalent parameters*

| Electrode | Randle's circuit parameters | |
|---|---|---|
| | $R_{CT}$ (Ω) | $R_s$ (Ω) |
| Bare SPCE | 5022 | 46 |
| $MoSe_2$(1.5K)/SPCE | 4918.1 | 133.11 |
| $MoS_2$(1.5K)/SPCE | 4932.3 | 47.012 |
| $WS_2$(1.5K)/SPCE | 14522 | 17.852 |

## III.5. Electroanalytical determination of dopamine (DA) on $MoSe_2$-based SPCE

Due to the importance of the determination of DA, we will check the efficacy of the modified electrodes toward the determination of this neurotransmitter molecule.

A brief CV test for comparison purposes is performed for the $MX_2$/SPCE in PBS containing DA with concentration ranges from 3µM to 100µM at 0.05V/s in [-0.4V; 0.8V], as shown in Figure III.23.a-b-c. Herein, as expected $MoSe_2$ (1.5Krpm) shows better performance and sensitivity than the other SPCE, Figure III.23.d. Indeed, an increase in faradic current of DA is observed owing to the large surface area, increase in the active sites, and high electric conductivity of $MoSe_2$(1.5Krpm) sensing layers. The various electrochemical performance noted with the different $MX_2$/SPCE is due to the electronic structure, conductivity, and carrier mobility.

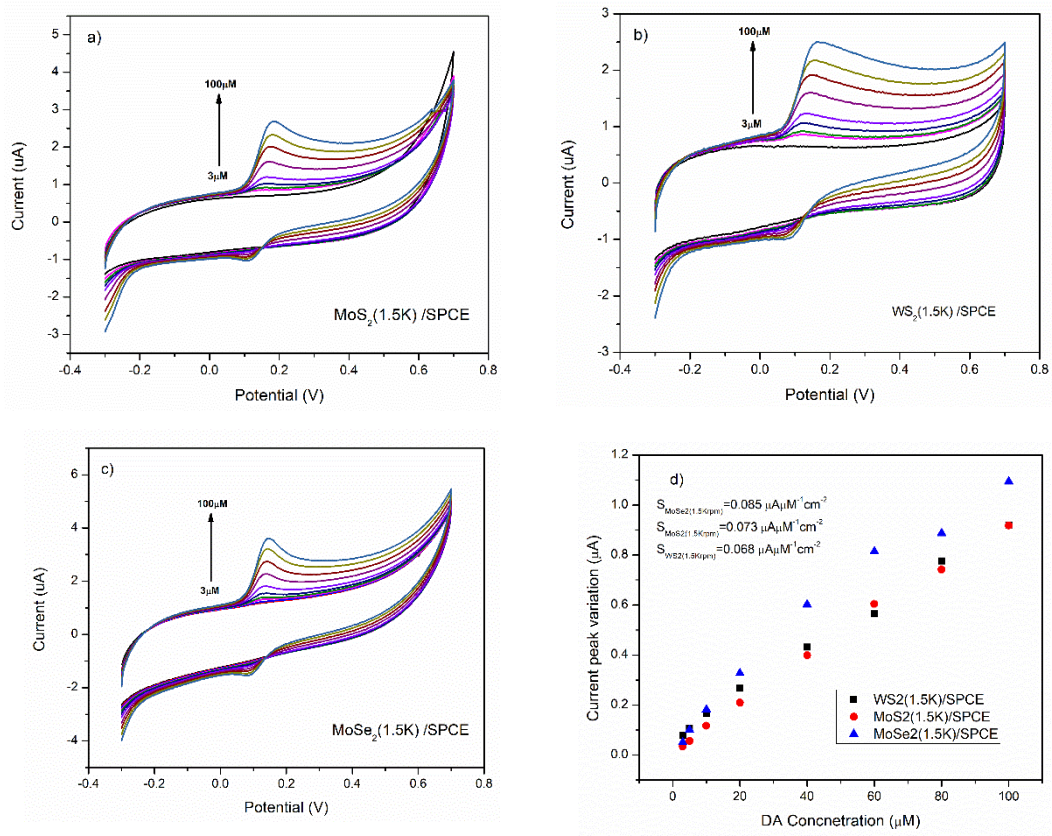


***Figure.III. 23.****CV curves of DA in (a) MoS2/SPCE, (b) WS2/SPCE, (c) MoSe2/SPCE, and (d) calibration curve*

From the data above, we will check the efficiency of $MoSe_2$ (1.5Krpm and 5Krpm) sensing layers toward the determination of DA at different concentrations ranging from 0.5µM to

80µM. The CV findings of these modified electrodes are depicted in Figure III.24. It is clear that modifying the working electrode with $MoSe_2$(5Krpm) shows a better response in Faradic current of DA at lower concentrations (less than 3µM) compared with the other modified and unmodified SPCE. This prominent result is related to the decrease in the number of layers when increasing the centrifugation power in the elaboration process of $MoSe_2$ i.e low number of layers of $MoSe_2$ nanosheets results in improvement of electroanalytical response and conductivity of the SPCE. The sensitivity obtained with $MoSe_2$(5Krpm)/SPCE boosted with ~3 and ~4 magnitudes compared with bare and $MoSe_2$(1.5Krpm) SPCE, respectively.

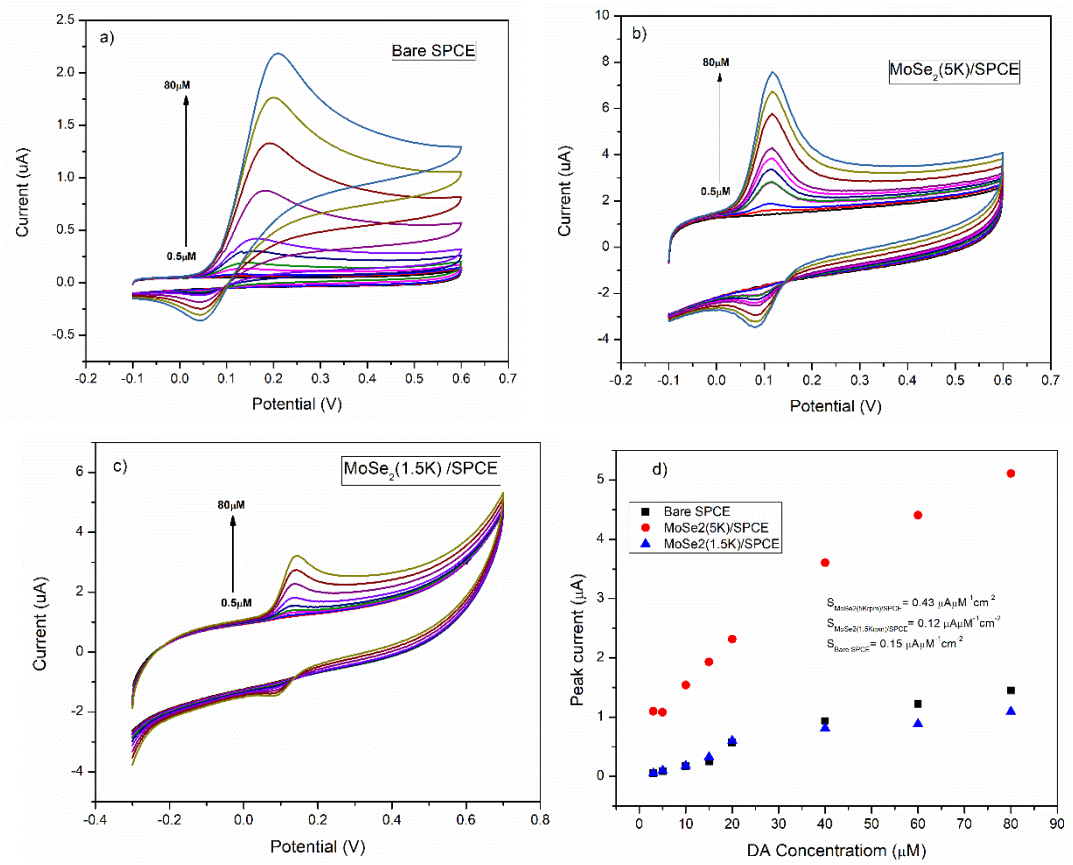


***Figure.III. 24.****CV curves of (a) bare/SPCE, (b) MoS2(5K)/SPCE, (c) MoSe2(1.5K) from 0.5µM to 100µM, and (d) calibration curve*

Since our goal is to develop a sensitive sensor, we modified the working electrode of unmodified SPCE with Au@$MoSe_2$(5Krpm) nanocomposite and we checked its efficiency and sensitivity toward DA as illustrated in Figure III.25.a. Compared with the CV outcomes of bare and $MoSe_2$(5Krpm) electrodes, the nanocomposite shows a crucial enhancement in the Faradic current of DA owing the good charge transfer between the sensing layers (Au-

$MoSe_2$). This fact increases the number of active sites on the Au@$MoSe_2$(5Krpm) matrix interacting with DA molecules.

The sensitivity of this modified SPCE is computed based on the calibration curve where it was noted that the sensitivity of Au@$MoSe_2$ (5Krpm)/SPCE is significantly improved by a factor of 8 compared with the unmodified electrode and 3 times compared with pure $MoSe_2$(5Krpm)/SPCE, see Figure III.25.b.

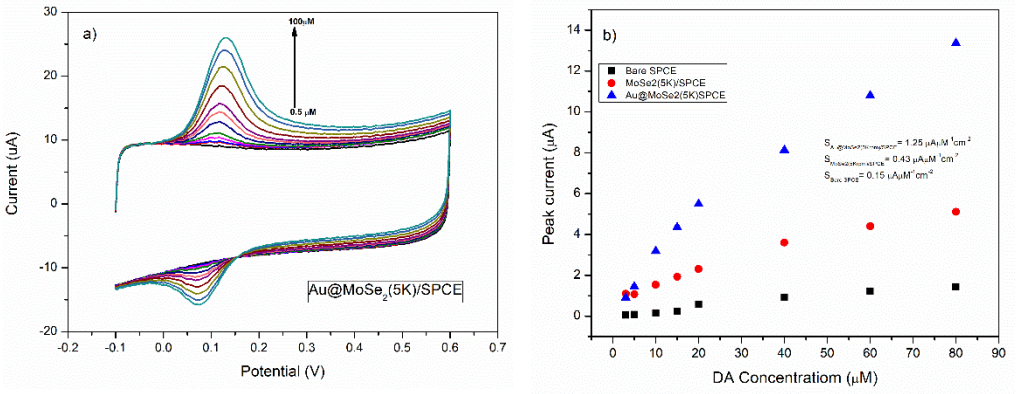


***Figure.III. 25.****(a) CV curve of Au@MoSe2(5K)/SPCE in PBS containing DA and (b) the calibration curve*

## III.6. Selectivity test of $MoSe_2$(5Krpm)-based electrodes

Further to the sensitivity, selectivity is one of the sensor's major characteristic parameters. To determine this feature, we need to check the efficacy of the modified electrodes at a similar potential in PBS containing DA and its interference bio-molecule i.e. uric acid (UA). The selectivity test is performed for $MoSe_2$(5Krpm)/SPCE and Au@$MoSe_2$(Krpm)/SPCE using CV analytical technique in PBS electrolyte with 60µM of DA and UA at different concentrations ranging from 7.7µM to 61.6µM. For both modified electrodes, the DA Faradic current remains constant when varying the UA concentration, however, a slight change is noted with Au@$MoSe_2$/SPCE when the UA is more than 30µM (Figure III.26).

Based on these data, we have determined that the relative standard deviation (%RSD) is equal to 2.6% and 4.1% for $MoSe_2$(5Krpm)/SPCE and Au@$MoSe_2$(5Krpm)/SPCE, respectively. This finding indicates the good reproducibility and repeatability of these sensors.

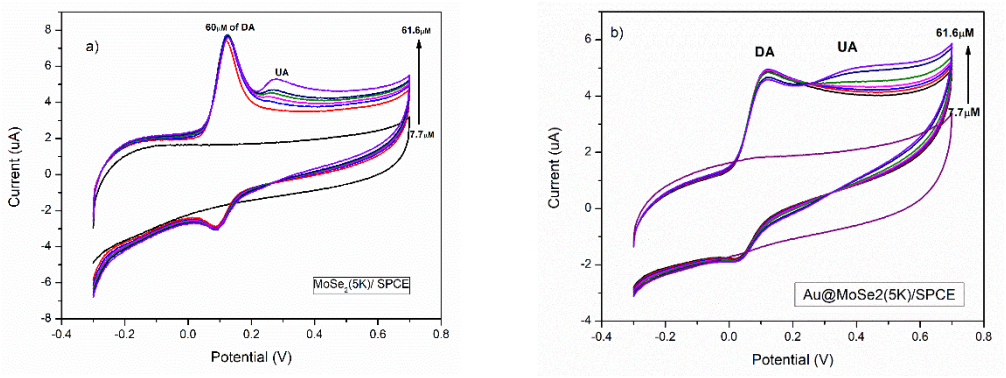


***Figure.III. 26.****CV curves of MoSe2(5K)/SPCE, Au@MoSe2(5K)/SPCE in PBS containing 60µM and UA in different concentration*

## III.7. DA determination in real sample

Further to both selectivity and sensitivity features, it is crucial to check the performance of the modified sensor in a real sample. In this framework, we achieved a CV test on both $MoSe_2$(5Krpm)/SPCE and Au@$MoSe_2$(5Krpm)/SPCE in PBS containing real tyrosine and spiked DA as well as UA. The outcomes of this study are depicted in Figure III.26 that is occurred in three phases; starting with the addition of a 30µM spike DA that remains constant and we add then real tyrosine to electrolyte solution at different concentrations ranges from 10µM to 100µM. Then, at 100 µM of Tyrosine, we increase $C_{DA}$ to reach 100 µM. In the final phase, we conserve both tyrosine and DA concentrations at 100 µM and we add UA up to 226 µM that interfere with DA at the same potential.

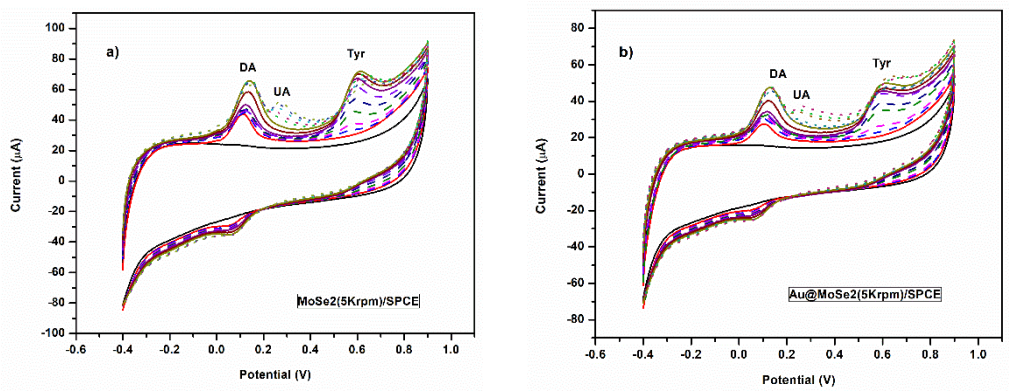


***Figure.III. 27.****CV test of (a) MoSe2(5Krpm)/SPCE, (b) Au@MoSe2(5Krpm)/SPCE in PBS containing real Tyrosine spiked of DA and UA; dots lines is when CTyr increase and CDA remains constant, continuous line CTyr=100µM and CDA is varying, and dots lines CDA and CTyr remains constant at 100µM while UA concentration varies*

# Results & Discussion

## Plasmonic Sensors

# Chapter III

## Results & Discussion: Plasmonic Sensors

### Table of Contents

# Chapter III

## Results & Discussion: Plasmonic Sensors

### Table of Figures

# Chapter III

## Results & Discussion: Plasmonic Sensors

### Table of Tables

# Chapter III

## Results & Discussion: Plasmonic Sensors

### Table of Schemes

# Chapter III

## Results & Discussion: Plasmonic Sensors

### Acronyms and Abbreviations

All the abbreviations used in this chapter are listed below:

- ERS: Enhanced Raman spectroscopy
- MBA: 4-mercaptobenzoic acid
- Au@$WS_2$: Gold nanoparticles-tungsten disulphide
- LSPR: Localized surface plasmon resonance
- SERS: Surface-enhanced Raman spectroscopy
- PIERS: Photo-induced enhanced Raman spectroscopy
- CT: Charge transfer
- EM: Electromagnetic
- ED: electron density
- W: work function
- CB: conduction band
- VB: Valence band
- $E_F$: Fermi level
- AEF: Analytical enhancement factor
- $MS_2$: Metal sulphide
- MB: Methylene blue

# Overview

In this section, we will focus on the use of the exfoliated metals disulphide ($MS_2$; M=Mo/W) and molybdenum selenide ($MoSe_2$) in the plasmonic sensing field for different analyte detection at low concentrations.

## I. Enhanced Raman spectroscopy (ERS) $WS_2$ substrate

The exfoliated $WS_2$ nanosheets were coated with gold nanoparticles synthesized with the Turkish-Frens technique. This nanocomposite is used later for plasmonic sensing. First and foremost, this Au@$WS_2$ nanocomposite is checked with a Raman molecule known as 4-mercaptobenzoic acid (MBA) to check its efficiency in PIERS and SERS [45].

### I.1. Raman discussion of 4-mercaptobenzoic acid (MBA)

Before the ERS study, we performed Raman characterization using a 633nm excitation on MBA to distinguish its characteristics and Raman modes as illustrated in Figure.III.1. We noted two peaks dominating the spectrum at 1098cm$^{-1}$ and 1595cm$^{-1}$ identified for ring breathing and ring breathing axial deformation modes, respectively. Further to these prior peaks, various vibrational Raman modes are observed at high and low frequencies region that are grouped in Table.III.1.

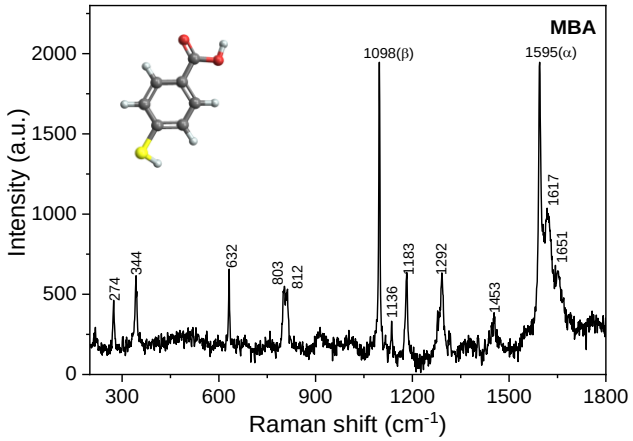


***Figure.III. 1.*** *Raman spectrum of MBA*

***Table.III. 1.****Raman modes frequencies and assignments of MBA compared to the SERS/PIERS modes of MBA absorbed on WS2-AuNPs*

| Normal Raman modes ($cm^{-1}$) | SERS/PIERS modes ($cm^{-1}$) | Assignements |
|---|---|---|
| 274 | **** | Au-S |
| **** | 420 | Out-of-plane mode ($A_{1g}$) of $WS_2$ |
| 344 | **** | C-H in-plane deformation, β(C-H) |
| **** | 522 | Ring out-of-plane bending |
| 632 | 633 | OCO bending and C-S stretching, δ(O-C-O)& ν(C- S) |
| 1098 | 1075 | In-plane ring breathing mode |
| 1183 | **** | C–O stretching, ν (C- O) |
| 1453 | 1480 | COO- stretching, ν(COO-) |
| 1595 | 1584 | Ring breathing axial deformation modes |
| 1617 | 1706 | C=O stretching, ν(C=O ) |

## I.2. ERS behaviour of Au-$WS_2$ substrate

To check the efficiency of Au-$WS_2$ substrate, it was used as ERS platform for the determination of MBA molecules. Compared with the conventional Raman spectrum of MBA, a redshift is observed in most of the Raman reporter molecules using the SERS-Au@$WS_2$ substrate. This shift is originated from the binding between Au and the reporter molecule resulting in polarizability change in agreement with Ma,H. et al [46], [47]. The obtained SERS spectrum is dominated by two characteristic vibrational Raman modes of MBA located at 1075$cm^{-1}$ and 1584$cm^{-1}$ with the same assignments described in the previous section.

Similar to Ma, W. et al investigation, they have observed that the presence of the in-plane ring breathing (at 1075$cm^{-1}$) is an indication of a certain angle 'θ' between AuNPs surface and the benzene ring plane [48]. Moreover, the highest intensity observed in this mode may be identified that the adsorption of MBA on AuNPs occurs through the S atom. A characteristic Raman mode of $WS_2$ is observed also in the SERS spectrum at 420$cm^{-1}$ assigned for out-of-plane ($A_{1g}$).

For the PIERS spectrum, on 1584$cm^{-1}$, we computed the enhancement factor (AEF) using equation 1 which is found around 4 compared with SERS ($AEF_{SERS} \sim 2\times10^5$ and an $AEF_{PIERS} \sim 9\times10^5$)due to the migration of charge from $WS_2$ (semiconductor ) to

nanoparticles (AuNPs), upon the UV irradiation. This prior leads to an extra charge transfer (CT) and a chemical enhancement [49].

$$\mathbf{AEF} = \frac{\mathbf{I_{SERS/PIERS}}/\mathbf{c_{SERS/PIERS}}}{\mathbf{I_{Raman}}/\mathbf{c_{Raman}}} \qquad \mathbf{eq(1)}$$

This major parameter identifies the factor of improvement in the Raman signals. Indeed, $I_{Raman}$, $I_{SERS/PIERS}$ are the intensities of the selected modes in conventional and SERS/PIERS spectra, respectively. The concentration of the analyte used in Raman and ERS characterization.

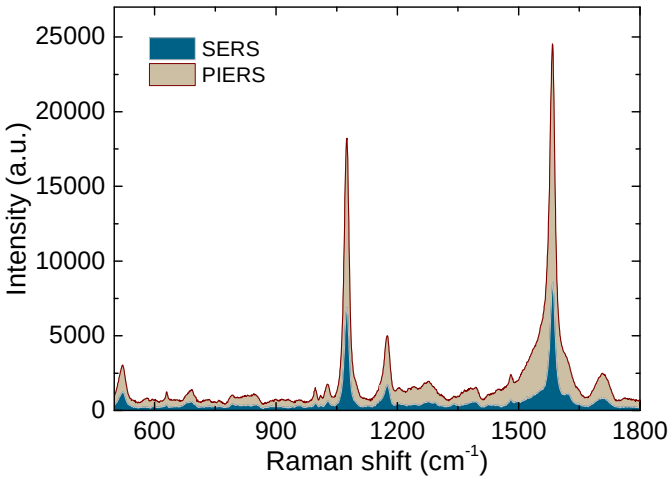


*Figure.III. 2. SERS (blue area) and PIERS (grey area) spectra of MBA ($10^{-5}$M) on Au@WS2*

Scheme III.1 depicts an explicative and descriptive sketch of the mechanism that occurred in the PIERS substrate. Herein, upon the UV-C irradiation, the LSPR of the AuNPs are bombarded increasing the electromagnetic field and the charge transfer (CT) between the substrate sensing layer and that between substrate-analyte. This contributes to the improvement of the Raman signals.

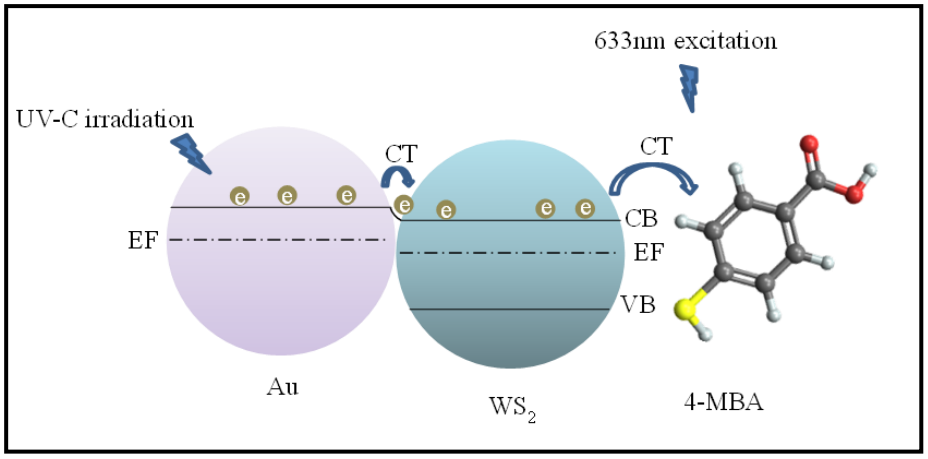


***Scheme.III. 1.****Sketch presenting the phenomena occured upon the UV-C irradiation in PIERS technique*

The pre and post-UV-C extinction spectra were collected at ambient conditions and presented in Figure.III.3. In the post-irradiation spectrum (red line), the LSPR is located at 547nm which is redshifted compared with the extinction spectrum of AuNPs (at 520nm), see Figure. This offset may be an indication of some aggregation happening upon the adsorption of AuNPs on the $WS_2$ surface. Compared with pre and post-spectra, we observed a blue shift with ~5nm defined to $WS_2$-AuNPs charge transfer (CT) and the increase of electron density (ED) resulting in the activation of AuNPs. In agreement with the literature, we can compute the ED variation ($\Delta N/N$), found to be 1.8%, through the following equation [50,51]:

$$\frac{\Delta N}{N} = -2\frac{\Delta \lambda}{\lambda} \qquad \textbf{eq(3)}$$

The $\Delta\lambda$ is the LSPR peak shift in $Au@WS_2$ nanocomposite.

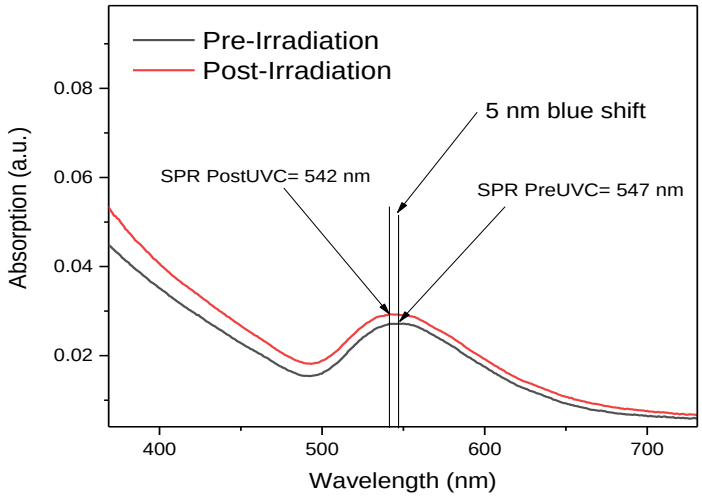


***Figure.III. 3.Extinction spectra of Au@WS2 composites before (black line) and after (red line) irradiation with UVC light at room temperature.***

According to the literature, the CT between Au-$MoS_2$ nanocomposite is obtained with PL quenching of $MoS_2$ [52]. Since $MoS_2$ and $WS_2$ are similar, thus, we propose a similar process with $Au@WS_2$ nanocomposite. Based on the semiconductor theory, we can identify the contact between metal and semiconductor which can be ohmic or Schottky [53]. This type depends on the sign of the work function of these materials [53]. In ohmic contact, electrons flow from metal to semiconductor i.e. the semiconductor work function is greater than that of metal [53]. In the inverse case, a space with a positive charge is generated in the Schottky junction and the Schottky barrier is produced blocking the charge transfer between metal

and semiconductor [53]. With our Au@$WS_2$ nanocomposite, we have an ohmic contact. According to Alessandri, I et al. work, in this junction the high concentration of the electron will generate high conductivity [54]. Based on the literature, the Fermi level of few layers of $WS_2$ is found to be 5.89eV and that of Au is 5.1eV [52], [55]. The energy difference (0.79eV) leads to band bending in Au-$WS_2$. As presented in the scheme.III.2, upon the irradiation of the substrate, AuNPs electrons will be excited and flow to the $WS_2$ [56].

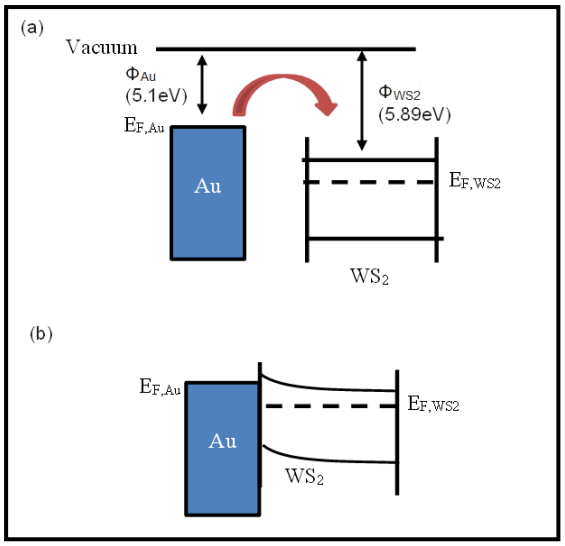


***Scheme.III. 2.****Charge transfer mechanism in Au@WS2 nanoflake. (a) Energy band diagram for Au NPs and WS2 nanosheets showing the relative positions of Fermi levels with respect to the vacuum level. The arrow represents the transfer of electrons from Au to WS2 after the contact is established. (b) Energy band diagram of Au@WS2 nanoflake showing band bending after establishing the contact between Au and WS2* [56].

## II. Au-$MoS_2$ based enhanced Raman spectroscopy (ERS) substrates

### II.1. For MBA detection

In this investigation, we used MBA molecule to check the efficiency of this substrate for ERS applications using Au-$MoS_2$ substrate under the same condition used with Au-$WS_2$ nanocomposite. The outcomes of this investigation are depicted in Figure.III.3. It is noted that the normal Raman vibrational modes of this probe analyte were detected with both SERS/PIERS substrates with a significant improvement in the SERS intensities compared to that of PIERS.

Two characteristic peaks of MBA dominate both ERS substrate located at 1075$cm^{-1}$ and 1581$cm^{-1}$ named a1 and b2, respectively (Figure.III.3). With respect to the previous

investigation, the observation of the first vibrational Raman mode identify the presence of a θ angle between the plasmonic surface and the in-plane breathing ring of MBA as depicted in Figure III.3.b.[57,48] Furthermore, the weak interaction between the gold surface and the carboxyl portion in MBA is identified by the weak intensity of the vibration mode observed at 1393cm$^{-1}$ [48]. In Table.III.2, we grouped all the observed ERS modes with their assignments.

The obtained enhancement compared with the conventional Raman findings make SERS-substrate a good candidate for the detection process at low concentrations. The enhancement factor computed on 1589cm$^{-1}$ vibrational mode for AuNPs, Au-$MoS_2$, and Au-$WS_2$ substrates are found to be ~$4\times10^5$, ~$5\times10^5$. ~$2\times10^5$, respectively. The fact that the SERS signals were boosted 2 times compared with the PIERS ones may be introduced to the electromagnetic enhancement (EM). These results indicate that Au-$MoS_2$ works well with the SERS technique.

Based on the semiconductor theory, we tried to explain the constraint of the PIERS performance of this substrate based on the work function (W) and the junction type. Indeed, the created positive space zone will block the charge transfer when $W_M$ is higher than $W_{SC}$. In the inverse case, the contact nature is ohmic. According to the literature, the Fermi level of 4L-$MoS_2$ and AuNPs is equal to 4.98eV and 5.1 eV [58,59], respectively. In this framework, the Au-$MoS_2$ junction nature is Schottky since $W_{Au}$ is higher than $W_{MoS2}$ (Scheme.III.3). According to Mao, Z. et al, the presence of the Schottky junction is confirmed also through the resulting Fermi energy offset (0.12eV) [60].

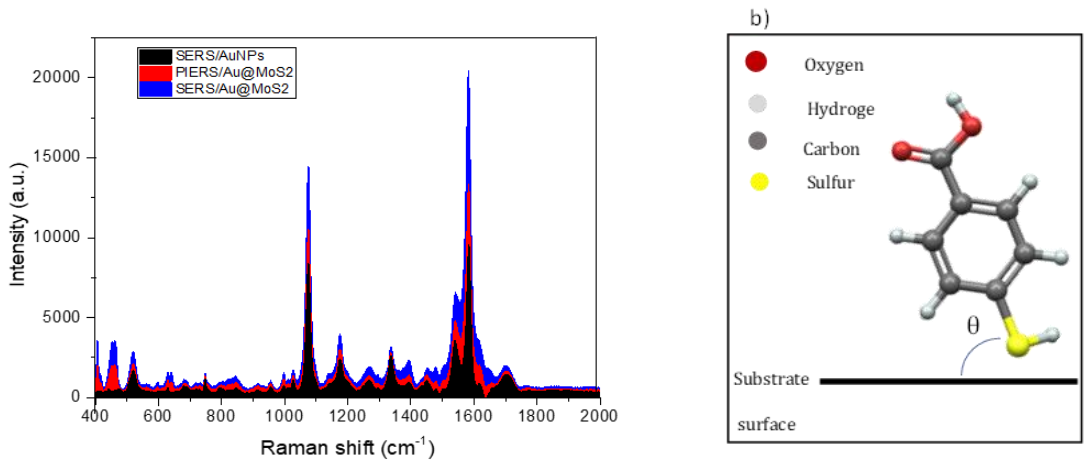


***Figure.III. 4.*** *(a) Room temperature SERS and PIERS spectra of mercaptobenzoic-acid (MBA, 10-5M) on MoS2-AuNPs substrates using 633nm excitation (b) the absorption angle θ of MBA on Au@MoS2.*

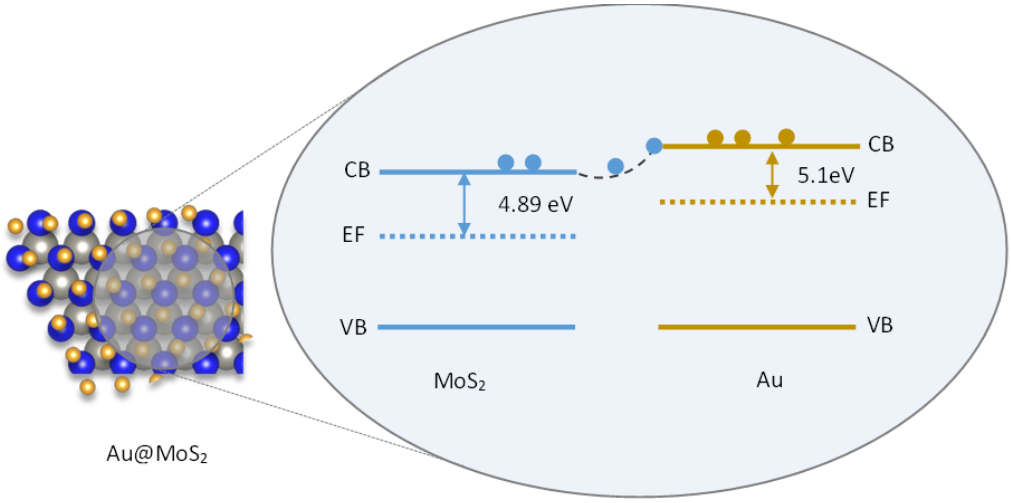


***Scheme.III. 3.****The occuring charge transfer (CT) between Au nanoparticles (NPs) and MoS2 nanosheets (NS) in the Au@MoS2 PIERS sensor*

***Table.III. 2.****Raman frequencies and assignments of normal Raman and SERS/PIERS bands of MBA on Au@MoS2*

| **Normal Raman frequencies ($cm^{-1}$)** | **Raman frequencies ($cm^{-1}$) SERS/PIERS** | **Assignments** |
|---|---|---|
| 274 | **** | Au-S |
| **** | 461 | $A_2u(\Gamma)$ [1] |
| 344 | **** | C-H in-plane deformation, β(C-H) |
| **** | 519 | Ring out-of-plane bending |
| 632 | 633 | OCO bending and C-S stretching,δO-C-O) & νC- S) |
| 1098 | 1075 | Ring breathing mode |
| 1183 | 1175 | C–O stretching, ν(C- O) |
| 1453 | 1393 | COO- stretching, ν(COO-) |
| 1595 | 1581 | Ring breathing axial deformation modes |

The ERS enhancement is delivered by two mechanisms known as a chemical enhancement (CM) and electromagnetic enhancement (EM). The contribution of these mechanisms can be uneven or equal. Indeed, the EM effect is contributed between the substrate and the analyte where its degree ″$P_{CT}$″, found to be (~0.6), is computed based on the intensity ratio of a1 and b1 defined with R in the following equation [61]:

$$P_{CT}=R/(R+1) \qquad eq(6)$$

The analytical enhancement factor (AEF) is determined using equation (1). For the SERS case, this is a factor is found to be almost 3 times higher than that of PIERS. According to our knowledge, the EM effect controls the improvement obtained with the SERS substrate. It is known that the CT contributes more less than the EM effect since in the SERS technique there is no UV irradiation step. Moreover, the CM is sensitive to the analyte-substrate distance [62]. Furthermore, the interaction between the incident electromagnetic wave and the plasmonic surface results in the improvement of the electromagnetic field and in some case lead to the creation of hot spots. Indeed, these active areas have intense energy occurring when the resonance is achieved i.e. incident wavelength is equal to the LSPR.

Similar to the Au-$WS_2$ PIERS substrate described in the previous section, we have determined the electron density (ED) [62,63.] As indicated in the Figure.III.5, no shift is noted indicating that there no additional electron gained by the substrate ($\Delta N/N=0$). This finding is in agreement with our suggestion that the charge transfer is not occurred on Au-$MoS_2$ PIERS substrate.

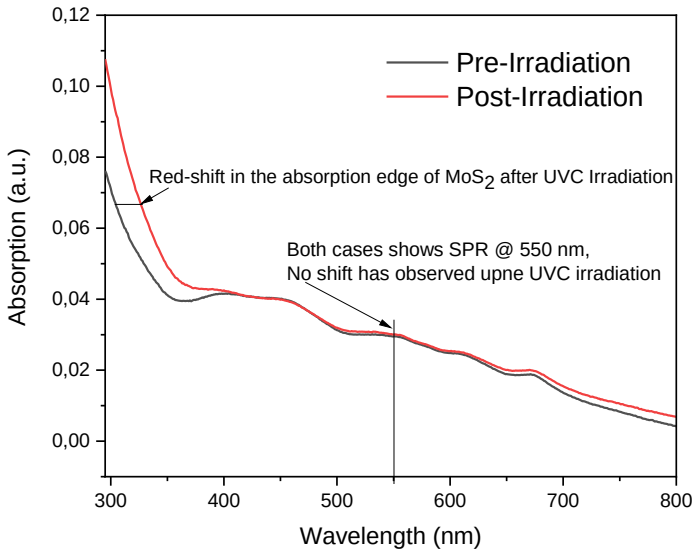


***Figure.III. 5.Pre- and Post-irradiation spectra of Au@MoS2 PIERS chips at room temperature***

## II.2. Folic acid (FA) detection

Besides the electroanalytical test toward FA molecules on the Au-$MoS_2$ SPCE electrode, we checked its efficiency as an SERS substrate at $10^{-4}$M. Upon the analyte-AuNPs interaction is crucial, a significant improvement is obtained in the SERS signals, Thus, the modified AuNPs/SPCE and Au-$MoS_2$/SPCE electrodes were used also as SERS substrate for the determination of folic acid [34]. The outcomes of this test is presented in Figure.III.6.

On bare SPCE, no FA characteristic peaks are noted. On $MoS_2$/SPCE, we observed the SERS effect in addition to two characteristic modes of $MoS_2$ NS named LA(M) (237cm-1) and 2LA (460cm-1). On Au-$MoS_2$/SPCE, an important and clear SERS enhancement is observed where Table. III.3 grouped all the obtained SERS signals of FA. This prior finding introduces the strong chemisorption FA-AuNPs 29, 35.

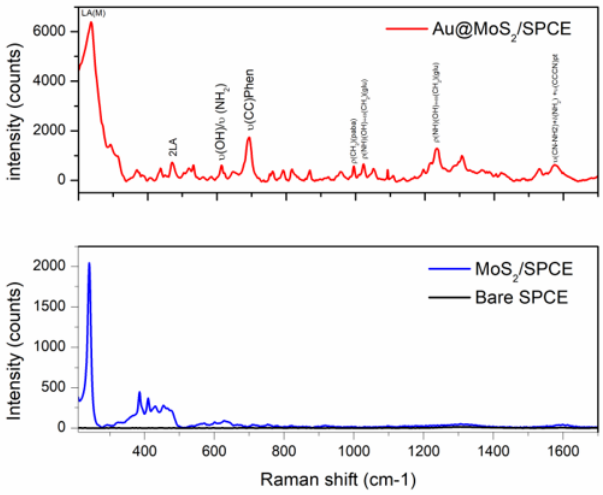


***Figure.III. 6.SERS spectra acquired from FA deposited from a solution $10^{-4}$ M on the investigated electrodes.***

***Table.III. 3.****Assignment of SERS vibrational mode*

| Wavelength (cm-1) | Assignment |
|---|---|
| 237 | LA(M); MoS2 |
| 468 | 2LA; MoS2 |
| 615 | ρ(OH)(pt) IP DEF; ρ(NH2)(pt) OOP |
| 761 | ** |
| 817 | δ (CNO)ρ(OH)(CH2)(Glu); $\nu(C-N)(paba)def$ |
| 959 | ρ (CH2)(paba) |
| 996 | $\nu$(C-C) ρ(CH)(paba)def; ρ(OH)(pt)def; |
| 1024 | ω(CH2)(Glu) + ρ (NH)(OH) |
| 1052 | $\nu$(C-C)(paba) ; ρ(NH2)(CH)(OH)(pt) def; $\nu(C-C)(glu)def$ |
| 1195 | (CH2)(Glu)+δ(OH)(pt) |
| 1238 | ρ(NH)(OH)+ω(CH2)(Glu); ν(CN-NH2)+ ν(CC-CN)pt |
| 1574 | $s(NH_2)+\nu_{as}\ (C=N)(pt)$ or $\nu_s(C-C)+\rho(CH)(paba)$ |

## III. Au-$MoSe_2$ enhanced Raman spectroscopy (ERS) substrates

The metal sulphide ($MS_2$) used in the previous investigations are the most studied 2D-TMDCs materials. Recently, metal selenide gained crucial interest due to its similar structure and better electronic and electrochemical features compared to $MS_2$ 2D materials.

## III.1. Methylene blue (MB) Raman discussion

Methylene blue (MB) or methylthioninium chloride is a dye molecule commonly used for ERS study to check the efficiency of substrate, see Figure.III.7. The conventional Raman spectrum of this dye molecule is performed using 638nm at room temperature on a gold film substrate is illustrated in Figure.III.7.

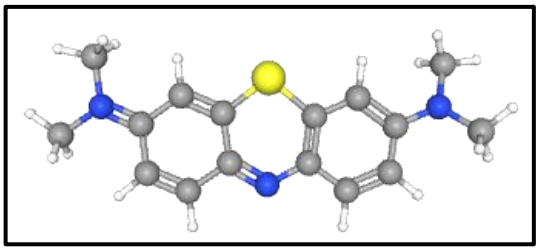

***Figure.III. 7.*** *Methylene blue (MB) 3D molecule structure*

The characteristic peak of MB is observed at 446cm$^{-1}$ and 449 cm$^{-1}$ identifying skeletal deformations of C-N-C [64]. Moreover, two other fingerprints of MB vibrational modes are obtained at 1392cm$^{-1}$ and 1623cm$^{-1}$ indicating C-N symmetric stretching and C-C ring stretching [64].Table.III.4. present all the Raman modes obtained on this substrate with their assignments.

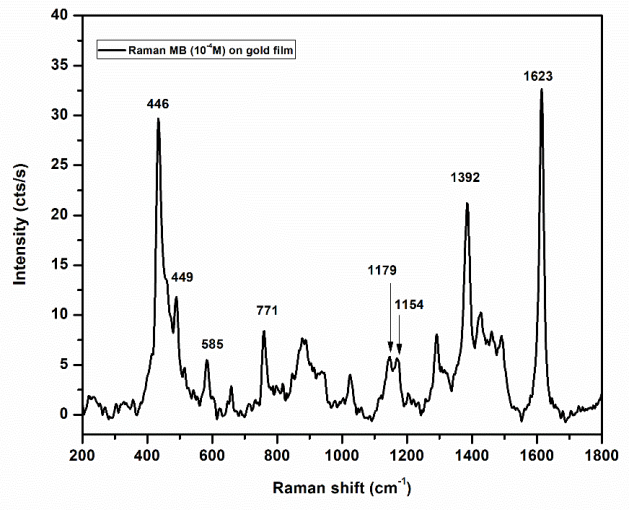


***Figure.III. 8.Raman spectrum of MB($10^{-4}$) on gold film***

***Table.III. 4.****Table regrouping MB(10-4M) Raman mode*

| Mode frequency ($cm^{-1}$) | Assignments |
|---|---|
| 446 | C-N-C skeletal deformation[66] |
| 449 | |
| 585 | C-S-C skeletal deformation[66] |
| 659 | C-H out-of-plane bending[66] |
| 773 | C-H in-plane bending [66] |
| 880 | |
| 1023 | Bending in plane (C-H)/ (C-S) stretching [67] |
| 1179 | C-N streatching[66] |
| 1154 | C-H in-plane bending [66] |
| 1290 | C-H in-plane ring deformation[66] |
| 1392 | C-N symmetric stretching[66] |
| 1429 | In-plane bending N-H-C attached to methyl group [68] |
| 1460 | Scissoring CH2/wagging CH2/ C-H in-plane bending [68] |
| 1493 | C-C asymmetric streatching[66] |
| 1623 | C-C ring stretching[66] |

## III.2. Au-$MoSe_2$ enhanced Raman spectroscopy (ERS) substrates

The efficiency of the prepared AuNRs-$MoSe_2$(5Krpm) substrate is checked using MB ($10^{-4}$M). The SERS and PIERS spectra are illustrated in Figure. Using both ERS substrates, we noted the characteristics of MB Raman modes that were strongly enhanced on the PIERS-Au@$MoSe_2$ substrate compared to that of SERS. This enhancement may be introduced to the pre-irradiation of the substrate that affects the charge transfer between the substrate and the analyte as well as the semiconductor and the noble metals. On the other hand, the pre-irradiation step in PIERS can be considered as a factor that improves the electron bombardment on the Au nanorods surface thus increase of the electromagnetic field.

Using this substrate, we observed almost all the characteristic vibrational modes of MB with a strong improvement especially with the PIERS substrate compared with SERS. Indeed, the major vibrational mode of MB is 47 times significantly enhanced compared to that of Raman and 3 times to that of SERS. Moreover, it is noted that the intensity of MB vibrational modes either medium, high or weak in the Raman spectrum was strongly enhanced. This crucial boost is due to the UV irradiation onto the substrate improving the charge transfer between the sensing layer and consequently the charge transfer between the analyte molecules and the surface. Furthermore, this intensity change can be introduced to

the probe molecules-surface substrate interaction that is sensitive to different facts. The first one is the adsorption sites present on the surface substrate, the orientation of the adsorption, and the PIERS rules related to the adsorbed vibrational mode of the probe molecules on the substrate surface [64], [67].

The enhancement factor is calculated on different prominent vibrational Raman modes of MB, see Table.III.5. The overall PIERS enhancement factor was found to be and compared to **x33** and **x4** SERS and normal Raman.

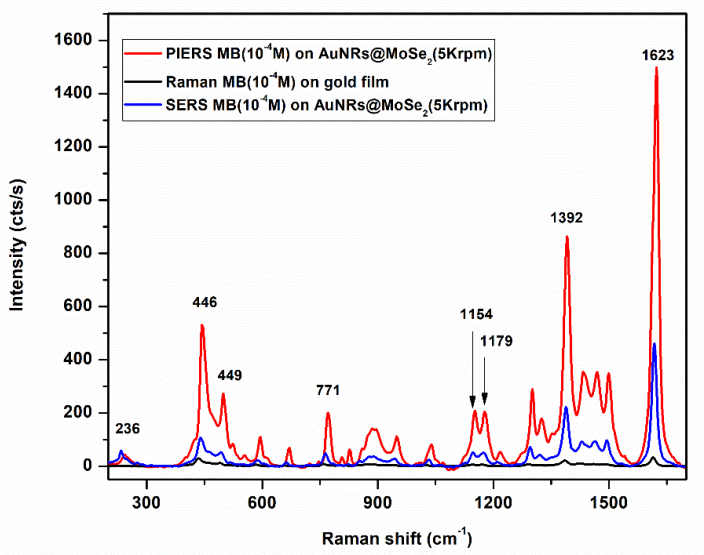


***Figure.III.9. MB normal Raman (black line) on gold film substrate, SERS (blue line) and PIERS (red line) spectra on AuNRs@MoSe2(5Krpm)***

***Table.III. 5.****SERS/PIERS enhancement factor of the main vibrational modes*

| Mode frequency ($cm^{-1}$) | $EF_{SERS}$ compared to Raman | $EF_{PIERS}$ compared to Raman |
|---|---|---|
| 446 | **x5** | **x18** |
| 773 | **x4** | **x23** |
| 1154 | **x4** | **x32** |
| 1179 | **x4** | **x40** |
| 1392 | **x4** | **x41** |
| 1623 | **x3** | **x47** |

It is important to understand the mechanism beyond the PIERS enhancement on the Au-$MoSe_2$ substrate. Indeed, two types of improvement are suggested; electromagnetic (EM) and charge transfer (CT) [68]. Since the PIERS tool is characterized by UV- irradiation, the charge transfer between the sensing layer/molecules is beyond the PIERS enhancement. Herein, two charge transfers (CT) occur; the first one is between the semiconductor and metal. The second one is between the sensing layer and the probe molecules.

Based on our knowledge and previous investigations, we will try to explain the mechanism beyond the PIERS enhancement on the AuNRs-$MoSe_2$ substrate. Indeed, the charge transfer is accomplished upon the UV irradiation between AuNRs and $MoSe_2$. Usually, after this irradiation, the alignment of the fermi level will occurred following the semiconductor theory. In our case, the fermi level of both AuNRs and $MoSe_2$ are already aligned since their work functions are equal to 5.1eV [69,70]. Herein, a great CT occurred. When the MB molecule, the sensing layers are noble metal (AuNRds) and a semiconductor ($MoSe_2$) are in contact, a charge redistribution is achieved [71]. Since the energy offset between CB of $MoSe_2$ (~ 0.22) and LUMO energy level of MB (2.99eV) is lower than the irradiation photon energy (4.5eV), the transfer of the excited electrons is achieved. Therefore, the charge transfer mechanism in the AuNRs-$MoSe_2$-MB system is noted [71], see the scheme. III.5.

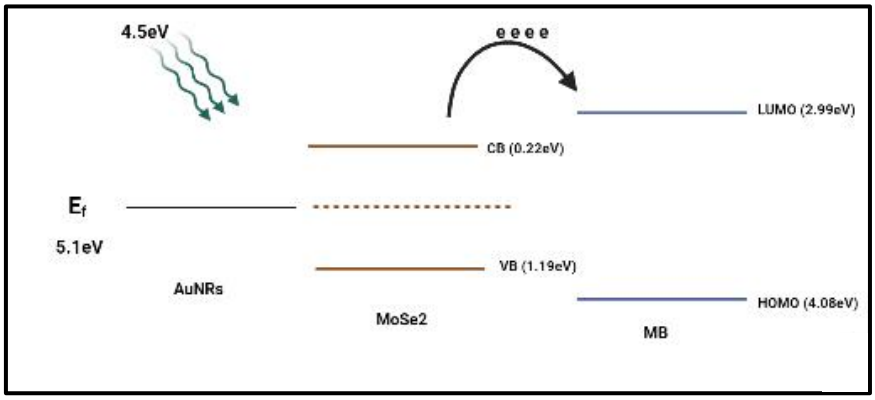


***Scheme.III. 4.****Schematic scheme presenting the proposed mechanism beyond the PIERS enhancement on AuNRs-MoSe2-MB system*

In addition to the fact that MB is used as a dye molecule to check the efficiency of the substrate, it is crucial to determine this analyte due to its drawbacks to human health and in aquaculture Xu et al., 2012. According to the literature, vomiting, shock, and tissue necrosis are some of the health effects resulting from exposure to MB [72,73]. No clear regulation identifying the banning of MB in aquaculture worldwide except in Japan and the USA. Therefore, it is prominent to promote the rapid detector of this organic compound for food quality control. From the findings above, we note that our ERS substrate shows a promising performance toward MB determination.

To sum up, 2D materials have shown promising behaviour to develop electrochemical and plasmonic sensors for the determination of different analytes. This fact is due to their high carrier mobility and the indirect-to-direct crossover…

## References

1. Nguyen, T. P., Sohn, W., Oh, J. H., Jang, H. W. & Kim, S. Y. Size-Dependent Properties of Two-Dimensional MoS $_2$ and WS $_2$. *J. Phys. Chem. C* **120**, 10078–10085 (2016).

2. _Thickness-dependent differential reflectance spectra of monolayer and few-layer.pdf.

3. Mahdavi, M., Kimiagar, S. & Abrinaei, F. Preparation of Few-Layered Wide Bandgap MoS2 with Nanometer Lateral Dimensions by Applying Laser Irradiation. *Crystals* **10**, 164 (2020).

4. Gholamvand, Z., McAteer, D., Harvey, A., Backes, C. & Coleman, J. N. Electrochemical Applications of Two-Dimensional Nanosheets: The Effect of Nanosheet Length and Thickness. *Chem. Mater.* **28**, 2641–2651 (2016).

5. Ottaviano, L. *et al.* Mechanical exfoliation and layer number identification of MoS $_2$ revisited. *2D Mater.* **4**, 045013 (2017).

6. Ghayeb Zamharir, S., Karimzadeh, R. & Aboutalebi, S. H. Laser-assisted tunable optical nonlinearity in liquid-phase exfoliated MoS2 dispersion. *Applied Physics A: Materials Science & Processing* **124**, 692 (2018).

7. Sahoo, D. *et al.* Cost effective liquid phase exfoliation of MoS2 nanosheets and photocatalytic activity for wastewater treatment enforced by visible light. *Sci Rep* **10**, 10759 (2020).

8. Lee, C. *et al.* Anomalous Lattice Vibrations of Single- and Few-Layer MoS $_2$. *ACS Nano* **4**, 2695–2700 (2010).

9. Cao, Z.-Y. & Chen, X.-J. Phonon scattering processes in molybdenum disulfide. *Appl. Phys. Lett.* **114**, 052102 (2019).

10. Zhang, X. *et al.* Phonon and Raman scattering of two-dimensional transition metal dichalcogenides from monolayer, multilayer to bulk material. *Chem. Soc. Rev.* **44**, 2757–2785 (2015).

11. Parlak, O., İncel, A., Uzun, L., Turner, A. P. F. & Tiwari, A. Structuring Au nanoparticles on two-dimensional MoS2 nanosheets for electrochemical glucose biosensors. *Biosens Bioelectron* **89**, 545–550 (2017).

12. Castillo, J. J. *et al.* Synthesis and characterization of covalent diphenylalanine nanotube-folic acid conjugates. *J Nanopart Res* **16**, 2525 (2014).

13. Majidi, F. S. *et al.* Investigating the effect of near infrared photo thermal therapy folic acid conjugated gold nano shell on melanoma cancer cell line A375. *Artif Cells Nanomed Biotechnol* **47**, 2161–2170 (2019).

14. Mers, S. S., Kumar, E. T. D. & Ganesh, V. Gold nanoparticles-immobilized, hierarchically ordered, porous TiO2 nanotubes for biosensing of glutathione. *Int J Nanomedicine* **10 Suppl 1**, 171–182 (2015).

15. Mohd noor, N. *et al.* Photocatalytic Properties and Graphene Oxide Additional Effects in TiO 2. *Solid State Phenomena* **280**, 65–70 (2018).

16. Kaniyoor, A. & Ramaprabhu, S. A Raman spectroscopic investigation of graphite oxide derived graphene. *AIP Advances* **2**, 032183 (2012).

17. Bharath, G. *et al.* Sunlight-Induced photochemical synthesis of Au nanodots on α-Fe2O3@Reduced graphene oxide nanocomposite and their enhanced heterogeneous catalytic properties. *Sci Rep* **8**, 5718 (2018).

18. Qiao, S.-J., Xu, X.-N., Qiu, Y., Xiao, H.-C. & Zhu, Y.-F. Simultaneous Reduction and Functionalization of Graphene Oxide by 4-Hydrazinobenzenesulfonic Acid for Polymer Nanocomposites. *Nanomaterials* **6**, 29 (2016).

19. Chien, C.-T. *et al.* Tunable Photoluminescence from Graphene Oxide. *Angew. Chem. Int. Ed.* **51**, 6662–6666 (2012).

20. Krishnamoorthy, D. & Prakasam, A. Graphene Hybridized with Tungsten disulfide (WS2) Based Heterojunctions Photoanode Materials for High Performance Dye Sensitized Solar Cell Device (DSSCs) Applications. *J Clust Sci* **32**, 621–630 (2021).

21. Zamfir, L.-G., Puiu, M. & Bala, C. Advances in Electrochemical Impedance Spectroscopy Detection of Endocrine Disruptors. *Sensors* **20**, 6443 (2020).

22. Electrochemical sensor for isoniazid detection by using a WS2/CNTs nanocomposite | Elsevier Enhanced Reader. https://reader.elsevier.com/reader/sd/pii/S2666053921000485?token=8243DADA66A89CBE564476EE8AFF0C33735290ACBEE7E70FE8F38DAE4B72897D45B53EF6C76F2547792B

E672F78801AA&originRegion=eu-west-1&originCreation=20220303132842 doi:10.1016/j.snr.2021.100073.

23. Najibi, A., Kamran, S., Baezzat, M. R. & Heidari, R. Evaluating graphene oxide and gold nanocomposites (GO@AuNPs) as adsorbents for preconcentration of tetramethyl thiuram disulfide(thiram) from natural waters and as thiram antidotes for in vivo application. *International Journal of Environmental Analytical Chemistry* **101**, 794–809 (2021).

24. Li, A. *et al.* Bioinspired laccase-mimicking catalyst for on-site monitoring of thiram in paper-based colorimetric platform. *Biosensors and Bioelectronics* **207**, 114199 (2022).

25. Ibáñez, D., Izquierdo-Bote, D., González-García, M. B., Hernández-Santos, D. & Fanjul-Bolado, P. Development of a New Screen-Printed Transducer for the Electrochemical Detection of Thiram. *Chemosensors* **9**, 303 (2021).

26. Maximiano, E. M., Cardoso, C. A. L. & Arruda, G. J. Simultaneous Electroanalytical Determination of Thiram and Carbendazim in Samples of Fresh Fruit Juices in the Presence of Surfactants. *Food Anal. Methods* **13**, 119–130 (2020).

27. Development of gold nanoparticles modified screen-printed carbon electrode for the analysis of thiram, disulfiram and their derivative in food using ultra-high performance liquid chromatography | Elsevier Enhanced Reader. https://reader.elsevier.com/reader/sd/pii/S0039914014007863?token=11EA88BB049C446864647A5A9E4D00596C7F717E58CF0EF6C1DE0CAD6844838865F3DF4F5FEEF7D7E07B7C51F4844E23&originRegion=eu-west-1&originCreation=20220430205238 doi:10.1016/j.talanta.2014.09.020.

28. Alves Sá da Silva, V., Silva Santos, A., Ferreira, T. L., Codognoto, L. & Agostini Valle, E. M. Electrochemical Evaluation of Pollutants in the Environment: Interaction Between the Metal Ions Zn(II) and Cu(II) with the Fungicide Thiram in Billings Dam. *Electroanalysis* **32**, 1582–1589 (2020).

29. Ubeda, M. R., Escribano, M. T. S. & Hernandez, L. H. Determination of Thiram by high-performance liquid chromatography with amperometric detection in river water and fungicide formulations. *Microchemical Journal* **41**, 22–28 (1990).

30. Santos, B. G. *et al.* Electrochemical sensor for isoniazid detection by using a WS2/CNTs nanocomposite. *Sensors and Actuators Reports* **4**, 100073 (2022).

31. Philip, D. Honey mediated green synthesis of gold nanoparticles. *Spectrochimica Acta Part A: Molecular and Biomolecular Spectroscopy* **73**, 650–653 (2009).

32. Lee, H., Ahn, J., Im, S., Kim, J. & Choi, W. High-Responsivity Multilayer MoSe2 Phototransistors with Fast Response Time. *Scientific Reports* **8**, (2018).

33. Optical properties of MoSe2 nanosheets: characterization, simulation and application for Q-switching. https://opg.optica.org/ome/fulltext.cfm?uri=ome-9-8-3494&id=416236.

34. Woodward, R. I. *et al.* Wideband saturable absorption in few-layer molybdenum diselenide ($MoSe_2$) for Q-switching Yb-, Er- and Tm-doped fiber lasers. *Opt. Express, OE* **23**, 20051–20061 (2015).

35. Samikannu, S. & Sivaraj, S. Dissipative soliton generation in an all-normal dispersion ytterbium-doped fiber laser using few-layer molybdenum diselenide as a saturable absorber. *Optical Engineering* **55**, 081311 (2016).

36. Biswas, Y., Dule, M. & Mandal, T. K. Poly(ionic liquid)-Promoted Solvent-Borne Efficient Exfoliation of MoS2/MoSe2 Nanosheets for Dual-Responsive Dispersion and Polymer Nanocomposites. *ACS Publications* https://pubs.acs.org/doi/pdf/10.1021/acs.jpcc.7b00952 (2017) doi:10.1021/acs.jpcc.7b00952.

37. Paton, K. R. & Coleman, J. N. Relating the optical absorption coefficient of nanosheet dispersions to the intrinsic monolayer absorption. *Carbon* **107**, 733–738 (2016).

38. Yang, M. *et al.* Anharmonicity of monolayer $MoS_2$, $MoSe_2$, and $WSe_2$: A Raman study under high pressure and elevated temperature. *Appl. Phys. Lett.* **110**, 093108 (2017).

39. Chen, X. *et al.* Two-dimensional $MoSe_2$ nanosheets via liquid-phase exfoliation for high-performance room temperature $NO_2$ gas sensors. *Nanotechnology* **30**, 445503 (2019).

40. Zhang, S., Zhang, W., Nguyen, T. H., Jian, J. & Yang, W. Synthesis of molybdenum diselenide nanosheets and its ethanol-sensing mechanism. *Materials Chemistry and Physics* **222**, 139–146 (2019).

41. Sun, Z. *et al.* Optical properties of $MoSe_2$ nanosheets: characterization, simulation and application for Q-switching. *Opt. Mater. Express, OME* **9**, 3494–3503 (2019).

42. Tongay, S. *et al.* Thermally Driven Crossover from Indirect toward Direct Bandgap in 2D Semiconductors: $MoSe_2$ versus $MoS_2$. *Nano Lett.* **12**, 5576–5580 (2012).

43. Zhang, X. Characterization of Layer Number of Two-Dimensional Transition Metal Diselenide Semiconducting Devices Using Si-Peak Analysis. *Advances in Materials Science and Engineering* **2019**, 1–7 (2019).

44. Loo, A. H., Bonanni, A., Sofer, Z. & Pumera, M. Exfoliated transition metal dichalcogenides (MoS2, MoSe2, WS2, WSe2): An electrochemical impedance spectroscopic investigation. *Electrochemistry Communications* **50**, 39–42 (2015).

45. Michota, A. & Bukowska, J. Surface-enhanced Raman scattering (SERS) of 4-mercaptobenzoic acid on silver and gold substrates. *Journal of Raman Spectroscopy* **34**, 21–25 (2003).

46. Kho, K. W., Dinish, U. S., Kumar, A. & Olivo, M. Frequency Shifts in SERS for Biosensing. *ACS Nano* **6**, 4892–4902 (2012).

47. Ma, H. *et al.* Frequency Shifts in Surface-Enhanced Raman Spectroscopy-Based Immunoassays: Mechanistic Insights and Application in Protein Carbonylation Detection. *Anal. Chem.* **91**, 9376–9381 (2019).

48. Ma, W., Fang, Y., Hao, G. & Wang, W. Adsorption Behaviors of 4-Mercaptobenzoic Acid on Silver and Gold Films. *Chinese Journal of Chemical Physics* **23**, 659–663 (2010).

49. Zhang, M. *et al.* Three-Dimensional TiO2−Ag Nanopore Arrays for Powerful Photoinduced Enhanced Raman Spectroscopy (PIERS) and Versatile Detection of Toxic Organics. *ChemNanoMat* **5**, 55–60 (2019).

50. Ben-Jaber, S. *et al.* Photo-induced enhanced Raman spectroscopy for universal ultra-trace detection of explosives, pollutants and biomolecules. *Nature Communications* **7**, 1–6 (2016).

51. Almohammed, S., Zhang, F., Rodriguez, B. J. & Rice, J. H. Photo-induced surface-enhanced Raman spectroscopy from a diphenylalanine peptide nanotube-metal nanoparticle template. *Sci Rep* **8**, 3880 (2018).

52. Bhanu, U., Islam, M. R., Tetard, L. & Khondaker, S. I. Photoluminescence quenching in gold - MoS 2 hybrid nanoflakes. *Scientific Reports* **4**, 1–5 (2014).

53. Mao, Z. *et al.* Metal–Semiconductor Contacts Induce the Charge-Transfer Mechanism of Surface-Enhanced Raman Scattering. *J. Phys. Chem. C* **115**, 18378–18383 (2011).

54. Alessandri, I. & Lombardi, J. R. Enhanced Raman Scattering with Dielectrics. *Chem. Rev.* **116**, 14921–14981 (2016).

55. Kuru, C. *et al.* High-performance flexible hydrogen sensor made of $WS_2$ nanosheet–Pd nanoparticle composite film. *Nanotechnology* **27**, 195501 (2016).

56. Abid, K. *et al.* Photoinduced Enhanced Raman Spectroscopy with Hybrid Au@WS2 Nanosheets. *J. Phys. Chem. C* **124**, 20350–20358 (2020).

57. Zhang, X., Guo, L., Li, P., Zhao, B. & Cui, B. SERS as a probe for the charge-transfer process in a coupled semiconductor nanoparticle system $TiO_2$ /MBA/PbS. *RSC Adv.* **7**, 42138–42145 (2017).

58. Tamulewicz, M. *et al.* Layer number dependence of the work function and optical properties of single and few layers $MoS_2$: effect of substrate. *Nanotechnology* **30**, 245708 (2019).

59. Bhanu, U., Islam, M. R., Tetard, L. & Khondaker, S. I. Photoluminescence quenching in gold - MoS2 hybrid nanoflakes. *Sci Rep* **4**, 5575 (2015).

60. Mao, Z. *et al.* Metal–Semiconductor Contacts Induce the Charge-Transfer Mechanism of Surface-Enhanced Raman Scattering. *J. Phys. Chem. C* **115**, 18378–18383 (2011).

61. Ji, P. *et al.* Direct Observation of Enhanced Raman Scattering on Nano-Sized ZrO2 Substrate: Charge-Transfer Contribution. *Front. Chem.* **7**, 245 (2019).

62. Ben-Jaber, S. *et al.* Photo-induced enhanced Raman spectroscopy for universal ultra-trace detection of explosives, pollutants and biomolecules. *Nat Commun* **7**, 12189 (2016).

63. Almohammed, S., Zhang, F., Rodriguez, B. J. & Rice, J. H. Photo-induced surface-enhanced Raman spectroscopy from a diphenylalanine peptide nanotube-metal nanoparticle template. *Sci Rep* **8**, 3880 (2018).

64. Li, C., Huang, Y., Lai, K., Rasco, B. A. & Fan, Y. Analysis of trace methylene blue in fish muscles using ultra-sensitive surface-enhanced Raman spectroscopy. *Food Control* **65**, 99–105 (2016).

65. Ikramova, S. B. *et al.* Surface-Enhanced Raman Scattering from Dye Molecules in Silicon Nanowire Structures Decorated by Gold Nanoparticles. *International Journal of Molecular Sciences* **23**, 2590 (2022).

66. Dutta Roy, S., Ghosh, M. & Chowdhury, J. Adsorptive parameters and influence of hot geometries on the SER(R) S spectra of methylene blue molecules adsorbed on gold nanocolloidal particles: SER(R) S spectra of methylene blue molecules. *J. Raman Spectrosc.* **46**, 451–461 (2015).

67. Prashanth, J. *et al.* Molecular Structure, Vibrational Analysis and First Order Hyperpolarizability of 4-Methyl-3-Nitrobenzoic Acid Using Density Functional Theory. *Optics and Photonics Journal* **5**, 91–107 (2015).

68. Abid, I. *et al.* Plasmon damping and charge transfer pathways in Au@MoSe2 nanostructures. *Materials Today Nano* **15**, 100131 (2021).

69. Panigrahi, P., Hussain, T., Karton, A. & Ahuja, R. Elemental Substitution of Two-Dimensional Transition Metal Dichalcogenides ($MoSe_2$ and $MoTe_2$): Implications for Enhanced Gas Sensing. *ACS Sens.* **4**, 2646–2653 (2019).

70. Tsoutsou, D. *et al.* Epitaxial 2D $MoSe_2$ ($HfSe_2$) Semiconductor/2D $TaSe_2$ Metal van der Waals Heterostructures. *ACS Appl. Mater. Interfaces* **8**, 1836–1841 (2016).

71. Zhang, X. *et al.* Charge-Transfer Effect on Surface-Enhanced Raman Scattering (SERS) in an Ordered Ag NPs/4-Mercaptobenzoic Acid/$TiO_2$ System. *J. Phys. Chem. C* **119**, 22439–22444 (2015).

72. Liu, Y., Hao, X., Hu, H. & Jin, Z. High Efficiency Electron Transfer Realized over $NiS_2/MoSe_2$ S-Scheme Heterojunction in Photocatalytic Hydrogen Evolution. *Acta Physico Chimica Sinica* **0**, 2008030–0 (2020).

73. Muthuraman, G., Teng, T. T., Leh, C. P. & Norli, I. Extraction and recovery of methylene blue from industrial wastewater using benzoic acid as an extractant. *Journal of Hazardous Materials* **163**, 363–369 (2009).

74. Razmara, R. S., Daneshfar, A. & Sahrai, R. Determination of methylene blue and sunset yellow in wastewater and food samples using salting-out assisted liquid–liquid extraction. *Journal of Industrial and Engineering Chemistry* **17**, 533–536 (2011).

# General Conclusion

The main goal of this thesis is the development of electrochemical and plasmonic sensors based on two-dimensional (2D) materials for the determination of various analytes. Indeed, these materials have gained tremendous attention worldwide owing to their fascinating electronic, mechanical, chemical, and thermal features. Therefore, a wide potential of applications is noted based on 2D materials or 2D-materials nanocomposite, recently. The most important is the sensing field since it is crucial in our daily and practical use.

In this work, we aimed the development of low-cost, real-time, sensitive, and selective electrochemical and plasmonic sensors. To accomplish this goal, we have used nanocomposite based on 2D- transition metal dichalcogenides (TMDCs) for the determination of various analytes. Indeed, we have successfully exfoliated $MX_2$ ($MoS_2$, $WS_2$, and $MoSe_2$) nanosheets using a top-down technique named liquid phase exfoliation (LPE) with a number of layers ranging from 3-10. This parameter is determined by both Raman and UV-Vis data. On the other hand, we have synthesized different nanocomposites based on $MX_2$ modified with gold nanoparticles (AuNPs) or graphene oxide (GO).

For the developed electrochemical sensors, we have used a low-cost device known as a screen-printed carbon electrode (SPCE). In order to improve its sensitivity and selectivity, we have used both pure $MX_2$ nanosheets and $MX_2$ nanocomposite (Au-$MoS_2$, Au-$MoSe_2$, and GO-$WS_2$) to modify the working electrode surface of SPCE for the determination of several analytes in different fields; medicine and agriculture.

Regarding the medicine field, a promising sensing mechanism toward the folic acid (FA) on Au-$MoS_2$ is observed. In this prior, a decrease in the oxidation current peak is noted instead of increasing the current peak when increasing the concentration of FA. This fact is due to the strong adsorption of FA on the surface of AuNPs leading to the decrease of active sites number. Still, in the same field, we have used a neurotransmitter named dopamine (DA) which is important for human health. Using this prior, we have studied the electroanalytical performance of different $MX_2$ where we find that $MoSe_2$ shows better behaviour compared to that of $MoS_2$ and $WS_2$. Later, we studied the effect of the number of layers on the electrochemical behaviour for the determination of DA. In this study, we noted that decreasing the layers number results in the improvement of conductivity and electroanalytical performance. Moreover, the sensitivity is significantly enhanced with Au-MoSe2 nanocomposite.

For the agriculture field, $WS_2$ nanosheets were used as pure modifiers toward the determination of thiram fungicide at low concentrations showing good performance. However, better performance is noted on GO-$WS_2$ nanocomposite due to the addition of GO improving the conductivity of the sensing layer.

Using the ERS techniques, we have checked the efficiency of several substrates. Indeed, the Au-$MoS_2$ performance was checked using MBA reporter molecules and then used for the determination of FA at $10^{-4}$M. Moreover, we used Au-WS2 nanocomposite for the determination of MBA using PIERS and SERS. Herein, we have noted that both tools work well with this substrate. However, the PIERS performance is better than that of SERS with a PIERS enhancement factor (EF) 4 times compared to that of SERS. This fact is due to the charge transfer between metal and semiconductor during the pre-irradiation step.

Using the $MoSe_2$ nanosheets, an ERS substrate is created with gold nanorods (AuNRS). This substrate was first tested with a dye molecule known as methylene blue (MB) at $10^{-3}$M. an outstanding enhancement in the Raman signals is observed using the PIERS technique. The mechanism beyond this improvement is fascinating charge transfer between the noble metal and the semiconductor.

From these findings, the $MX_2$ nanosheets can be used either as electrochemical or plasmonic sensors. The nanocomposite made of noble metals and the MX2 nanosheets illustrates promising sensing mechanisms and better performance. These facts can be introduced to the crucial charge transfer between the sensing layers. This work is only the beginning of a promising and crucial work for medicine and environmental applications.